

# **INTERNAL TIDES IN WHITTARD CANYON**

A thesis submitted to the School of Environmental Sciences  
of the University of East Anglia in partial fulfilment  
of the requirements for the degree of Doctor of Philosophy

**TAHMEENA ASLAM**

**JUNE 2017**

© This copy of the thesis has been supplied on condition that anyone who consults it is understood to recognise that its copyright rests with the author and that use of any information derived there from must be in accordance with current UK Copyright Law. In addition, any quotation or extract must include full attribution.



Supervised by:  
Dr. Robert Hall (University of East Anglia),  
Dr. Stephen Dye (Centre for Environment, Fisheries and Aquaculture) and  
Prof. Karen J. Heywood (University of East Anglia)

Wordcount: 41,688 words



# ABSTRACT

Submarine canyons are common bathymetric features incising the shelf edge and are known to trap and focus internal waves leading to high levels of turbulent mixing. Whittard Canyon, located at the Celtic Sea shelf edge, is a dendritic canyon where little is known about the internal tide, yet where it is postulated to have a huge impact on biology within the canyon and also play a role in the generation of nepheloid layers. High-resolution simulations of the  $M_2$  tide in Whittard Canyon using a modified version of the Princeton Ocean Model are used to determine the generation, propagation, spatial structure and dissipation of the internal tide within the canyon. Shamrock canyon and Brenot Spur are identified as key remote sources of internal tide generation, which modulate local generation in a flux-conversion feedback mechanism which causes the observed asymmetry in barotropic-to-baroclinic conversion within the canyon limbs. Depth-integrated baroclinic energy flux within the canyon is elevated, but variably so in different limbs, with values reaching  $>8 \text{ kW m}^{-1}$ . The eastern limb of the canyon is notable for being particularly energetic. Enhancement of near-bottom baroclinic tidal currents are seen within the canyon with velocities reaching  $0.4 \text{ m s}^{-1}$ . The three-dimensional structure exhibits bottom intensification due to topographic focusing by the steep canyon walls, and the dominantly supercritical limb heads. Within the upper canyon the internal tide exhibits a typical mode-1 structure. Cores of baroclinic energy flux, in a dominantly up-canyon direction, form over the depth range of 1000-2500 m and are correlated with potential source regions for nepheloid layers. The sensitivity of the model to bathymetric resolution is tested and it is found that using 500 m resolution bathymetry results in domain-averaged conversion rates higher than for the smoothed bathymetries tested, highlighting the need for high-quality, high-resolution bathymetric datasets.



# ACKNOWLEDGEMENTS

Many thanks to my supervisors Rob Hall, Stephen Dye and Karen Heywood for providing me with the opportunity to carry out this work and for all of their advice and support over the years. Also, thank you to the University of East Anglia and CEFAS who jointly funded my studentship. Thank you to the scientists and crew aboard all the research cruises that I was a part of. From the Celtic Sea to the Samoan Passage, those 14 weeks (!! ) at sea were one of the highlights of my PhD. Special thanks go to Veerle Huvenne, Claudio Lo Iacono and the rest of the CODEMAP team, for providing the opportunity to deploy a Seaglider into Whittard Canyon, and for other help in terms of data that has gone into this work.

The past four and a bit years has been tougher than I ever imagined and so a few thanks are in order to all of the people who helped me get through it. Thanks to the 3.17 crew, past and present - what an amazing office to have been allowed to work in. Special thanks go to Karin for her sense of calm, Céline for her dauntless attitude, Rhiannon for the tea and crosswords and Rich for just being plain wonderful.

Outside of the office, thank you to Viviane and Aurélien for being marvellous friends. How can I forget all of that cheese? Thank you to Nadia, formerly of the SRU, for providing me insights on PhD life in the “arts, darling” and for being there for me whenever I’ve wanted a big old moan. Thank you to Amelia for being a great housemate and friend, thank you to Marina for the Latin spirit, thank you to Ruth for the Janeway levels of awesome, thanks to Osgur for the craic, thank you to Mel for the kindness and the kefir, thank you to Laura D-H for the good times at 66 Adelaide Street, thank you to Bastien and his better half Lauren for their academic world advice and Gareth for the insults and the gentle poke to “just finish already”. Thank you to Kelly for being a great friend despite the time difference. Thank you to Heydon and Fan for being top-notch human beings. Thank you to Polly, for the advice and counsel. Thank you to Amelia mark 2 for the car journeys. Thank you to Caroline and all of Science Team T for the encouragement and kind words. Thank you to my colleagues at Sir John Leman High School, especially my mentor Rozie, for being

understanding of my need to finish my PhD and providing me with the support and motivation needed to do so. And thanks to my students, you're right, "Dr. Aslam" does sound pretty cool. Thank you for the support and love from friends from a life pre-PhD: Sarah J, Sarah C, Cat, Michelle, Raila, Laura and Emma. I hope we can spend more time together now that I've finally finished...

Thank you to mum and dad for the unwavering support they have always provided me, whether that be in the form of a six-hour round trip to bring me some curry, or soothing words over the phone. I could not have wished for more amazing parents, your selflessness constantly inspires me. Thanks to my brother Ashar for the puppy videos and the wisdom beyond your years. I look forward to all of our future Earth science chats at the dining table!

Thank you to Zib and Laika for the cuddles and smiles when it all got a bit too much. You are due large amounts of peanut butter and belly scratches for your services. And finally, thank you to Sam. Thank you for convincing me to persevere with the thesis, for your ability to make me laugh even when I'm feeling down and for simply being my best friend. I couldn't have done this without you.

# CONTENTS

<b>Abstract</b>	<b>v</b>
<b>Acknowledgements</b>	<b>vii</b>
<b>List of figures</b>	<b>xiii</b>
<b>List of tables</b>	<b>xxi</b>
<b>1 Introduction</b>	<b>1</b>
1.1 Internal Waves . . . . .	2
1.1.1 Internal wave reflection . . . . .	3
1.1.2 Internal wave generation and modification within submarine canyons. . . . .	3
1.2 Celtic Sea . . . . .	5
1.2.1 Internal wave generation and modification at the Celtic Sea Shelf.	6
1.3 Whittard Canyon . . . . .	7
1.3.1 Morphology . . . . .	7
1.3.2 Hydrography. . . . .	8
1.3.3 Internal tides. . . . .	8
1.3.4 Interdisciplinary links . . . . .	9
1.4 Motivation and aims . . . . .	9
1.5 Structure of Thesis . . . . .	10
<b>2 Model Setup</b>	<b>11</b>
2.1 Introduction . . . . .	11
2.2 Methods. . . . .	11
2.2.1 The Princeton Ocean Model . . . . .	11
2.2.2 Model setup . . . . .	12
2.2.3 Diagnostics. . . . .	20

2.3	Control run . . . . .	24
2.3.1	Domain size sensitivity . . . . .	24
2.3.2	Run length sensitivity . . . . .	33
2.4	Discussion and Conclusions. . . . .	39
<b>3</b>	<b>Model Validation</b>	<b>41</b>
3.1	Introduction . . . . .	41
3.2	Instrumentation . . . . .	41
3.3	Methodology . . . . .	43
3.3.1	Harmonic tidal analysis . . . . .	44
3.3.2	Error estimates . . . . .	46
3.4	Model and observational data comparison . . . . .	47
3.4.1	ADCP data . . . . .	47
3.4.2	Seaglider data . . . . .	51
3.4.3	Error estimates . . . . .	55
3.5	Discussion and Conclusions. . . . .	56
<b>4</b>	<b>Internal tides in Whittard Canyon</b>	<b>59</b>
4.1	Introduction . . . . .	59
4.2	Internal tide generation . . . . .	61
4.2.1	Remote generation . . . . .	61
4.2.2	Local generation . . . . .	63
4.3	Internal tide propagation through Whittard Canyon . . . . .	64
4.3.1	Baroclinic tidal currents . . . . .	64
4.3.2	Kinetic and potential energy . . . . .	65
4.3.3	3D structure of the $M_2$ internal tide . . . . .	68
4.3.4	Internal tide reflection . . . . .	76
4.4	Canyon energy budget . . . . .	82
4.5	Internal tide propagation on shelf . . . . .	85
4.6	Discussion and Conclusions. . . . .	87
4.6.1	Internal tide generation . . . . .	87
4.6.2	Internal tide propagation through Whittard Canyon. . . . .	90
4.6.3	Canyon energy budget . . . . .	91
4.6.4	Internal tide propagation on shelf . . . . .	91

---

4.6.5	Conclusions . . . . .	92
<b>5</b>	<b>Effects of bathymetric resolution on the modelling of internal tides</b>	<b>95</b>
5.1	Introduction . . . . .	95
5.2	Bathymetric grids . . . . .	96
5.2.1	Criticality . . . . .	98
5.3	Modelling results . . . . .	101
5.3.1	Barotropic-to-baroclinic energy conversion . . . . .	101
5.3.2	Baroclinic energy flux . . . . .	104
5.3.3	Baroclinic energy dissipation . . . . .	107
5.4	Discussion and Conclusions. . . . .	108
<b>6</b>	<b>Internal tide layers for Predictive Habitat Models</b>	<b>111</b>
6.1	Introduction . . . . .	111
6.2	Preliminary results . . . . .	112
6.3	Hydrodynamic variables selection . . . . .	113
6.4	Isopycnal displacement . . . . .	114
6.4.1	Barotropic isopycnal displacement . . . . .	114
6.4.2	Baroclinic isopycnal displacement. . . . .	115
6.4.3	Total isopycnal displacement. . . . .	118
6.5	Discussion and Conclusions. . . . .	122
<b>7</b>	<b>Summary and Synthesis</b>	<b>125</b>
7.1	Summary . . . . .	125
7.1.1	Model setup . . . . .	125
7.1.2	Model validation . . . . .	126
7.1.3	Internal tides in Whittard Canyon . . . . .	126
7.1.4	Bathymetric resolution effects on the internal tide . . . . .	127
7.1.5	Internal tide layers for Predictive Habitat Models. . . . .	127
7.2	Synthesis . . . . .	128
7.2.1	Implications for nepheloid layer generation . . . . .	128
7.2.2	The variability of on shelf energy fluxes. . . . .	131
7.2.3	Importance of domain size and bathymetric resolution for wider internal wave modelling studies . . . . .	132

---

7.3 Future Work . . . . .	133
7.4 Conclusion . . . . .	134
<b>Appendices</b>	<b>135</b>
<b>A Appendix A - Model runs</b>	<b>137</b>
<b>B Appendix B - Along canyon sections of baroclinic energy flux for the minor canyon limbs</b>	<b>139</b>
<b>References</b>	<b>143</b>

# LIST OF FIGURES

1.1	(a) Supercritical reflection between internal waves, entering from above the canyon rim, and the steep canyon walls result in the internal waves being focused towards the canyon floor (b) Subcritical reflection between offshore internal waves and the (typically) gently sloping canyon floors result in the internal waves being focused towards the canyon head. Adapted from Hotchkiss and Wunsch (1982) . . . . .	4
1.2	Map of the Celtic Sea shelf edge . . . . .	6
2.1	Comparison between sigma- and z-co-ordinate systems. Adapted from Carter et al. (2012). . . . .	12
2.2	(a) GEBCO (blue) and INFOMAR (red) bathymetric contours plotted every 500 m (b) Offset between and GEBCO and INFOMAR bathymetry with correction used (degrees) shown in the bottom left hand corner (c) GEBCO and INFOMAR data after correction applied. . . . .	14
2.3	(a) Location of discontinuities found within combined bathymetry, highlighted by red boxes. (b) The same location as in (a) after smoothing carried out along the join boundary. Bathymetric contours are plotted every 100 m . . . . .	15
2.4	Locations of CTD profiles used to create <i>summer</i> (red) and <i>winter</i> (blue) stratification profiles. . . . .	17
2.5	Potential temperature, salinity, buoyancy frequency and potential density profiles for <i>summer</i> (red) and <i>winter</i> (blue) stratification cases. .	18
2.6	Comparison between measured salinity and temperature profiles (black) and profiles averaged over 51 sigma levels (red) for: (a,b) Full depth profiles and (c,d) Profile depths of 2000 m (representative of canyon head depths) . . . . .	19

2.7	(a) Schematic showing a time-series of a generic velocity $U$ and how a harmonic fit to the signal can be represented using amplitude, $U_{amp}$ , phase, $\phi_U$ and $\omega$ , the frequency of the signal ( $\text{rad s}^{-1}$ ) (b) Schematic showing the relationship between a generic velocity $U$ , its real and imaginary components, $U_r$ and $U_i$ and phase and amplitude, $\phi_U$ and $U_{amp}$ . . . . .	21
2.8	The Whittard Canyon system and surrounding region. Contours are plotted every 300 m . . . . .	24
2.9	Domain sizes for model runs $wc01$ , $wc02$ , $wc03$ mapped onto cartesian space (top) and geographic latitude and longitude (bottom). Contours are plotted every 300 m . . . . .	25
2.10	$M_2$ barotropic to baroclinic energy conversion, $E_{conv}$ , for model runs: (a) $wc01$ , (b) $wc02$ and (c) $wc03$ . Depth contours are plotted every 500 m.	27
2.11	Depth-integrated baroclinic $M_2$ energy flux for model runs (a) $wc01$ , (b) $wc02$ and (c) $wc03$ . Vectors are plotted every 40 model grid points ( $\approx 20$ km) in each direction. The underlying colour is the energy flux magnitude. Depth contours are plotted every 300 m. . . . .	31
2.12	Depth-integrated baroclinic $M_2$ energy flux in Whittard Canyon for model runs: (a) $wc01$ , (b) $wc02$ and (c) $wc03$ . Vectors are plotted every 10 model grid points ( $\approx 5$ km) in each direction. The underlying colour is the energy flux magnitude. Depth contours are plotted every 300 m. The difference in energy flux magnitude between $wc01$ and $wc02$ ( $wc01 - wc02$ ) is shown in (d). The difference in energy flux magnitude between $wc02$ and $wc03$ ( $wc02 - wc03$ ) is shown in (e). . . . .	32
2.13	Horizontal current velocity time series from virtual mooring at location 1 ( $48^\circ\text{N } 10.2^\circ\text{W}$ ) . . . . .	34
2.14	Horizontal current velocity time series from virtual mooring at location 2 ( $48.5^\circ\text{N } 9.94^\circ\text{W}$ ) . . . . .	35

2.15	Depth-integrated baroclinic $M_2$ energy flux in Whittard Canyon for model runs: (a) 21, (b) 32 and (c) 43 tidal cycles. Vectors are plotted every 10 model grid points ( $\approx 5$ km) in each direction. The underlying colour is the energy flux magnitude. Depth contours are plotted every 300 m. The difference in energy flux magnitude between 32 and 21 tidal cycles (32 cycles - 21 cycles) is shown in (d). . . . .	38
3.1	Locations of observations used for assessment of model skill. The 1000 m contour is marked in bold and contours are plotted every 200 m . . . .	43
3.2	$M_2$ barotropic surface elevation amplitude and phase (radians) for the current model (left) and TPXO 7.2 model (right). Bathymetric contours are plotted every 200 m using the different models respective bathymetries. . . . .	44
3.3	Schematic showing time-series of observed (solid line) and modelled (dashed line) signals where (a) the observed amplitude is twice the modelled amplitude and (b) where there is a phase shift of $\pi$ between the observed and modelled signal. . . . .	47
3.4	<i>adcp1</i> time-series of along- and across-canyon velocities and depth-averaged along- and across-canyon velocities (blue lines). $M_2$ harmonic fits to both the observations (black), with a spring-neap correction applied, and model output (red) at the <i>adcp1</i> location are also shown. . .	49
3.5	<i>adcp2</i> time-series of along- and across-canyon velocities and depth-averaged along- and across-canyon velocities (blue lines). $M_2$ harmonic fits to both the observations (black), with a spring-neap correction applied, and model output (red) at the <i>adcp2</i> location are also shown. . .	50
3.6	Comparison between $M_2$ isopycnal displacement amplitude (left panel) and phase (centre panel) for glider stations VM1, VM2, VM3a, VM3b, VM4 and VM5 (blue) and the current model (black). The depth structure of relative rms error, $R_E$ , is shown in the right panel. . . . .	53
3.7	Comparison between $M_2$ isopycnal displacement amplitude (left panel) and phase (centre panel) for glider stations VM6, VM7, VM8a and VM8b (blue) and the current model (black). The depth structure of relative rms error, $R_E$ , is shown in the right panel. . . . .	54

3.8	(a) Amplitude and (b) phase of modelled near-bottom total (barotropic and baroclinic) zonal $M_2$ velocity in the region surrounding <i>adcp1</i> and <i>adcp2</i> . (c) Amplitude and (d) Phase of modelled near-bottom total meridional $M_2$ velocity in the region surrounding <i>adcp1</i> and <i>adcp2</i> . (e) Maps of criticality ( $\alpha$ ) for the region surrounding <i>adcp1</i> and <i>adcp2</i> . Contours are plotted every 300 m. . . . .	57
4.1	Location of limbs and along-thalweg sections used. Distance along each thalweg, referenced to the 1000-m isobath (positive shallower than 1000 m, negative deeper than 1000 m) is marked in either 20-km or 10-km intervals. . . . .	60
4.2	(a) Depth-integrated baroclinic $M_2$ energy flux in the Whittard Canyon region. Vectors are plotted every 40 model grid points ( $\approx 20$ km) in each direction. The underlying colour is the energy flux magnitude. (b) Barotropic-to-baroclinic $M_2$ energy conversion. Positive values indicate sources of baroclinic energy. Depth contours are plotted every 200 m. . .	62
4.3	Modelled near-bottom horizontal baroclinic $M_2$ tidal current ellipses. Current ellipses shallower than 300 m are omitted for clarity. Depth contours are plotted every 200 m. . . . .	65
4.4	(a) Depth-integrated baroclinic $M_2$ HKE in Whittard Canyon. (b) Depth-integrated $M_2$ APE. Depth contours are plotted every 200 m. . . . .	66
4.5	Limb 1a along-canyon sections (a) Depth-integrated along-canyon baroclinic $M_2$ energy flux (blue), HKE (green) and APE (red) with distance along the thalweg. (b) Along-canyon and (c) across-canyon baroclinic $M_2$ energy flux with distance along the thalweg. Positive along-canyon values are towards the head of the canyon. Positive across-canyon values are to the left when looking up canyon. (d) Along-canyon HKE. (e) Along-canyon APE. Distance along the canyon is referenced to the 1000-m isobath; positive distances are towards the head of the canyon and negative distances are towards the mouth of the canyon. . . . .	70
4.6	Limb 2a along-canyon sections. See Figure 4.5 for explanation. Note that the vertical scales are different. . . . .	71

4.7	Limb 3a along-canyon sections. See Figure 4.5 for explanation. Note that the vertical scales are different. . . . .	72
4.8	Limb 4a along-canyon sections. See Figure 4.5 for explanation. . . . .	73
4.9	Along-canyon baroclinic $M_2$ energy at across-sections located at (a) -60 km, (b) -40 km, (c) -20 km, and (d) 0 km along the thalweg of Limb 4a (referenced to the 1000-m isobath). flux with distance along the thalweg. Positive along-canyon values are towards the head of the canyon. . . . .	75
4.10	Map of the ratio of the topographic slope to the $M_2$ characteristic slope, $\alpha$ (criticality). Depth contours are plotted every 500 m. . . . .	77
4.11	Limb 1a: (a) Along-canyon baroclinic $M_2$ energy flux, with distance along the thalweg for Limb 1a. Positive along-canyon values are towards the head of the canyon. (b) $\alpha$ with distance along the thalweg (blue) and $\alpha$ smoothed with a running mean using a $\sim 5$ km filter (black). The grey shaded region denotes the ‘near-critical region’ ( $0.8 < \alpha < 1.3$ ). . . . .	79
4.12	Limb 2a (see Figure 4.11 for explanation) . . . . .	80
4.13	Limb 3a (see Figure 4.11 for explanation) . . . . .	80
4.14	Limb 4a (see Figure 4.11 for explanation). An $M_2$ internal tide characteristic slope for an internal tide propogating up canyon is calculated using the internal wave dispersion relation and is plotted over the section. . . . .	81
4.15	Depth-integrated baroclinic $M_2$ energy flux in the Whittard Canyon region. Vectors are plotted every 40 model grid points ( $\approx 20$ km) in each direction. The underlying colour is the energy flux magnitude. Depth contours are plotted every 200 m. The regions used to calculate the canyon energy budget are outlined in black and correspond to the canyon limb naming convention used in this thesis. A corrugated region (corr.) is also used. The Brenot Spur section is also included and the arrow indicates the direction of the flux calculated (44 MW). . . . .	82

4.16 (a) Depth-integrated baroclinic $M_2$ energy flux on the continental shelf. Vectors are plotted every 5 model grid points ( $\approx 2.5$ km) in each direction. The underlying colour is the energy flux magnitude. Depth contours are plotted every 200 m and the black line is the 300-m isobath, the approximate depth of the shelf break. Distance along the 300-m isobath is marked with a cross at 50 km intervals (b) Depth-integrated across-slope baroclinic $M_2$ energy flux with distance along the 300-m isobath. Positive values indicate a flux onto the shelf. . . . .	85
4.17 Flux-conversion feedback showing how a fixed remote source ( $p'_{remote}$ ), but variable local generation ( $p'_{local}$ and $w_{BT}$ ) leads to conditions where positive (left), zero (centre) and negative (right) $E_{conv}$ occur . . . . .	89
5.1 The model bathymetries used in the (a) 500 m and (b) 15 km runs. . . . .	97
5.2 Topographic height and slope spectra for the 500 m, 1500 m, 5500 m and 15 km bathymetries. The equivalent internal mode wavenumbers are shown for reference. . . . .	98
5.3 Maps of $\alpha$ for the (a) 0.5 km gridded bathymetry (b) bathymetry smoothed with a 5.5 km mean filter. Depth contours are plotted every 500 m. . . . .	100
5.4 $M_2$ barotropic-to-baroclinic energy conversion, $E_{conv}$ , for the (a) 500-m, (b) 1.5-km, (c) 5.5-km and (d) 15-km model runs. Depth contours are plotted every 500 m. . . . .	103
5.5 Depth-integrated baroclinic $M_2$ energy flux for the (a) 500-m, (b) 1.5-km, (c) 5.5-km and (d) 15-km model runs. Vectors are plotted every 40 model grid points ( $\approx 20$ km) in each direction. The underlying colour is the energy flux magnitude. Depth contours are plotted every 300 m. . . . .	105
6.1 (a) Improvement in PHM performance through the inclusion of modelled near-bottom velocity as shown in (b). (b) Snapshot of modelled near-bottom velocity (barotropic plus baroclinic) used as a layer in the PHM. Vectors are plotted every 15 model grid points (7.5 km) and vectors shallower than 300 m are omitted for clarity. Depth contours are plotted every 300 m. . . . .	113

6.2	Barotropic isopycnal displacement amplitude (left) and phase (right). Contours are plotted every 300m . . . . .	115
6.3	Baroclinic isopycnal displacement amplitude using (a) 1 km square average and (b) 2.5 km square average. Contours are plotted every 300 m.	117
6.4	Baroclinic isopycnal displacement phase using (a) 1 km square average and (b) 2.5 km square average. Contours are plotted every 300 m. . . . .	117
6.5	Isopycnal displacement amplitude in <i>Limb4</i> associated with: (a) the $M_2$ surface tide ( $\zeta_{BT}$ ), (b) the $M_2$ internal tide ( $\zeta_{BC}$ ) and (c) the two combined. Note that the total isopycnal displacement is a summation of the real and imaginary components of $\zeta_{BT}$ and $\zeta_{BC}$ . . . . .	119
6.6	(a) Near-bottom temperature variability due to total (barotropic + baroclinic) modelled isopycnal displacement. The 1000 m isobath is indicated by the bold line. (b) Near-bottom oxygen variability due to total modelled isopycnal displacement. (c) Oxygen (black) and temperature (red) profiles used to calculate (a) and (b). . . . .	121
7.1	Depth ranges of baroclinic energy flux cores in the model (black) in comparison with the depth range from where nepheloid layers are sourced (dashed red) (Wilson et al., 2015b). . . . .	129
7.2	Locations where RMS current speed for the baroclinic $M_2$ tidal current exceeds $0.15 \text{ m s}^{-1}$ (red). Depth contours are plotted every 200 m. . . . .	130
B.1	Limb 1b along-canyon sections (b) Along-canyon and (c) across-canyon baroclinic $M_2$ energy flux with distance along the thalweg. Positive along-canyon values are towards the head of the canyon. Positive across-canyon values are to the left when looking up canyon. . . . .	140
B.2	Limb 1c along-canyon sections (See Figure B.1 for explanation) . . . . .	140
B.3	Limb 2b along-canyon sections (See Figure B.1 for explanation) . . . . .	140
B.4	Limb 2c along-canyon sections (See Figure B.1 for explanation) . . . . .	141
B.5	Limb 3b along-canyon sections (See Figure B.1 for explanation) . . . . .	141
B.6	Limb 4b along-canyon sections (See Figure B.1 for explanation) . . . . .	141



# LIST OF TABLES

2.1	Details of CTD profiles used to create <i>summer</i> and <i>winter</i> stratification profiles . . . . .	17
2.2	Model runs for diagnosing domain size including run time on GRACE (High powered computing cluster) . . . . .	26
2.3	Area-integrated and area-averaged barotropic to baroclinic energy conversion in the <i>wc01</i> , <i>wc02</i> and <i>wc03</i> model runs for each entire domain, and within each domain, the Whittard Canyon region and the Shamrock Canyon region (only <i>wc03</i> contains this complete region). . .	28
2.4	Area-integrated and area-averaged baroclinic energy flux divergence in the <i>wc01</i> , <i>wc02</i> and <i>wc03</i> model runs for the Whittard Canyon region (bold) and the whole domain. . . . .	29
2.5	Domain-integrated and domain-averaged barotropic to baroclinic energy conversion in the 21, 32 and 43 tidal cycle model runs for each entire domain, and within each domain, the Whittard Canyon region and the Shamrock Canyon region. . . . .	36
2.6	Domain-integrated and domain-averaged baroclinic energy flux divergence in the 21, 32 and 43 tidal cycle runs model runs for the Whittard Canyon region (bold) and the whole domain.	37
3.1	Location, dates, depth and instrument used at each ADCP station . . . .	42
3.2	Location of glider stations . . . . .	42
3.3	Details of the tidal constituents fit by harmonic analysis to the observational data. . . . .	45
3.4	Comparison of $M_2$ velocity amplitudes and phases between the model and ADCPs. . . . .	51
3.5	Average RMS error ( $\bar{E}$ ) and average relative RMS error ( $\overline{R_E}$ ) between the model and Seaglider data. . . . .	55

4.1	HKE and APE ( <i>italics indicates recalculation of APE after the barotropic contribution to isopycnal displacement has been removed</i> ) integrated over the regions shown in Figure 4.15 and the resulting HKE/APE ratio ( <i>italics indicate where recalculated APE has been used</i> ). . . . .	67
4.2	Fraction of depth between 500 m and 3000 m depth that are subcritical, supercritical and near-critical for the main limbs within Whittard Canyon.	81
4.3	Model baroclinic energy estimates integrated over the regions shown in Figure 4.15, including: baroclinic energy flux divergence, barotropic to baroclinic energy conversion and baroclinic energy dissipation. . . . .	83
5.1	Percentage of domain that is sub-critical, near-critical (defined as $0.9 < \alpha < 1.1$ ) and supercritical for the <i>0.5 km</i> , <i>1.5 km</i> and <i>5.5 km</i> model. . . . .	101
5.2	Area-integrated and area-averaged barotropic-to-baroclinic energy conversion for the 500-m, 1.5-km, 5.5-km and 15-km model runs for each entire domain, and within each domain, the Whittard Canyon region and the Shamrock Canyon region. . . . .	104
5.3	Area-integrated and area-averaged baroclinic energy flux in the 500-m, 1.5-km, 5.5-km and 15-km model runs for each entire domain, and within each domain, the Whittard Canyon region and the Shamrock Canyon region (only <i>wc03</i> contains this complete region). . . . .	106
5.4	Inferred dissipation in the 500-m, 1.5-km, 5.5-km and 15-km model runs for each entire domain, and within each domain, the Whittard Canyon region and the Shamrock Canyon region (only <i>wc03</i> contains this complete region). . . . .	107
A.1	List of model runs used in this thesis. The control run is marked in red. . . . .	138

# 1

## INTRODUCTION

Shelf seas are considered highly productive regions, as even though they cover less than 10% of the oceans surface area, they contribute 15 to 30% to the total oceanic primary production (Hickman et al., 2012). Understanding the biological and physical processes that control shelf sea primary productivity is therefore of great interest from both an academic, and economic point of view. The Celtic Sea shelf edge is a region notable for its highly productive fisheries and it is hypothesised that higher mixing rates, driven by internal waves, drive vertical nitrate fluxes which fuel new phytoplankton production (Sharples et al., 2009). The geometry at the Celtic Sea shelf break is complex, due to its incision by multiple submarine canyons, thus providing multiple internal wave generation locations and propagation pathways. The generation and reflection of internal waves is dependant on topographic slope. Therefore the presence of submarine canyons, are likely to create a complex internal wave field through both generation and reflection. However, observational data within canyons needed in order to investigate these dynamics are difficult and expensive to obtain. Numerical models are therefore vital tools to utilise in order to begin to understand the internal wave fields within submarine canyons.

One of the major canyons that incise the Celtic Sea shelf break is Whittard Canyon. This canyon, with its complex dendritic morphology, is home to a diverse range of habitats (Huvenne et al., 2011; Johnson et al., 2013), but the conditions that enable these habitats to flourish is not fully understood. Internal waves are associated with

enhanced near-bottom energy, and this has been identified as a major mechanism in the production and the maintenance of nepheloid layers, particularly in sloping environments and canyons (e.g. McPhee-Shaw and Kunze, 2002; McPhee-Shaw et al., 2004; Puig et al., 2004). This may provide nutrient pathways for habitats, therefore, any insights into the spatial variability of internal waves within Whittard Canyon obtained from numerical models, are also of interest for researchers in a wide range of fields, from sedimentology to ecology.

Submarine canyons are common incisions along the shelf edge globally (Harris and Whiteway, 2011), however, internal waves have previously only been well studied using numerical models within submarine canyons that are simple incisions (e.g. Gregg et al., 2011, Ascension Canyon) or meandering (e.g. Hall and Carter, 2011; Lee et al., 2009, Monterey and Gaoping Canyon, respectively). This work provides the first numerical modelling study of internal wave dynamics within a dendritic canyon. The results of this study therefore have implications for global estimates of mixing at the shelf edge (e.g. Carter and Gregg, 2002), which previously have only accounted for shelf edges incised by canyons with much simpler morphologies.

## 1.1 INTERNAL WAVES

Internal waves propagate beneath the ocean surface and are generated when the stratification of the ocean is disturbed. Internal waves with tidal frequencies are termed internal tides. They form when horizontal tidal currents encounter submarine obstacles such as ridges, causing the water to be forced up over the obstacle (Carter et al., 2012). If the water is stratified, then the surfaces of constant density (isopycnals) near the obstacle oscillate with tidal frequency, resulting in isopycnal disturbances that propagate outwards from that region as internal gravity waves. The deviation of the isopycnal disturbances from almost horizontal, isobaric surfaces mean that the velocity and pressure field perturbations caused by internal waves are baroclinic (Carter et al., 2012). Hence, the internal tides propagating away from the disturbance can be referred to as baroclinic tides whilst surface tides are termed barotropic.

If stratification varies continuously, internal waves propagate vertically as well as horizontally. The angle of the wavenumber vector ( $\mathbf{k}$ ) and by definition the

phase velocity vector ( $\mathbf{c}$ ) with the vertical,  $\theta$ , and also the ratio of horizontal to vertical wavenumber,  $\tan\theta = k_h/k_z$ , is given by the internal wave dispersion relation,

$$\omega^2 = f^2 \cos^2 \theta + N^2 \sin^2 \theta \quad (1.1)$$

where  $\omega$  is the angular frequency of the wave,  $f = 2\Omega \sin\phi$  is the inertial (or Coriolis) frequency, where  $\Omega$  is the angular rotational frequency of the Earth and  $\phi$  is latitude and  $N = [-(g/\rho_0)(d\rho/dz)]^{1/2}$  is the buoyancy frequency, where  $\rho_0$  is a reference density, and  $d\rho/dz$  is the vertical potential density gradient. The dispersion relation implies that internal waves can only exist between a range of frequencies, namely the inertial frequency and the buoyancy frequency, i.e.  $f < \omega < N$ .

### 1.1.1 INTERNAL WAVE REFLECTION

The reflection of internal waves differs from internal wave generation in that the behaviour is entirely dependant on the topographic slope (Hall and Carter, 2011). The onshore-offshore propagation direction of deep water internal waves that have encountered a topographic slope can be calculated using the ratio of the topographic slope to the internal wave characteristic slope,

$$\alpha = \frac{s_{topog}}{s_{wave}} = \frac{\partial H / \partial x}{[(\omega^2 - f^2) / (N^2 - \omega^2)]^{1/2}} \quad (1.2)$$

where  $H$  is the total depth,  $x$  across-slope distance,  $\omega$  the angular frequency of the wave,  $f$  the inertial frequency and  $N$  the buoyancy frequency. If  $\alpha < 1$  (subcritical), after reflection, waves will continue to shoal. If  $\alpha > 1$  (supercritical), waves will travel back into deeper water after reflection. If  $\alpha = 1$  (critical), nonlinear effects and potential wave breaking can occur.

### 1.1.2 INTERNAL WAVE GENERATION AND MODIFICATION WITHIN SUBMARINE CANYONS

The continental shelves and slopes of continental margins are often incised by submarine canyons (Harris and Whiteway, 2011). They are common features and are often similar in scale to canyons seen on land such as the Grand Canyon ( ~ 10-30

km wide and  $\sim 2$  km deep) (Hickey, 1995). There can be marked differences between the slopes of the canyon walls, floor and the adjacent continental slope, therefore there are multiple sites where the generation and reflection of internal tides can occur (Hickey, 1995).

Scattering of the barotropic tides from the sloping topography can generate internal tides (Baines, 1982) whilst reflection can lead to trapping and focusing of internal waves from outside the canyon towards the head of the canyon (Gordon and Marshall, 1976; Hotchkiss and Wunsch, 1982). Super- critical reflection of internal waves from the steep canyon walls results in the internal waves above the canyon rim being focused towards the canyon floor (Gordon and Marshall, 1976). In addition, submarine canyon floors are typically gently sloping and subcritical reflection along this surface results in offshore internal waves being focused towards the canyon head (Hotchkiss and Wunsch, 1982) (Figure 1.1).

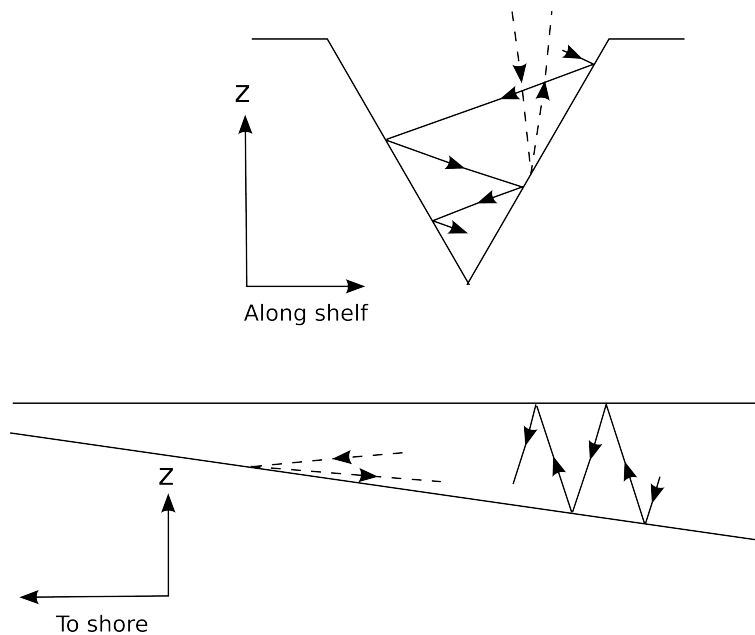


**Figure 1.1:** (a) Supercritical reflection between internal waves, entering from above the canyon rim, and the steep canyon walls result in the internal waves being focused towards the canyon floor (b) Subcritical reflection between offshore internal waves and the (typically) gently sloping canyon floors result in the internal waves being focused towards the canyon head. Adapted from Hotchkiss and Wunsch (1982)

During reflection the separation between adjacent internal wave characteristics narrows, resulting in a concentration of the energy into a smaller region (Hall and Carter, 2011). Therefore, during both the subcritical and supercritical

examples mentioned above, energy density increases. Internal wave energy density enhancement has been observed in a number of canyons, for example, Hudson Canyon (Hotchkiss and Wunsch, 1982) and Gaoping Canyon off Taiwan (Lee et al., 2009). This enhanced tidal and internal wave energy within canyons results in extremely large amounts of mixing. For example, diffusivity within Monterey Canyon has been measured at  $0.05 \text{ m}^2\text{s}^{-1}$  near the canyon axis and only a factor of 10 times smaller towards the rim depth (Carter and Gregg, 2002). In the case of near-critical reflection ( $\approx 1$ ), the energy is trapped against the boundary resulting in non-linear effects such as wave breaking, internal bores and turbulent mixing (e.g., Nash et al., 2004).

The short horizontal scale of submarine canyons result in them being avoided by coastal observation programmes as they are difficult to characterize with a small number of point measurements (Kunze et al., 2002). Obtaining measurements from within the canyons is also made difficult by the steep canyon walls which make obtaining CTD profiles safely difficult, and also comprise the accuracy of deploying moored arrays (Hickey, 1995). Hence, models that can be validated with relatively few measurements are vitally important to fully understand the behaviour of internal waves within submarine canyons.

## 1.2 CELTIC SEA

The Celtic Sea, located off the south coast of Ireland, is approximately 400km wide and is a 100 - 200 m deep shelf sea that is notable for the presence of a combination of large tidal currents and strong seasonal fluctuations in surface cooling and heating (Green et al., 2008). The supply of freshwater to the Celtic Sea is small, therefore temperature dominates stratification and during the summer a strong seasonal stratification is established over areas where stirring by tides and wind is small compared to buoyancy input (Green et al., 2008).

The shelf break (Figure 1.2) has a west-northwest to east-southeast trend from the eastern margin of the Goban Spur to the Brenot Spur (Bourillet and Mulder, 2006). The slope break occurs between depths of 170 m and 300 m, with the landward shelf morphology displaying relative smoothness compared to the corrugated margin (Cunningham et al., 2005). The margin is deeply incised by a number of submarine

canyons that are typically orientated NNW SSE and NNE SSW (Cunningham et al., 2005). The main canyons are Shamrock Canyon, Whittard Canyon, Black Mud Canyon and King Arthur Canyon, and feed sand into the Celtic Deep Sea Fan.

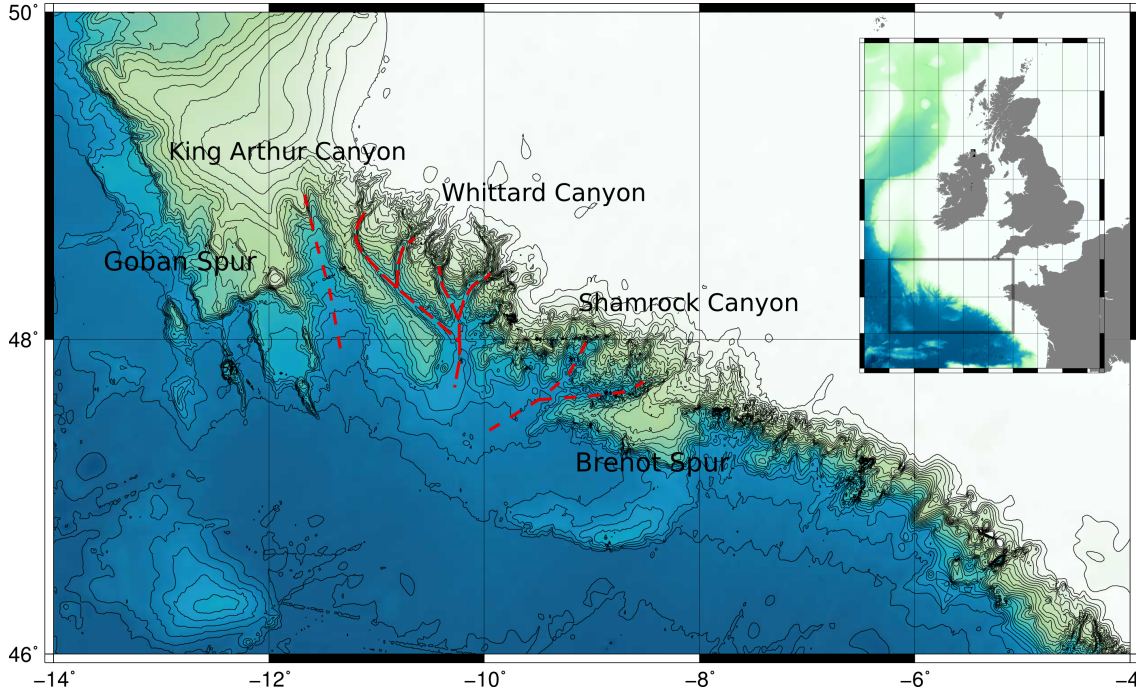


**Figure 1.2:** Map of the Celtic Sea shelf edge

### 1.2.1 INTERNAL WAVE GENERATION AND MODIFICATION AT THE CELTIC SEA SHELF

Barotropic tidal flow over the shelf edge forces the stratified water to move up and down the slope, generating internal waves and a baroclinic energy flux. Close to the shelf edge, the majority of the internal tide is dissipated, causing vertical mixing which drives a nutrient flux which maintains a subsurface chlorophyll maximum observed at the Celtic Sea shelf edge (Green et al., 2008). The remaining internal tide energy propagates onto the shelf, thus providing the stratified regions of the inner Celtic Sea shelf with a small but significant source of energy (Simpson, 1998b). The primary energy source for mixing in the pycnocline of large areas of stratified shelf such as the Celtic Sea is not well understood, however, it has been suggested that internal waves that are generated at the shelf edge may be one of the main contributors to this mixing (Green et al., 2008). Another source of energy for

mixing at the shelf edge arises from remotely generated internal tides which, upon encountering the shelf edge, are reflected and depending on whether supercritical, subcritical or critical reflection takes place, leads to higher mixing rates (Sharples et al., 2009). Within the Celtic Sea, this increased vertical mixing drives vertical nitrate fluxes which fuel new phytoplankton production (Sharples et al., 2009). This internal tide driven productivity may help explain the high fish and fish larva densities observed at Celtic Sea shelf edge (Sharples et al., 2009).

## **1.3 WHITTARD CANYON**

A recent review of Whittard Canyon (Amaro et al., 2016) provides an overview of research carried out in the canyon, including preliminary results from this work. However, key points about the canyon pertinent to this work are summarised here.

### **1.3.1 MORPHOLOGY**

The cross-sectional profiles of canyons along the Celtic Shelf are typically V-shaped towards the head of the canyon and increasingly U-shaped down-slope (Cunningham et al., 2005). This may be due to a down-slope change from erosive to depositional processes or due to the canyons acting as conduits by which sediment can bypass the continental shelf on to the abyssal plain (Cunningham et al., 2005). Irrespective of the cause of the change in morphology, the difference has implications for the modification and generation of internal waves due to the variability in canyon wall slope along the length of the canyon. The canyons that have historically been well studied with regards to internal waves (e.g. Monterey Canyon) comprise of a single canyon, however, globally many submarine canyons are dendritic, with many smaller canyons branching off the primary canyon. Harris and Whiteway (2011) classify canyon dendricity as the number of canyon limbs per unit area, excluding the primary canyon thalweg (a line denoting the lowest points along the length of a canyon). With this scheme they determined that the mean concentration of dendritic canyon limbs was 3.3 limbs per 100,000 km<sup>2</sup> for canyons occurring on passive margins like the Celtic Sea Shelf. Whittard Canyon itself comprises of four main branches, with numerous minor branches. No studies of the effect of dendritic canyons on the internal wave

field appear to have been made.

### **1.3.2 HYDROGRAPHY**

Along the Celtic Margin, the upper-water column (0 - 1500 m) is characterised by central and intermediate water masses originating from sub-tropical latitudes. Eastern North Atlantic Water (ENAW), a winter mode water occupying the layer above the permanent thermocline, is a relatively warm and saline water sourced in the SW Bay of Biscay region (e.g Pérez et al., 1995; Pollard et al., 1996). Below the ENAW lies Mediterranean Outflow Water (MOW) (e.g van Aken, 2000). In deeper waters (1600-2200 m) Labrador Sea Water layers are present (Bower et al., 2002). The European Slope Current (ESC) carrying the ENAW and boundary flows associated with the MOW (Van Rooij et al., 2010) dominate flow characteristics in this region (Pingree and Le Cann (1990). Near the seabed, observed currents generally have a tidally induced downslope mean component (Pingree and Le Cann, 1989).

### **1.3.3 INTERNAL TIDES**

As previously discussed, internal waves and tides are generated at the shelf break by across-slope tidal flow along the Celtic Sea shelf edge (Pingree et al., 1986; Holt and Thorpe, 1997). The direction of the propagating internal waves onto the shelf, however, is quite random (Holt and Thorpe, 1997), which is in contradiction to the generally accepted view that across-shelf internal wave energy flux is controlled by the orientation of the shelf break (Garrett and Kunze, 2007). Near Whittard Canyon, internal solitary waves with amplitudes reaching a maximum of 105 m have been reported (Vlasenko et al., 2014). The internal tide generated at the shelf break has been observed as a coherent signal up to 170 km onto the Celtic Sea shelf (Inall et al., 2011). However, much of the energy generated at the shelf edge is dissipated near the shelf break as indicated by a shoreward energy decay scale of 42 km (Inall et al., 2011). Understanding the effect of the Whittard Canyon on the internal wave field is therefore important in understanding the internal wave dynamics within the region.

### 1.3.4 INTERDISCIPLINARY LINKS

The internal tide within Whittard Canyon has been postulated to have a potentially huge impact on the biology within the canyon (Robert et al., 2015) and also play a role in the generation of nepheloid layers, which are layers of suspended sediment and organic material along density surfaces (Wilson et al., 2015b). Vertical walls dominated by cold water corals, clams and deep sea oysters, as identified in Whittard Canyon (Huvenne et al., 2011; Johnson et al., 2013), are a novel habitat and the environment that promotes their presence is not yet known. It has been suggested that nutrient supply and internal tide dynamics may have a role to play (Wilson et al., 2015b; Johnson et al., 2013; Huvenne et al., 2011). The depth distribution of corals has been related to regions where internal waves cause enhanced productivity through vertical mixing and nutrient fluxes, and by elevating near seabed shear stresses and hence generating enhanced organic fluxes in the benthic boundary layer (Frederiksen et al., 1992). This enhanced near-bottom energy associated with internal waves has also been identified as a major mechanism in the production and the maintenance of nepheloid layers, particularly in sloping environments and canyons (e.g. McPhee-Shaw and Kunze, 2002; McPhee-Shaw et al., 2004; Puig et al., 2004). The insights into the spatial variability of the internal tide within Whittard Canyon, are therefore also of interest for researchers in a wide range of fields, from sedimentology to ecology.

## 1.4 MOTIVATION AND AIMS

The potential influence of internal tides on the dynamics, sedimentation patterns and biology within submarine canyons cannot be overstated, however, observational data across large canyon systems is difficult and expensive to obtain. The research presented here uses numerical simulations in order to provide a first comprehensive study of the  $M_2$  internal tide within Whittard Canyon. The specific aims of this thesis are to:

- Identify the key generation sites for the internal tide in Whittard Canyon
- Describe the spatial variability of the internal tide within Whittard Canyon and suggest possible mechanisms to explain this variability

- Estimate an energy budget for Whittard Canyon
- Assess the effect of varying bathymetric resolution on modelling of the internal tide within Whittard Canyon
- Create resources for marine biologists in order to help them assess the effect of internal tide hydrodynamics on benthic habitats

## **1.5 STRUCTURE OF THESIS**

This thesis contains five main chapters. In Chapter 2 the model setup is explained and the sensitivity of the model to both run length and domain size tested to identify the ideal control run setup to model the internal tide in Whittard Canyon. In Chapter 3 the model is validated against observational data in the canyon. In Chapter 4 the generation and propagation of the internal tide in Whittard Canyon are discussed and a crude energy budget for the canyon calculated. In Chapter 5, the model is run with different bathymetric resolutions to see how this affects barotropic-to-baroclinic conversion and the resulting internal tide field within the model. In Chapter 6 the preliminary attempt at integrating internal tide hydrodynamics within predictive habitat models is described. Key results from the work are presented in Chapter 7 along with recommendations for future work.

# 2

## MODEL SETUP

### 2.1 INTRODUCTION

This chapter details how the control run of the Whittard Canyon region is defined. The objective is to insure that the model parameters are set so that the  $M_2$  internal wave field is accurately represented by the simulations. The general model setup and diagnostic tools to be used are outlined in section 2. In section 3 model sensitivities to domain size and run length are tested.

### 2.2 METHODS

#### 2.2.1 THE PRINCETON OCEAN MODEL

We use the Princeton Ocean Model (POM), which is a hydrostatic, three-dimensional, primitive equation numerical model employing a sigma-coordinate system in the vertical direction (Blumberg and Mellor, 1987). The use of a sigma vertical-coordinate system results in terrain-following vertical levels where the grid lines follow bathymetry and the free surface, and are spaced uniformly through the water column (Figure 2.1). This provides good resolution of the surface and bottom boundary layers, the latter of which is important, as the bottom-following current is an important part of internal tide generation (Carter et al., 2012).

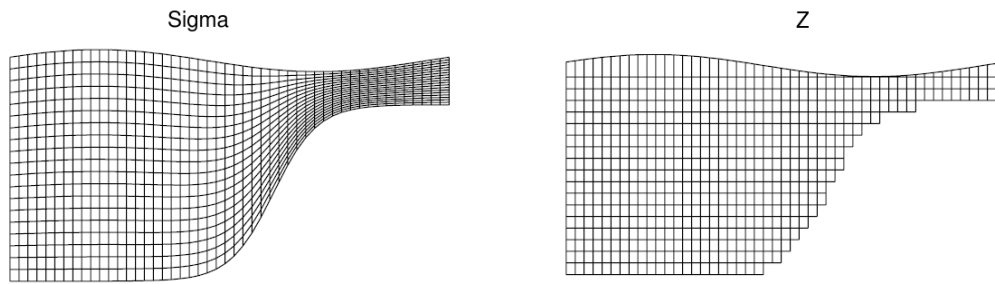


**Figure 2.1:** Comparison between sigma- and z-co-ordinate systems. Adapted from Carter et al. (2012).

### 2.2.2 MODEL SETUP

The simulations are run for an integer number of  $M_2$  tidal cycles using 51 sigma levels from a quiescent state with vertically varying but horizontally uniform temperature and salinity. The open boundary forcing is ramped up from zero to full strength over 2 tidal cycles. Harmonic analysis over the last 11 tidal cycles of model output are used to obtain  $M_2$  current amplitudes and phases ( $u$ ,  $v$ ,  $w$ ).

#### BATHYMETRIC GRID

A 500 m bathymetric grid derived from the Integrated Mapping for the Sustainable Development of Ireland's Marine Resources (INFOMAR)  $\sim$  500 m resolution bathymetry and the General Bathymetric Chart of the Oceans (GEBCO) 30 arc-second global grid (Becker et al., 2009) is used in all simulations. The high resolution bathymetry only covered the areas of Whittard Canyon within Irish waters, so GEBCO data were used to fill any gaps. Both datasets were gridded in terms of a fixed number of arcseconds (INFOMAR - 18 arcseconds, GEBCO - 30 arcseconds), resulting in variable horizontal distances between grid points due to the curvature of the Earth's surface. Fixed horizontal resolutions are favourable for later bathymetry manipulation, hence both sources were resampled to a fixed horizontal resolution of 500 m, using the southwestern corner as a reference point, and then combined.

The join between the two data was inspected and in regions of slowly varying topography, such as that found at the abyssal plain and the shelf, the join was not readily observable. In the vicinity of rapidly changing topography, such as the shelf break, discontinuities were found. Discontinuities are not desirable as they may cause

false internal tide generation. Inspection of the two original datasets showed that they were offset from one another (Figure 2.2 (a)). A correction was applied to the GEBCO data (Figure 2.2 (b)), with the data shifted  $0.015^\circ$  to the west and  $0.005^\circ$  to the south (Figure 2.2 (c)). Despite this, discontinuities were still found when the data were combined (Figure 2.3 (a)) and hence a  $3 \times 3$  grid point mean smoothing filter was applied along the join boundary (Figure 2.3 (b)). The join boundary is defined by the location of any grid points from one dataset with at least one neighbouring grid point from another dataset.

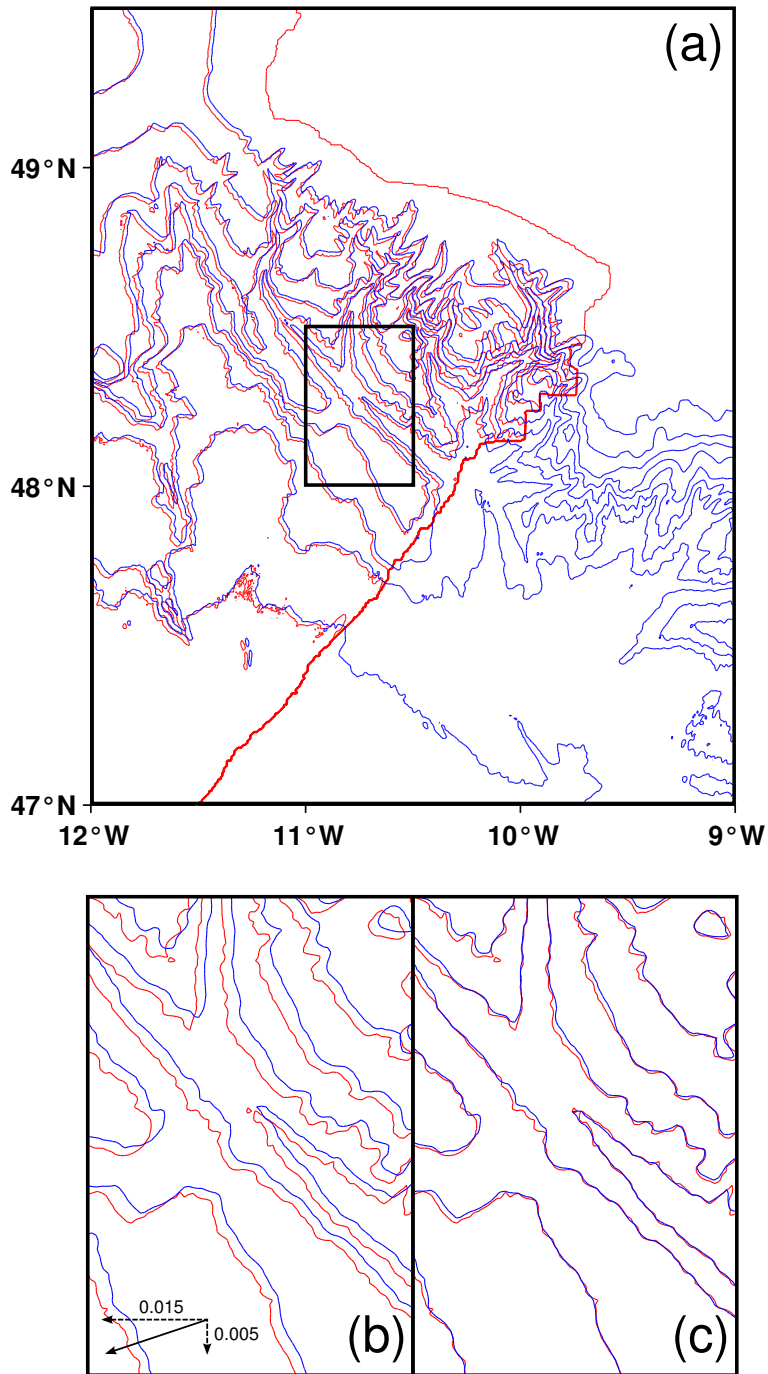


**Figure 2.2:** (a) GEBCO (blue) and INFOMAR (red) bathymetric contours plotted every 500 m (b) Offset between and GEBCO and INFOMAR bathymetry with correction used (degrees) shown in the bottom left hand corner (c) GEBCO and INFOMAR data after correction applied.

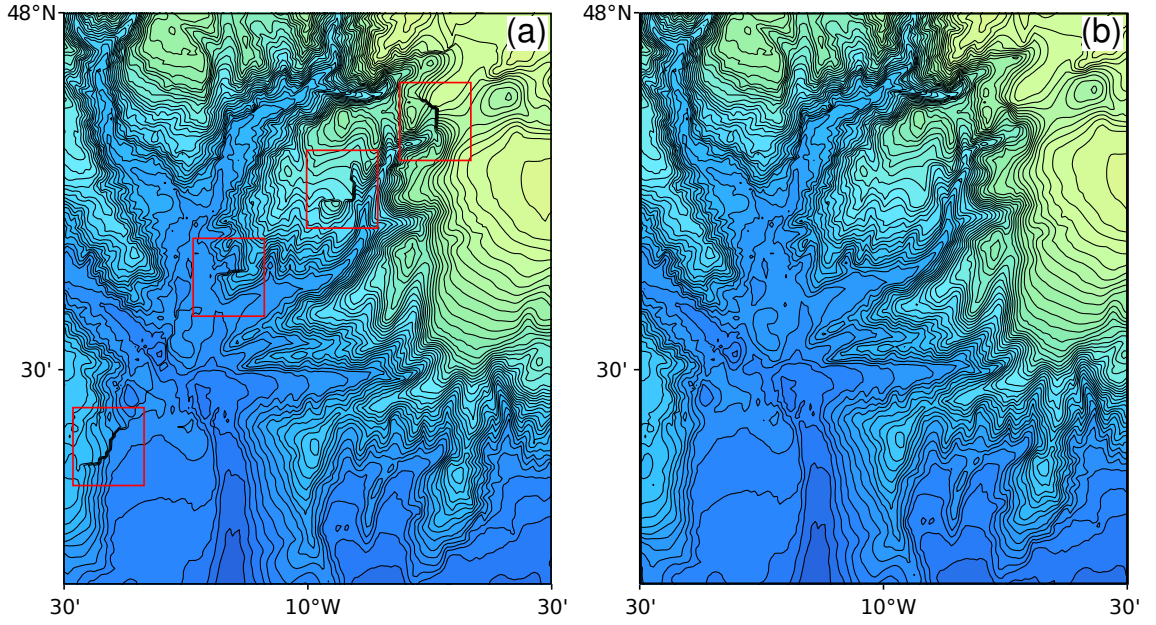


**Figure 2.3:** (a) Location of discontinuities found within combined bathymetry, highlighted by red boxes. (b) The same location as in (a) after smoothing carried out along the join boundary. Bathymetric contours are plotted every 100 m

### MODEL TIME STEPS

The model operates using a split time step: the external mode portion of the model is two-dimensional and uses a short time step based on the external wave speed, whilst the internal mode is three-dimensional and uses a longer time step based on the internal wave speed. This helps to deal with the rapid propagation of the external gravity wave relative to the much slower internal wave, thus improving computational efficiency. High horizontal resolution is necessary to resolve internal tide activity over Whittard Canyon, where the canyon varies in width from 30 km at the canyon mouth to 2 km at the canyon head. To achieve model stability, the high horizontal resolution requires a short external mode time step. The external mode time step ( $\Delta t_E$ ) is limited by the two-dimensional advective form of the Courant-Friedrichs-Levy (CFL) condition for computational stability (Blumberg and Mellor, 1987)

$$\Delta t_E \leq C_t^{-1} (\Delta x^{-2} + \Delta y^{-2})^{-\frac{1}{2}} \quad (2.1)$$

where  $\Delta x$  and  $\Delta y$  are the horizontal resolutions and  $C_t = 2(gH)^{\frac{1}{2}} + U_{max}$  where  $U_{max}$  is the expected maximum velocity. There are other restrictions on the time step, however in practice the CFL criterion is the most rigorous (Blumberg and Mellor,

1987). With  $\Delta x$  and  $\Delta y = 500\text{m}$  and  $H_{max} = 4860\text{ m}$ , the maximum external time step required is  $\approx 0.8\text{ s}$ . A  $\Delta t_E$  value of  $0.7\text{ s}$  is therefore used within all simulations.

The internal time step,  $\Delta t_I$ , has less stringent constraints because the fast external mode effects have been removed. The criteria is similar to that for the external mode and is given by

$$\Delta t_I \leq C_T^{-1} (\Delta x^{-2} + \Delta y^{-2})^{-\frac{1}{2}} \quad (2.2)$$

where  $C_T = 2C + U_{max}$ ; where  $C$  is the maximum internal gravity wave speed and  $U_{max}$  is the maximum advective speed. The ratio of the time steps  $\Delta t_I/\Delta t_E$  for coastal conditions is typically 30 - 80 (Blumberg and Mellor, 1987). For this study, the ratio is set to 40, giving a  $\Delta t_I$  of 28 s.

#### BOUNDARY CONDITIONS/FORCING

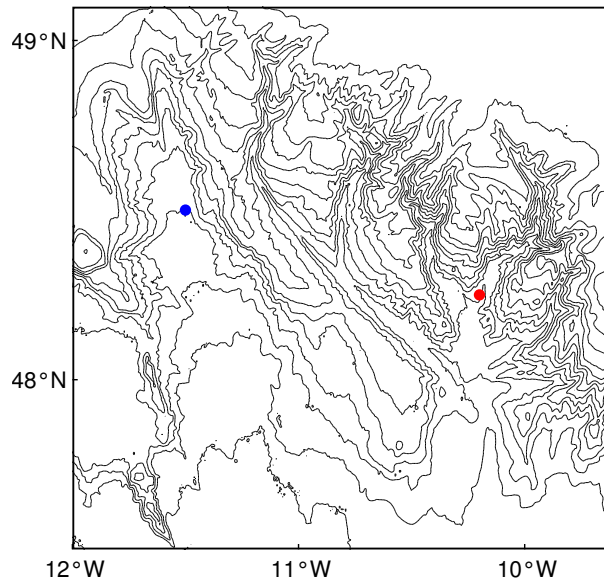
The model is forced at each boundary with the  $M_2$  (period 12.42 hours, angular frequency  $1.405 \times 10^{-4}\text{ rad s}^{-1}$ ) barotropic velocities and surface elevations extracted from the TPXO 7.2 inverse model of Egbert and Erofeeva (2002). A Flather boundary condition (Flather, 1976) is applied to the elevations and barotropic velocities at the domain boundaries, to let barotropic signals out of the domain, and a relaxation layer (10 grid cells) applied to the baroclinic velocities and isopycnal displacements to absorb baroclinic signals as per the method of Carter and Merrifield (2007). Both work to stop wave reflection back into the domain.

#### STRATIFICATION

The supply of freshwater to the Celtic Sea is small, therefore density is dominated by temperature variability and during the summer, strong seasonal stratification is established over areas where stirring by tides and wind is small compared to buoyancy input (Green et al., 2008). Although this seasonal stratification is not investigated in this work, two different potential temperature ( $\theta(z)$ ) and salinity profiles ( $S(z)$ ), *winter* and *summer*, are provided for reference. Two CTD profiles (vertical resolution of 2 m) located over the abyssal plain close to the mouth of Whittard Canyon were obtained from two different sources (Table 2.1). These profiles were linearly extrapolated to the maximum depth observed within the domain (4860 m) and smoothed using a 25-point gaussian window running mean. The resulting profiles are shown in Figure 2.5, however only the *summer* profile is used in all simulations.

**Table 2.1:** Details of CTD profiles used to create *summer* and *winter* stratification profiles

<i>Stratification</i>	<i>Latitude</i>	<i>Longitude</i>	<i>Depth</i>	<i>Date</i>	<i>Source</i>
<i>summer</i>	48°15'56"N	10°11'55"W	3525 m	12/07/09	JC36 cruise (NOC Southampton)
<i>winter</i>	48°31'51"N	11°31'9"W	3447 m	27/01/94	OMEX I cruise (BODC)

**Figure 2.4:** Locations of CTD profiles used to create *summer* (red) and *winter* (blue) stratification profiles.

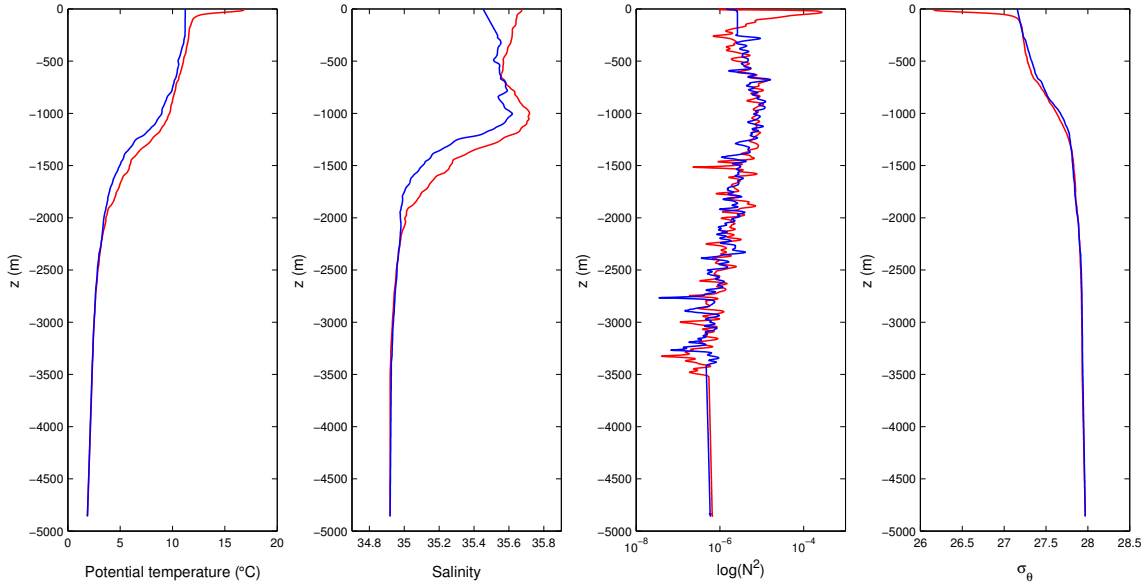


**Figure 2.5:** Potential temperature, salinity, buoyancy frequency and potential density profiles for *summer* (red) and *winter* (blue) stratification cases.

Fifty-one evenly distributed sigma levels are used within all simulations. High vertical resolution is obtained by using this number of sigma levels, resulting in resolutions of less than 1 m on the shelf and up to 97 m over the abyssal plain. This appears to adequately represent most of the variation in the salinity and temperature fields (Figure 2.6 (a,b)) throughout the full depth of the water column. The thermocline that is developed within the summer months is not as well resolved as the rest of the water column. An alternative would be to use a logarithmic distribution with more sigma levels concentrated within the upper water column. Although this would help to better resolve the upper water column thermal structure, information would be lost throughout the rest of the water column. For internal tide processes, as much detail about the middle part of the water column is required as at the surface, hence evenly distributed sigma levels are desirable. In shallower water, at depths encountered within Whittard Canyon (e.g. 2000 m), the thermocline is better resolved (Figure 2.6 (c,d)).

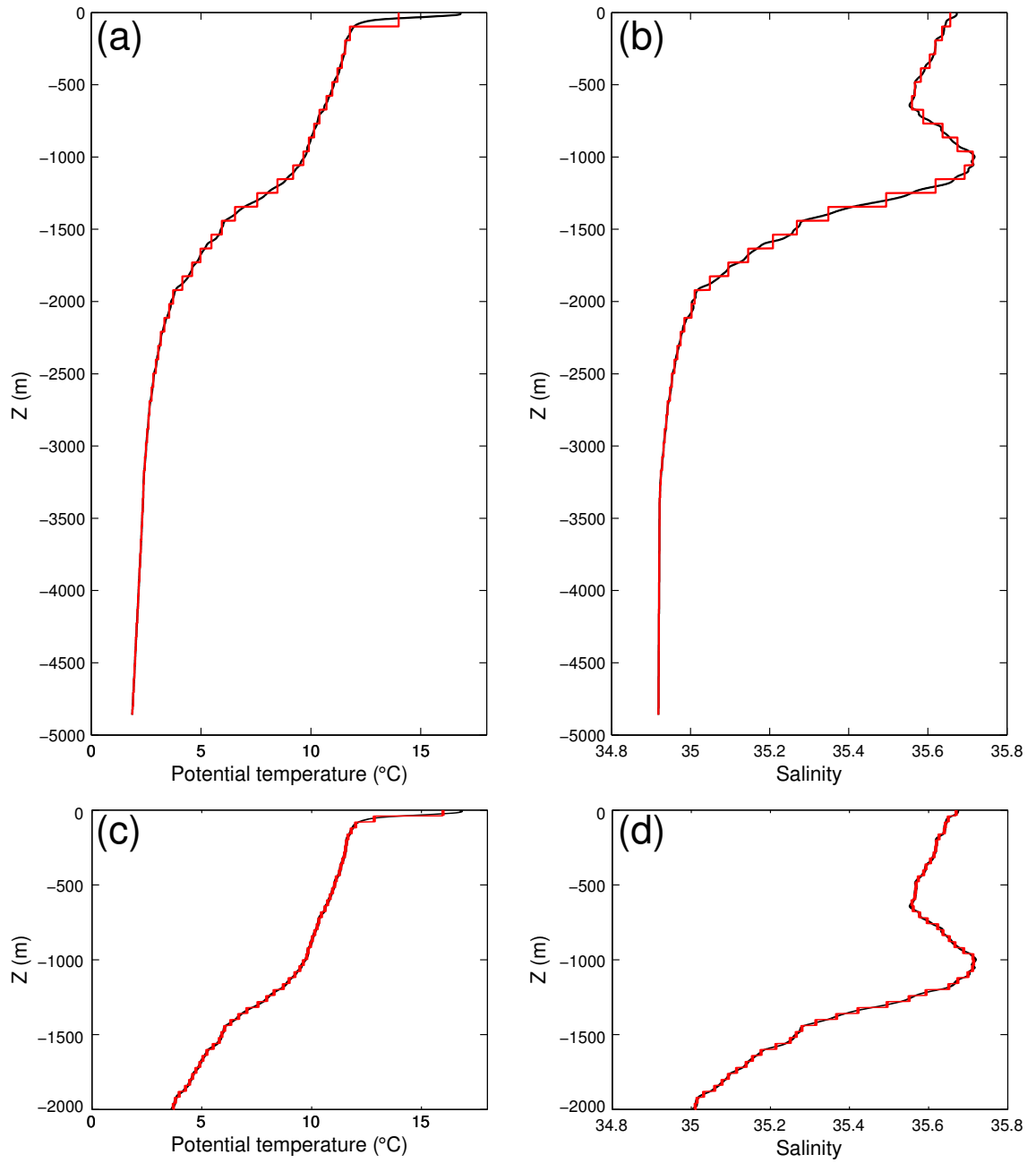


**Figure 2.6:** Comparison between measured salinity and temperature profiles (black) and profiles averaged over 51 sigma levels (red) for: (a,b) Full depth profiles and (c,d) Profile depths of 2000 m (representative of canyon head depths)

### 2.2.3 DIAGNOSTICS

#### BAROCLINIC ENERGY FLUX

Baroclinic energy flux  $\mathbf{F}$  is a useful metric with which to quantify internal tide energetics and is given by

$$\mathbf{F} = \langle \mathbf{u}' p' \rangle \quad (2.3)$$

where  $\mathbf{u}'$  is the baroclinic velocity perturbation,  $p'$  is the pressure perturbation induced by the passage of internal tides and  $\langle \rangle$  indicates an average over a tidal cycle (Kunze et al., 2002; Nash et al., 2005). The total horizontal velocity in the model,  $\mathbf{u}_{tot}$ , may be decomposed as

$$\mathbf{u}_{tot} = \mathbf{u}'_{tot} + \bar{\mathbf{u}}_{tot} \quad (2.4)$$

where  $\mathbf{u}'_{tot}$  is the horizontal velocity perturbation caused by the passage of surface and internal tides and  $\bar{\mathbf{u}}_{tot}$  is the time averaged, or residual, horizontal flow. In both cases,  $\mathbf{u} = [u, v]$ , where  $u$  is the zonal velocity (positive eastward) and  $v$  is the meridional velocity (positive northward). An  $M_2$  period harmonic fit is made to  $\mathbf{u}_{tot}$  using least-square methods and the harmonic constants, amplitude (subscript *amp*) and phase ( $\phi$ ), outputted as per the relationship shown in Figure 2.7 (a). The time-dependant nature of the harmonic fit means that only the velocity perturbation ( $\mathbf{u}'_{tot}$ ), and not the constant residual flow ( $\bar{\mathbf{u}}_{tot}$ ), are characterised by the harmonic output. The  $M_2$  barotropic horizontal velocity perturbation,  $\mathbf{u}'_{Bt}$ , is estimated as the depth-averaged horizontal velocity perturbation,

$$\mathbf{u}'_{Bt} = \frac{1}{H} \int_{-H}^0 \mathbf{u}'_{tot} dz \quad (2.5)$$

where  $H$  is the water depth. This study is mainly concerned with the  $M_2$  baroclinic perturbations,  $\mathbf{u}'$ , defined as

$$\mathbf{u}' = \mathbf{u}'_{tot} - \mathbf{u}'_{Bt} \quad (2.6)$$

For ease of calculation later,  $\mathbf{u}'$  is complex-demodulated into real and imaginary parts as per the relationship show in Figure 2.7 (b) and hence,

$$\mathbf{u}' = [u', v'] = [(u'_{amp}, \phi_{u'}), (v'_{amp}, \phi_{v'})] = [(u'_r, u'_i), (v'_r, v'_i)] \quad (2.7)$$

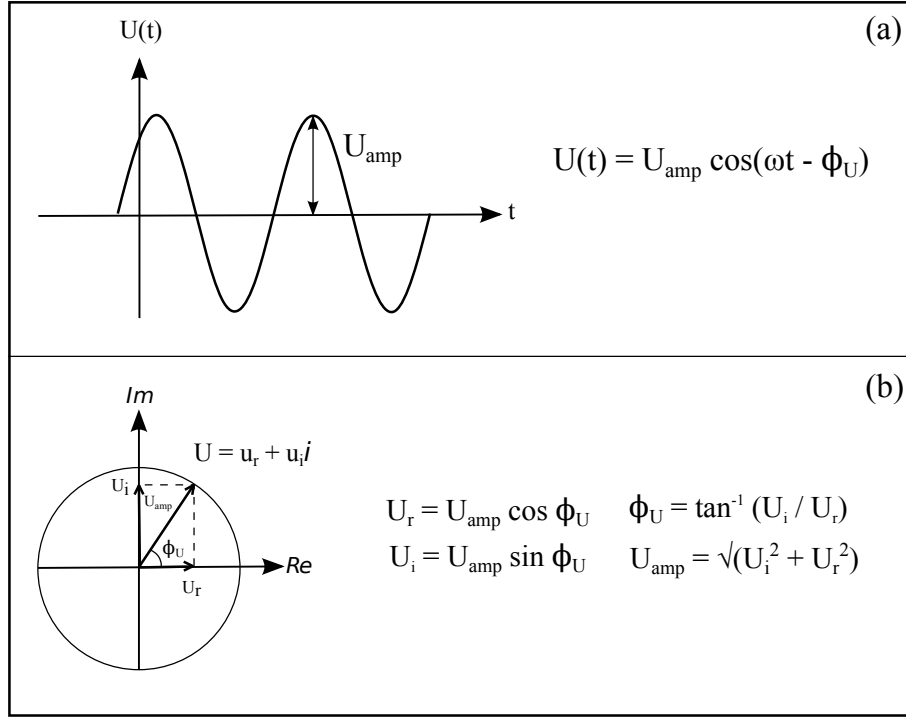


**Figure 2.7:** (a) Schematic showing a time-series of a generic velocity  $U$  and how a harmonic fit to the signal can be represented using amplitude,  $U_{amp}$ , phase,  $\phi_U$  and  $\omega$ , the frequency of the signal ( $\text{rad s}^{-1}$ ) (b) Schematic showing the relationship between a generic velocity  $U$ , its real and imaginary components,  $U_r$  and  $U_i$  and phase and amplitude,  $\phi_U$  and  $U_{amp}$

The pressure perturbation is calculated by assuming a hydrostatic balance,

$$0 = -\frac{\partial p'}{\partial z} + b \quad (2.8)$$

where  $b$  is buoyancy. This assumption is valid for frequencies  $\omega \ll N$  and so should be appropriate for the semidiurnal fluctuations focused on in this study. Integrating Equation (2.8) with depth following Kunze et al. (2002) gives

$$p'(z) = -\int_{-z}^0 b(z') dz' + p'_{surf} \quad (2.9)$$

The buoyancy term  $b = -\rho_0 N^2 \xi$  and is calculated using  $\rho_0$ , the density of seawater ( $1025 \text{ kg m}^{-3}$ ),  $N^2(z)$ , the model stratification, and  $\xi(z)$ , vertical isopycnal displacement profiles, which are estimated from  $M_2$  vertical velocity profiles  $w(z)$  (positive upwards) using,

$$[\xi_r, \xi_i] = [-w_i, w_r] / \omega \quad (2.10)$$

where  $\omega$  is the angular frequency of the  $M_2$  internal tide ( $1.405 \times 10^{-4} \text{ rad s}^{-1}$ ) and the subscripts  $r$  and  $i$  indicate the real and imaginary parts of the complex-demodulation of  $w$  where

$$w = (w_{amp}, \phi_w) = (w_r, w_i) \quad (2.11)$$

The constant of integration in Equation (2.9),  $p_{surf}$ , can be constrained by using the baroclinicity condition for pressure,  $\int_{-H}^0 p' dz = 0$  (Kunze et al., 2002) giving

$$p'(z) = \rho_0 \int_z^0 N^2(z') \xi(z') dz' - \frac{\rho_0}{H} \int_{-H}^0 \int_z^0 \rho N^2(z') \xi(z') dz' dz \quad (2.12)$$

Finally, the horizontal components of the baroclinic energy flux are defined as

$$F_x = \frac{1}{2} [p'_r u'_r + p'_i u'_i] \quad (\text{W m}^{-1}) \quad (2.13)$$

$$F_y = \frac{1}{2} [p'_r v'_r + p'_i v'_i] \quad (\text{W m}^{-1}) \quad (2.14)$$

#### BAROCLINIC FLUX DIVERGENCE

Baroclinic flux divergence ( $\nabla \cdot \mathbf{F}$ ) is a measure of the amount of baroclinic energy that is radiated from a geographic point (Carter et al., 2008). The domain-averaged baroclinic energy flux divergence is given by

$$\overline{\nabla \cdot \mathbf{F}} = \frac{1}{A} \int \nabla \cdot \mathbf{F} dx dy \quad (\text{W m}^{-2}) \quad (2.15)$$

where  $A$  is the domain area. The domain-integrated baroclinic energy flux divergence is therefore  $A \overline{\nabla \cdot \mathbf{F}}$  and is a measure of the rate at which baroclinic energy radiates out of the domain. Negative values imply positive convergence, i.e. the concentration of baroclinic energy within a region.

#### BAROTROPIC-TO-BAROCLINIC ENERGY CONVERSION

The magnitude of barotropic to baroclinic tidal energy conversion is given by

$$E_{conv} = \langle p'(-H) w_{Bt} \rangle \quad (\text{W m}^{-2}) \quad (2.16)$$

where  $\langle \rangle$  indicates an average over a tidal cycle,  $p'(-H)$  is the pressure perturbation at the bottom and  $w_{Bt}$  is the barotropic vertical velocity at the bottom (Niwa and Hibiya, 2001; Zilberman et al., 2009). The vertical velocity,  $w_{Bt}$ , is caused by barotropic flow

across sloping topography, and is given by

$$w_{Bt} = -\mathbf{u}'_{Bt} \cdot \nabla H \quad (2.17)$$

where  $\mathbf{u}'_{Bt}$  is the depth-averaged velocity from the harmonic output of the model (Equation (2.5)) and  $H$  is the water depth (Garrett and Kunze, 2007). Positive values of  $E_{conv}$  indicate the transfer of energy from the barotropic tide to the baroclinic tide, whilst negative values are a measure of energy transfer due to the pressure work done on the barotropic tide by the baroclinic tide (Zilberman et al., 2009). We define the domain-averaged energy conversion as

$$\bar{E}_{conv} = \frac{1}{A} \int E_{conv} dx dy \quad (\text{W m}^{-2}) \quad (2.18)$$

where  $A$  is the domain area. The domain-integrated energy conversion is therefore  $A\bar{E}_{conv}$ .

#### INTERNAL WAVE KINETIC AND POTENTIAL ENERGY

Baroclinic horizontal kinetic energy (HKE) density is calculated using

$$\text{HKE} = \frac{1}{4} \rho_0 \left( u'^2_{amp} + v'^2_{amp} \right) \quad (2.19)$$

where  $u'_{amp}$  and  $v'_{amp}$  are perpendicular baroclinic velocity amplitudes. Baroclinic available potential energy (APE) density is approximated using linear theory (Kang and Fringer, 2012) as

$$\text{APE} = \frac{1}{4} \rho_0 N^2 \xi^2_{amp} \quad (2.20)$$

where  $\xi_{amp}$  is the amplitude of vertical displacement caused by the internal tide calculated from vertical velocity profiles as per Equations (2.10, 2.11). For linear progressive internal waves with frequencies  $\omega \ll N$  (Gill, 1982), the theoretical relationship between HKE and APE is

$$\text{HKE/APE} = \frac{\omega^2 + f^2}{\omega^2 - f^2} \quad (2.21)$$

The theoretical value of HKE/APE for a latitude representative of this study region (48°N) is 3.99.

## 2.3 CONTROL RUN

For the purposes of defining the control run, the *summer* stratification case was used in all simulations and all simulations initially run for 21  $M_2$  tidal cycles. To make descriptions clearer, Figure 2.8 outlines the numbering convention for the various Whittard Canyon limbs that is used in this study.

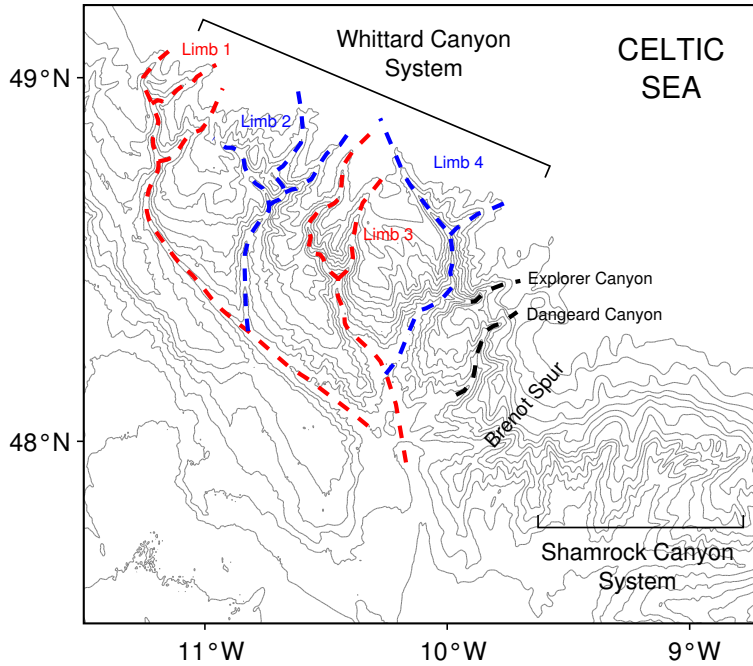


**Figure 2.8:** The Whittard Canyon system and surrounding region. Contours are plotted every 300 m

### 2.3.1 DOMAIN SIZE SENSITIVITY

The sensitivity of the model to domain size was considered by running the model with small (*wc01*), medium (*wc02*) and large (*wc03*) domain sizes as defined in Table 2.2 and shown in Figure 2.9. To accurately simulate the internal wavefield within Whittard Canyon, the domain must contain all the major generation sites within the region, however, the larger the domain size, the more computationally expensive each simulation becomes. Baroclinic energy conversion and baroclinic energy flux divergence are integrated and averaged over each domain, and also over the Whittard Canyon and Shamrock Canyon systems as shown in Figure 2.10 (c). Note that the Whittard Canyon system region is slightly smaller than *wc01* and hence values

integrated and averaged over the entire domain are different to those calculated for just the canyon.

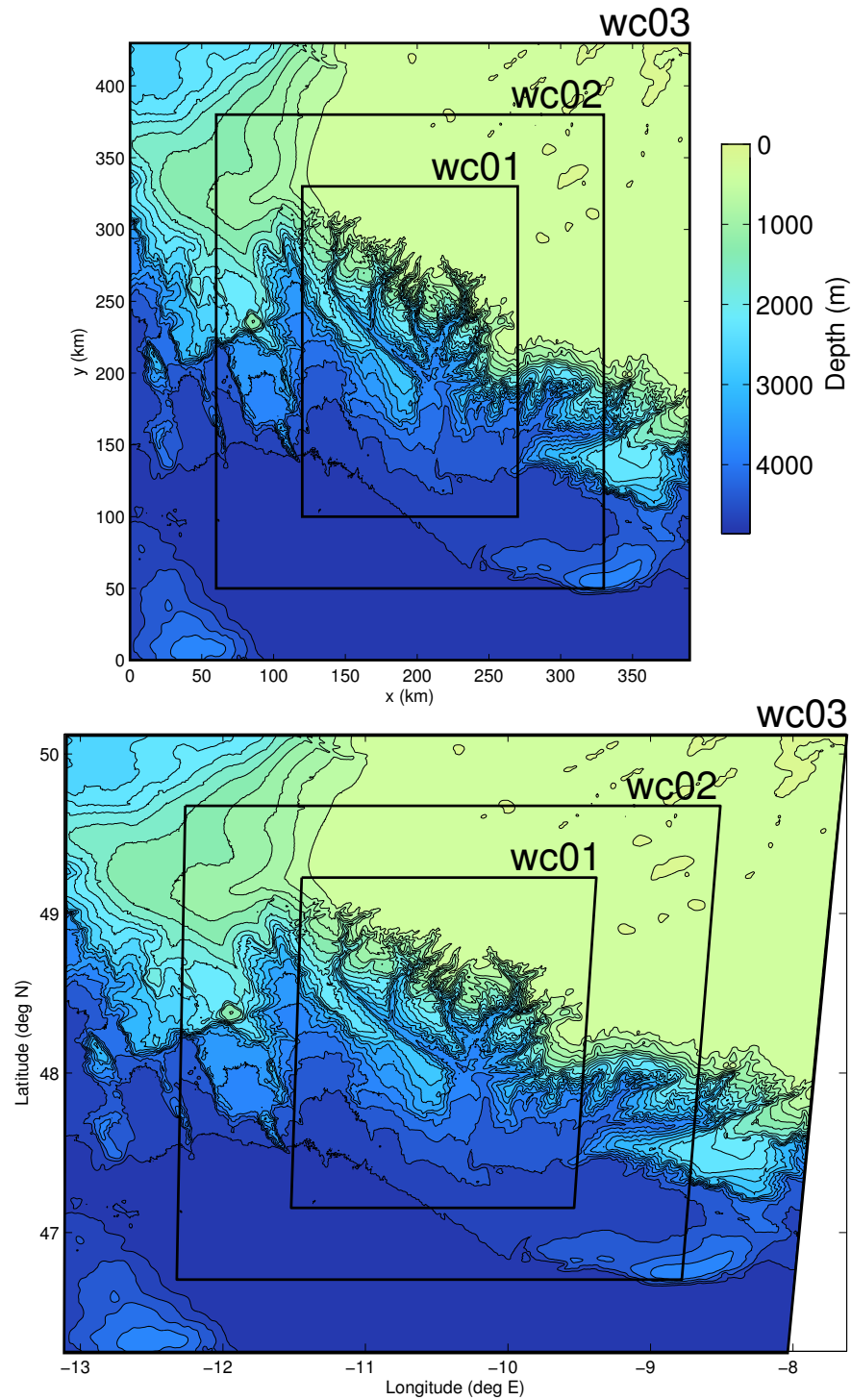


**Figure 2.9:** Domain sizes for model runs *wc01*, *wc02*, *wc03* mapped onto cartesian space (top) and geographic latitude and longitude (bottom). Contours are plotted every 300 m

<i>Model run</i>	<i>L<sub>x</sub> (km)</i>	<i>L<sub>y</sub> (km)</i>	<i>Grid size</i>	<i>Run time</i>
<i>wc01</i>	150	230	301 x 461	9 hours
<i>wc02</i>	270	330	541 x 661	38 hours
<i>wc03</i>	390	430	781 x 861	46 hours

**Table 2.2:** Model runs for diagnosing domain size including run time on GRACE (High powered computing cluster)

### BAROTROPIC-TO-BAROCLINIC ENERGY CONVERSION

The spatial pattern of barotropic-to-baroclinic energy conversion in all three model runs is similar (Figure 2.10), positive and negative conversion occurs predominantly at the shelf break where the topography is most complex, whilst there is little or no conversion in the rest of the domain. There is roughly twice as much positive conversion as there is negative conversion within the canyon for all domain sizes; total negative conversion as a percentage of total positive conversion within Whittard Canyon for the different domain sizes is 41.5% (*wc01*), 45.2% (*wc02*) and 45.2% (*wc03*). Negative conversion typically indicates multiple generation sites, and arises from the phase differences between locally and remotely generated internal tides (Zilberman et al., 2009; Kelly and Nash, 2010). Areas of positive conversion within the canyon do appear to lie adjacent to “shadow regions” of negative conversion, therefore internal tide generation is at least partially balanced by pressure work done on the barotropic tide by the baroclinic tide. Within the *wc01* model run, the main areas of barotropic-to-baroclinic energy conversion occur over the region covered by limb 4 of Whittard Canyon and the uppermost reaches of limb 2 (Figure 2.10a). This pattern is replicated in both the *wc02* and *wc03* model runs (Figures 2.10 (b,c)), however another major generation site is introduced by extending the domain to the east, towards Shamrock Canyon.

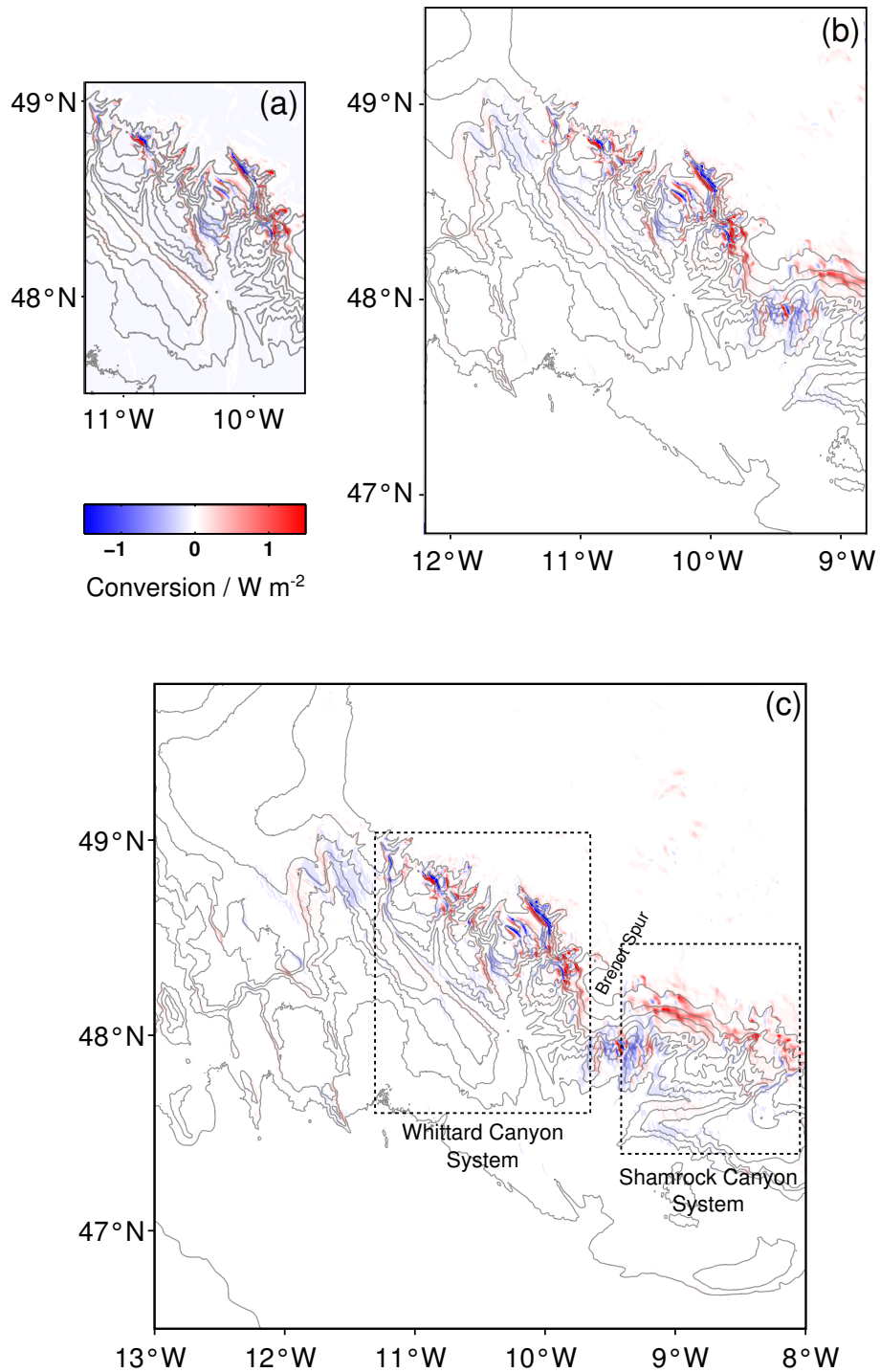


**Figure 2.10:**  $M_2$  barotropic to baroclinic energy conversion,  $E_{conv}$ , for model runs: (a) *wc01*, (b) *wc02* and (c) *wc03*. Depth contours are plotted every 500 m.

The domain-integrated barotropic-to-baroclinic energy conversion within each model run increases with increasing domain size, from 0.35 GW in *wc01*, to 1.17 GW in *wc03* (Table 2.3). However, the domain-averaged barotropic-to-baroclinic

energy conversion within each model run decreases with increasing domain size, from  $11.3 \text{ mW m}^{-2}$  in *wc01*, to  $7.3 \text{ mW m}^{-2}$  in *wc03* (Table 2.3). These opposing trends are likely due to the large areas of little or no conversion that dominate when the larger domain sizes are used. When the region containing only Whittard Canyon is considered, however, both the area-integrated and area-averaged conversion are largest in the *wc02* model run ( $0.35 \text{ GW}$  and  $14.2 \text{ mW m}^{-2}$ , respectively, Table 2.3), but only marginally so. Significant generation also occurs over Shamrock Canyon; in model run *wc03* (the only model run to contain the entire Shamrock Canyon system), the area-integrated conversion over the Shamrock Canyon region is  $0.34 \text{ GW}$ , identical to the conversion within Whittard Canyon for the same model run. To identify whether any of the baroclinic energy generated in Shamrock Canyon enters Whittard Canyon, the baroclinic energy fluxes must be considered.

Model run	Region	Area-integrated	Area-averaged
		$E_{conv}$ (GW)	$E_{conv}$ ( $\text{mWm}^{-2}$ )
<i>wc01</i>	Entire domain	0.35	11.3
	Whittard Canyon	<b>0.33</b>	<b>14.6</b>
	Shamrock Canyon	-	-
<i>wc02</i>	Entire domain	0.65	7.8
	Whittard Canyon	<b>0.35</b>	<b>14.2</b>
	Shamrock Canyon (partial)	0.17	33.8
<i>wc03</i>	Entire domain	1.17	7.3
	Whittard Canyon	<b>0.34</b>	<b>16.0</b>
	Shamrock Canyon	0.34	34.2

**Table 2.3:** Area-integrated and area-averaged barotropic to baroclinic energy conversion in the *wc01*, *wc02* and *wc03* model runs for each entire domain, and within each domain, the Whittard Canyon region and the Shamrock Canyon region (only *wc03* contains this complete region).

### BAROCLINIC ENERGY FLUX

The spatial pattern of depth-integrated baroclinic energy flux within model runs *wc02* and *wc03* (Figures 2.11 (b,c)) is similar; however there is a very different pattern in the *wc01* run (Figure 2.11 (a)). The smallest domain *wc01* is clearly missing a key generation site (Shamrock Canyon) and is thus not an appropriate domain size to use for this study. Peak depth-integrated baroclinic energy fluxes occur within Whittard Canyon in every model run ( $7.5$ ,  $12.8$  and  $11.2 \text{ kW m}^{-1}$  in *wc01*, *wc02* and *wc03*,

respectively), with the highest value occurring in *wc02*. When the spatial pattern of baroclinic energy flux in the region covered by Whittard Canyon is looked at in more detail, *wc01* (Figure 2.12 (a)) is still markedly different to the other two model runs, both of which show a similar spatial pattern. The northwest propagating beam appears strongest in *wc02* (Figure 2.12 (b)) compared to *wc03* (Figure 2.12 (c)). When the baroclinic energy flux magnitude from the *wc02* run is subtracted from that of *wc01*, there is significantly less baroclinic energy along the eastern shelf edge and limb 4 of the canyon in the smallest domain size run (Figure 2.12 (d)), indicating that the generation sites to the east are important to include, in order to model the dynamics of the internal tide in this region accurately. When the baroclinic energy flux magnitude from the *wc03* run is subtracted from that of *wc02*, there is significantly more baroclinic energy along the eastern shelf edge and limb 4 of the canyon and a reduction in energy in other parts of the canyon, most noticeably along the lower reaches of limb 1 (Figure 2.12 (e)).

Model run	Region	Area-integrated $\nabla \cdot \mathbf{F}$ (GW)	Area-averaged $\nabla \cdot \mathbf{F}$ ( $\text{mWm}^{-2}$ )
<i>wc01</i>	Entire domain	0.07	2.21
	Whittard Canyon	<b>0.05</b>	<b>2.20</b>
	Shamrock Canyon	-	-
<i>wc02</i>	Entire domain	0.12	1.50
	Whittard Canyon	<b>-0.04</b>	<b>-1.90</b>
	Shamrock Canyon (partial)	0.11	17.7
<i>wc03</i>	Entire domain	0.22	1.40
	Whittard Canyon	<b>-0.05</b>	<b>-2.20</b>
	Shamrock Canyon	0.12	12.1

**Table 2.4:** Area-integrated and area-averaged baroclinic energy flux divergence in the *wc01*, *wc02* and *wc03* model runs for the Whittard Canyon region (bold) and the whole domain.

The domain-integrated baroclinic energy flux divergence (the amount of baroclinic energy radiating out of the domain) increases with increasing domain size; from 0.07 GW in *wc01*, to 0.22 GW in *wc03* (Table 2.4). When only Whittard Canyon is considered, in *wc01* there is positive divergence (0.05 GW) in the canyon region, indicating that baroclinic energy is leaving the canyon. In runs *wc02* and *wc03*, there is negative divergence within the canyon (-0.04 and -0.05 GW, respectively), indicating that baroclinic energy is converging on the canyon and also providing evidence that Shamrock Canyon is an important source of baroclinic energy to Whittard

Canyon. However, the similarity between the baroclinic energy flux divergence within Whittard Canyon for runs *wc02* and *wc03* seems to suggest that although *wc02* only contains a portion of Shamrock Canyon, it contains the key generation sites that contribute baroclinic energy to Whittard Canyon. This can be seen in Figure 2.11 (c) where it is clear that a large proportion of baroclinic energy from Shamrock Canyon is not diverted northwards along the shelf edge, but instead travels southwestwards onto the abyssal plain. Given the computational expense of running a larger domain size, it seems appropriate to use the *wc02* domain size, as it appears to capture the main generation regions and features of the internal wavefield within this region despite its smaller size.

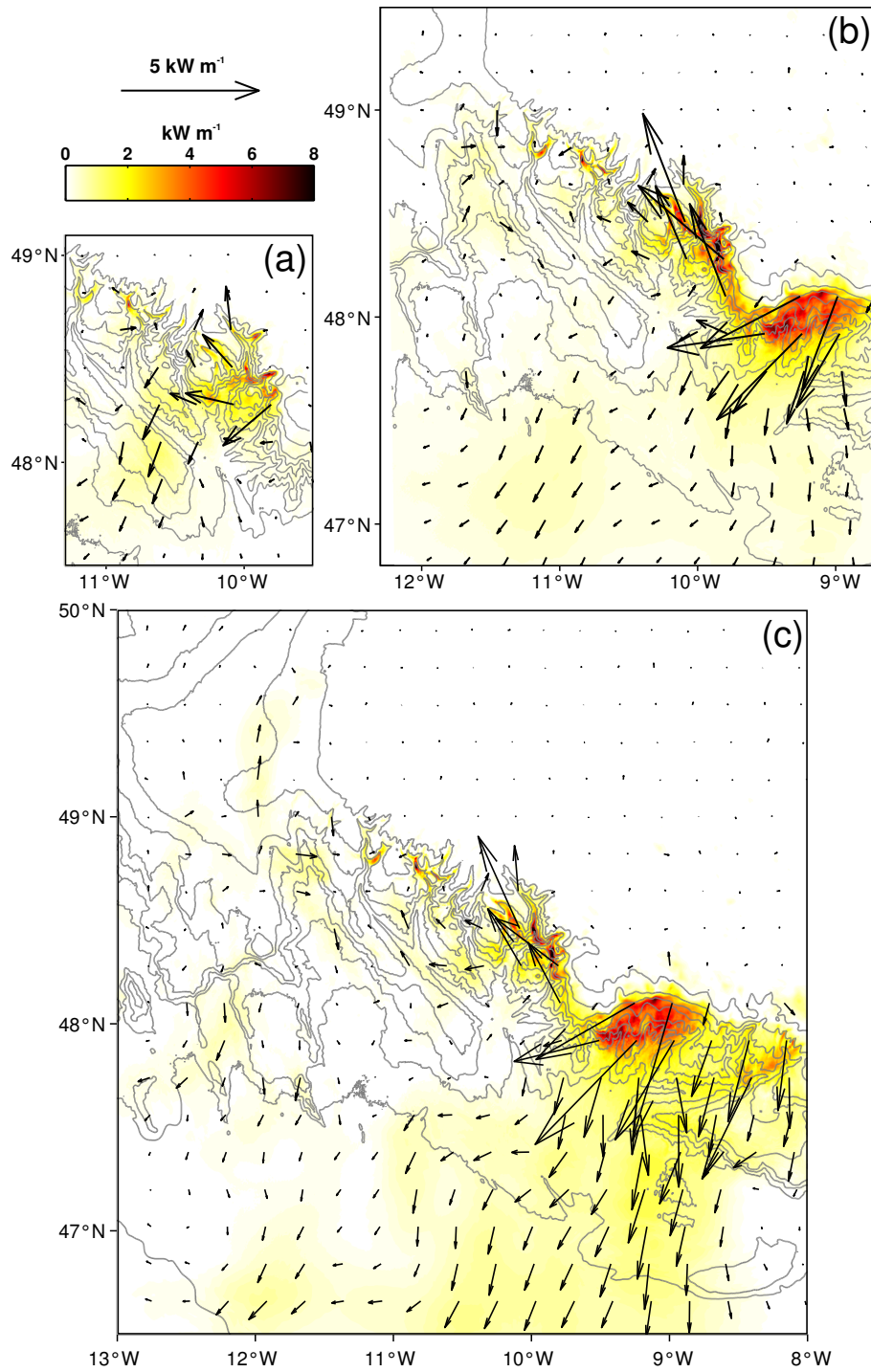


**Figure 2.11:** Depth-integrated baroclinic  $M_2$  energy flux for model runs (a) *wc01*, (b) *wc02* and (c) *wc03*. Vectors are plotted every 40 model grid points ( $\approx 20$  km) in each direction. The underlying colour is the energy flux magnitude. Depth contours are plotted every 300 m.

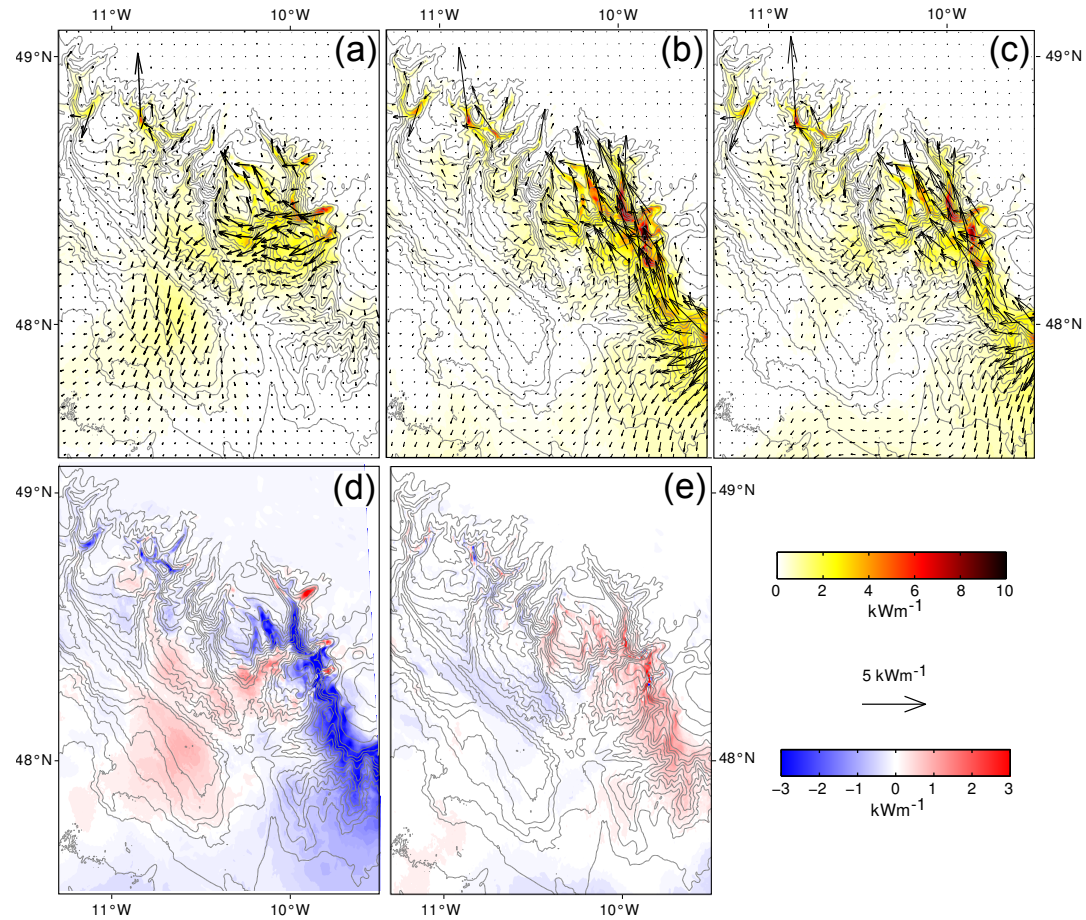


**Figure 2.12:** Depth-integrated baroclinic  $M_2$  energy flux in Whittard Canyon for model runs: (a) *wc01*, (b) *wc02* and (c) *wc03*. Vectors are plotted every 10 model grid points ( $\approx 5$  km) in each direction. The underlying colour is the energy flux magnitude. Depth contours are plotted every 300 m. The difference in energy flux magnitude between *wc01* and *wc02* ( $wc01 - wc02$ ) is shown in (d). The difference in energy flux magnitude between *wc02* and *wc03* ( $wc02 - wc03$ ) is shown in (e).

### 2.3.2 RUN LENGTH SENSITIVITY

The initial ‘control’ run length (21 tidal cycles) was extended by a further 22 tidal cycles, reaching a maximum of 43 tidal cycles, to check whether steady state conditions are reached within 21 tidal cycles (used for all preceding simulations) and to observe whether an identifiable pressure gradient error develops within the domain. The sigma-coordinate pressure gradient error is a disadvantage of using a sigma-coordinate system (Mellor et al., 1994). It arises because the sigma lines are not coincident with lines of constant density, therefore the coordinates can’t recreate the condition of zero horizontal hydrostatic pressure gradient when a horizontally uniform free surface and density field are present (Carter et al., 2012). This produces across-slope flow which can be of similar magnitude to that of weak internal wave currents, even though there should be no flow. The size of this error is dependant upon the topographic slope, therefore smoothing the domain can reduce the error (Carter et al., 2012).

#### VELOCITY TIME-SERIES

Model ‘virtual moorings’ were placed at  $48^{\circ}\text{N } 10.2^{\circ}\text{W}$  and  $48.5^{\circ}\text{N } 9.94^{\circ}\text{W}$  so that a time series of the velocity fields, rather than the harmonic constants, would be output. The two locations were chosen as they lie within the canyon: the first within the deeper part of the canyon, and the second within the upper reaches, where the high topographic variability makes it more likely that the pressure gradient error may develop.

The time-series of northward and eastward velocity (Figures 2.13 and 2.14) at both virtual mooring locations show that roughly a steady state has been reached by the point over which the harmonic analysis for the 21 tidal cycle run is calculated (10 to 21 tidal cycles). Furthermore, there is no indication within the time series that a pressure gradient error is developing. To confirm this, zero-forcing simulations were run; without any forcing there should be no baroclinic motion, therefore any baroclinic activity occurring within such a simulation would indicate a pressure gradient error. Zero-forcing simulations run for 21, 32 and 43 tidal cycles show no baroclinic activity, suggesting no pressure gradient error.

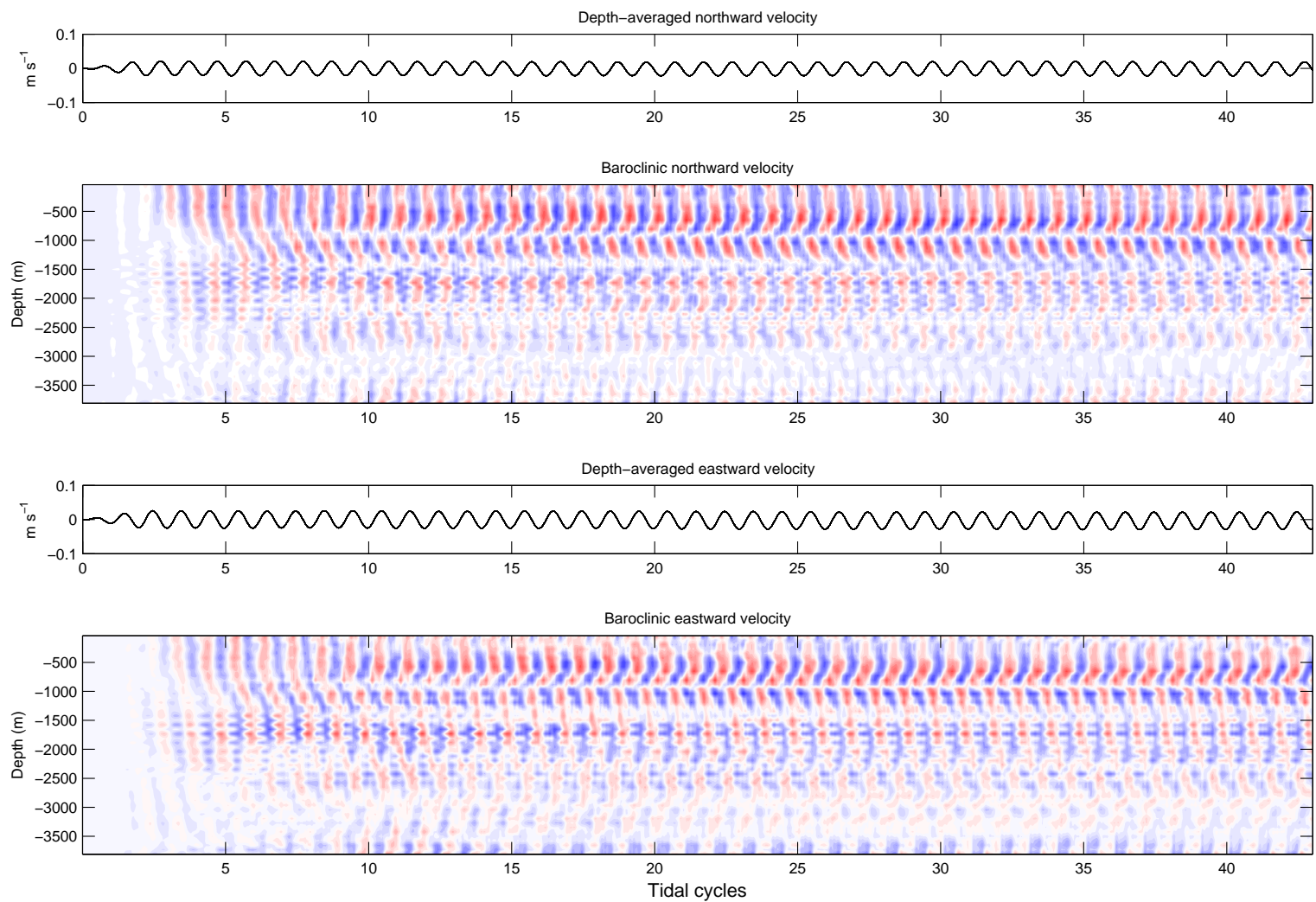


**Figure 2.13:** Horizontal current velocity time series from virtual mooring at location 1 (48°N 10.2°W)

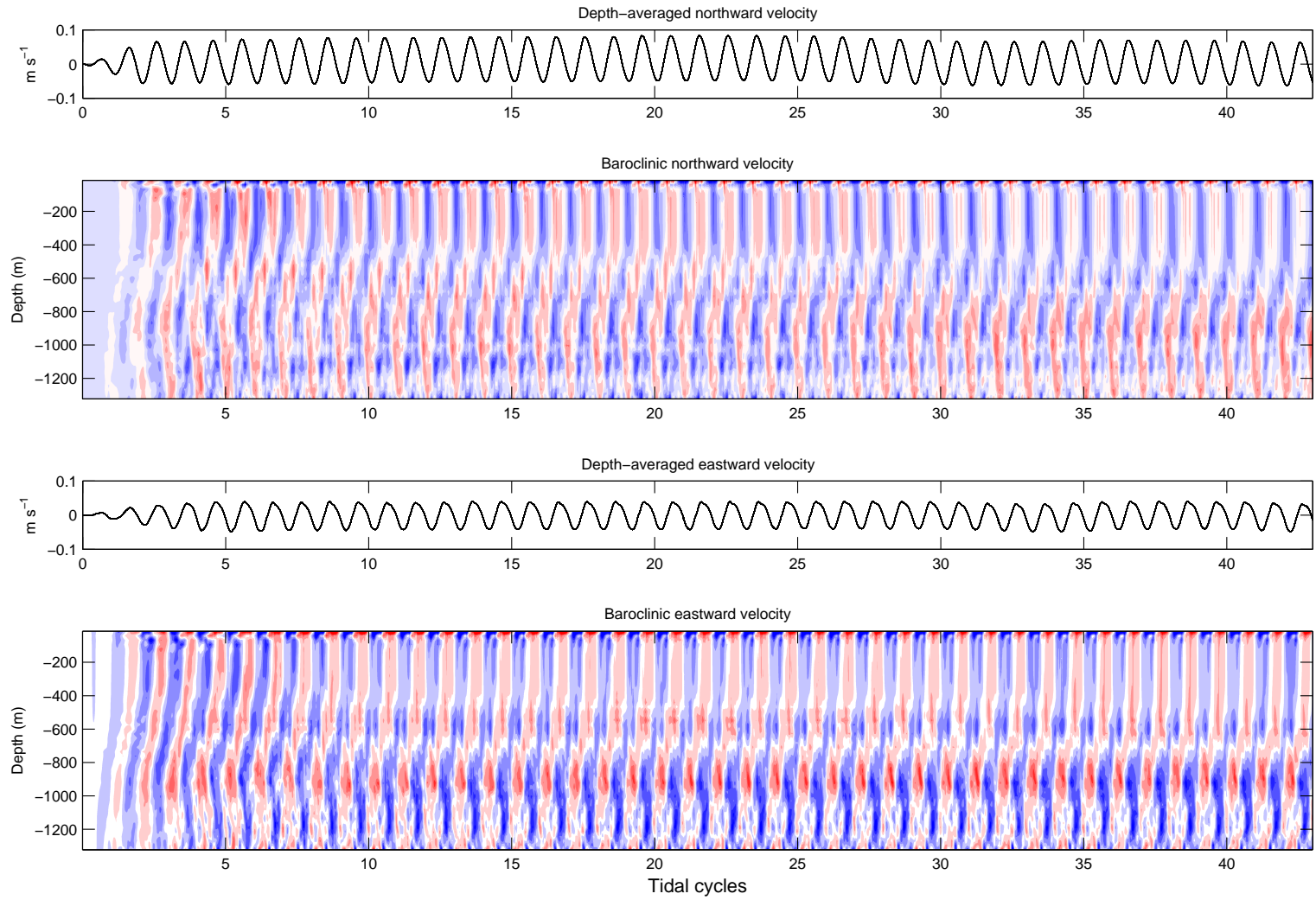


**Figure 2.14:** Horizontal current velocity time series from virtual mooring at location 2 (48.5°N 9.94°W)

### BAROTROPIC-TO-BAROCLINIC ENERGY CONVERSION

As expected, increasing the simulation run length doesn't change the pattern of barotropic-to-baroclinic conversion seen in Figure 2.10 (b) due its primary dependence on topographic slope, which remains the same for all run lengths. The domain-integrated and domain-averaged barotropic-to-baroclinic energy conversion values for all run lengths are within 1% of one another (Table 2.5) and, although not clearly apparent in the velocity time series (Figures 2.13 and 2.14), show that the model reaches steady state by 32 cycles.

Model run	Region	Area-integrated $E_{conv}$ (GW)	Area-averaged $E_{conv}$ (mWm <sup>-2</sup> )
21 cycles	Entire domain	0.65	7.8
	Whittard Canyon	<b>0.33</b>	<b>14.2</b>
	Shamrock Canyon	0.17	33.8
32 cycles	Entire domain	0.66	7.9
	Whittard Canyon	<b>0.32</b>	<b>14.2</b>
	Shamrock Canyon	0.17	33.5
43 cycles	Entire domain	0.66	7.9
	Whittard Canyon	<b>0.32</b>	<b>14.2</b>
	Shamrock Canyon	0.17	33.5

**Table 2.5:** Domain-integrated and domain-averaged barotropic to baroclinic energy conversion in the 21, 32 and 43 tidal cycle model runs for each entire domain, and within each domain, the Whittard Canyon region and the Shamrock Canyon region.

### BAROCLINIC ENERGY FLUX

The spatial pattern of depth-integrated baroclinic energy flux in Whittard Canyon is similar for all run lengths (Figure 2.15), however there are regions (upper reaches of limb 2 and mid-limb 4) where the magnitude is increased in the 32 cycle and 43 cycle runs (Figures 2.15 (b,c)). When the difference in baroclinic energy flux magnitude between the 21 cycle and 32 cycle runs is calculated (Figure 2.15 (d)), the variations in baroclinic energy magnitude between the two are clearer; there are decreases in magnitude of up to 3 kW m<sup>-1</sup> as well as increases in magnitude of up to 6 kW m<sup>-1</sup>. The domain-integrated and domain-averaged barotropic-to-baroclinic energy flux divergence values for all run lengths are within 1% of one another (Table 2.6) and as with Section 2.3.2 show that the model reaches steady state by 32 cycles. The

'standard' run length of 21 cycles is therefore extended to 32 cycles for all following simulations.

	<b>Model run</b>		
	<i>21 cycles</i>	<i>32 cycles</i>	<i>43 cycles</i>
Domain-integrated $\nabla \cdot \mathbf{F}$ (GW)	<b>-0.04</b> / 0.12	<b>-0.03</b> / 0.14	<b>-0.03</b> / 0.14
Domain-averaged $\nabla \cdot \mathbf{F}$ ( $\text{mW m}^{-2}$ )	<b>-1.90</b> / 1.50	<b>-1.50</b> / 1.70	<b>-1.50</b> / 1.70

**Table 2.6:** Domain-integrated and domain-averaged baroclinic energy flux divergence in the 21, 32 and 43 tidal cycle runs model runs for the Whittard Canyon region (bold) and the whole domain.

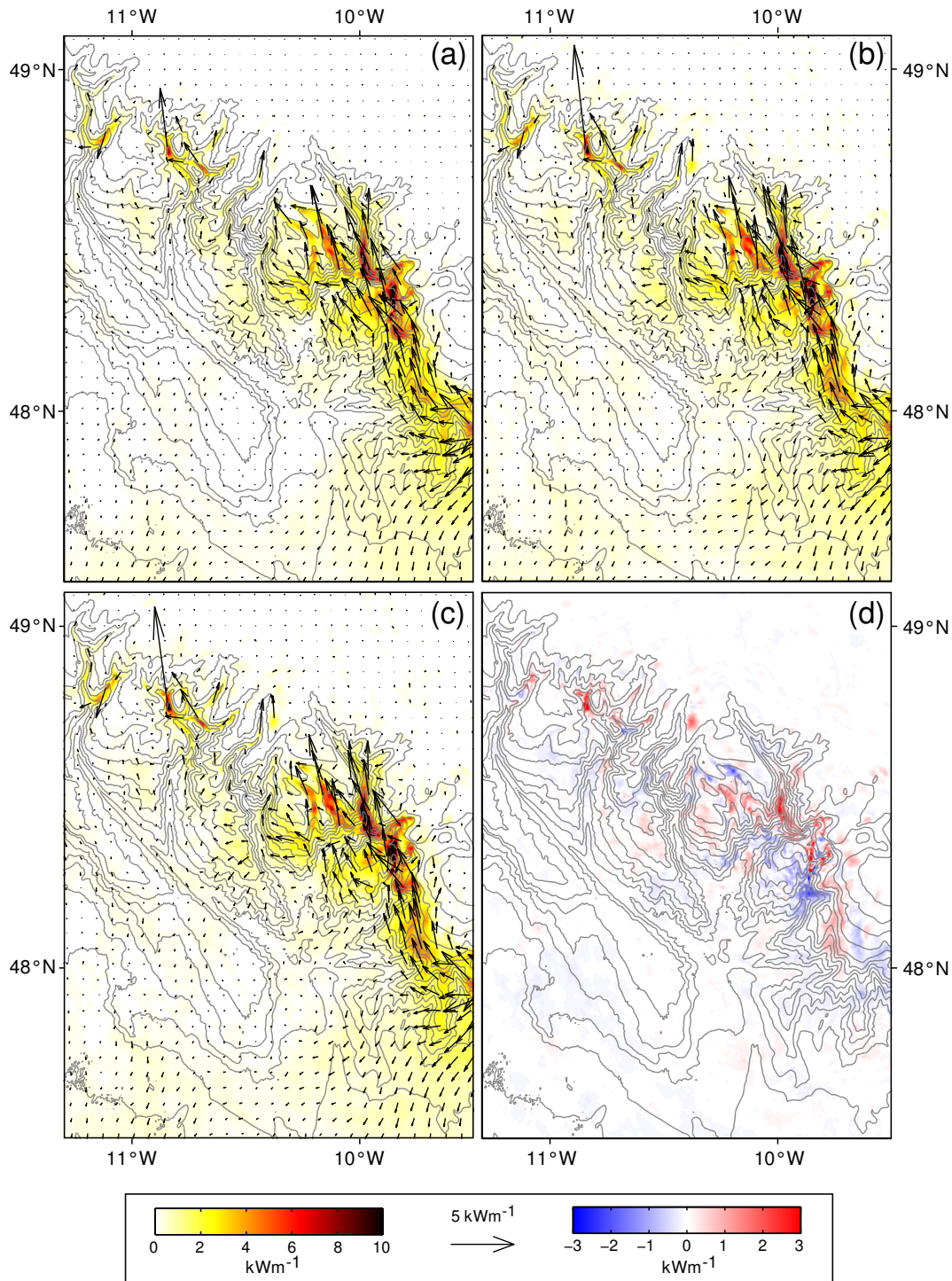


**Figure 2.15:** Depth-integrated baroclinic  $M_2$  energy flux in Whittard Canyon for model runs: (a) 21, (b) 32 and (c) 43 tidal cycles. Vectors are plotted every 10 model grid points ( $\approx 5$  km) in each direction. The underlying colour is the energy flux magnitude. Depth contours are plotted every 300 m. The difference in energy flux magnitude between 32 and 21 tidal cycles (32 cycles - 21 cycles) is shown in (d).

## 2.4 DISCUSSION AND CONCLUSIONS

Accurately representing seafloor bathymetry is a vital part of the modelling procedure to ensure that the internal tide field in the simulations is as close to reality as possible. A complete bathymetric dataset of the Whittard Canyon and surrounding area at the right resolution required for this work was not available, and therefore two data products were required to create one complete bathymetry input file. Combining GEBCO and INFOMAR data highlighted the difficulty of using products which may be geolocated differently, may have undergone different processing procedures and are of different resolutions. The effect of bathymetric resolution/smoothing on the internal wavefield is investigated in Chapter 6.

The correct domain size and run length are also important to diagnose. The run length chosen must also be long enough for the model to reach a steady state. Increasing the run length of the model does not seem to have a large impact on the calculated energetics of the internal tide within Whittard Canyon, with the model reaching steady state by 32 tidal cycles. This run length is therefore chosen as the ‘control’ simulation run length. The right domain size must be selected so that all the key generation sites are present, however too large a domain size is computationally expensive. The results of domain size sensitivity testing indicate that a domain that only includes Whittard Canyon does not include all of the generation sites that contribute to the internal tide field in the canyon itself. Shamrock Canyon is identified as a key generation site and a domain size including part the canyon is chosen as the ‘control’ domain size. Changing the domain size also has an interesting impact on the calculated energetics within the region; domain-integrated barotropic-to-baroclinic conversion and barotropic flux divergence show an increase with domain size, however when only the Whittard Canyon region is considered, both metrics are highest for the medium domain size, *wc02*. This result highlights the complexity of the internal tide in this region, which will be further investigated in Chapter 4.



# 3

## MODEL VALIDATION

### 3.1 INTRODUCTION

This chapter assesses the current models skill through comparison of model output with observational data from Whittard Canyon, namely data from a 2015 Seaglider deployment and also ADCP measurements taken in 2014. This chapter details the data used and any data processing carried out. Error (absolute and relative) estimates between the model and observations are calculated and the results are discussed.

### 3.2 INSTRUMENTATION

Two different sets of data are used to assess model skill: ADCP data and Seaglider data. The ADCP data consists of two time series collected during the Celtic Explorer cruise to Whittard Canyon (CE14009) over the period of the 10th-17th June 2014. Two different instruments with different frequencies were used, as detailed in Table 3.1, and were located within 2 km of one another, as shown in Figure 3.1. The Seaglider data<sup>1</sup> comprises of eight roughly 36-hour tide-resolving stations (with two repeat stations) collected during the RRS James Cook cruise to Whittard Canyon (JC125) over the period of the 15th August - 6th September using an iRobot Seaglider. Locations of

---

<sup>1</sup>Processed by Rob Hall.

the stations ('virtual moorings') are shown in Figure 3.1 and detailed in Table 3.2.

**Table 3.1:** Location, dates, depth and instrument used at each ADCP station

	<b>Location</b>	<b>Dates</b>	<b>Depth (m)</b>	<b>Instrument</b>	<b>First bin height (m)</b>
<i>adcp1</i>	48°42'16"N 10°33'31"W	11-17/06/14	1347	RDI 600 kHz 40 m range 2 m bins	4
<i>adcp2</i>	48°42'48"N 10°34'00"W	10-16/06/14	938	Nortek 1 MHz 14.5 m range 0.5 m bins	1

**Table 3.2:** Location of glider stations

<b>Glider station</b>	<b>Latitude</b>	<b>Longitude</b>
VM1	48°24.0'N	09°59.7'W
VM2	48°29.1'N	09°59.7'W
VM3a,b	48°34.5'N	09°56.4'W
VM4	48°38.4'N	10°01.5'W
VM5	48°42.3'N	10°05.4'W
VM6a,b	48°37.2'N	09°49.8'W
VM7	48°33.6'N	10°08.4'W
VM8	48°29.1'N	10°04.8'W

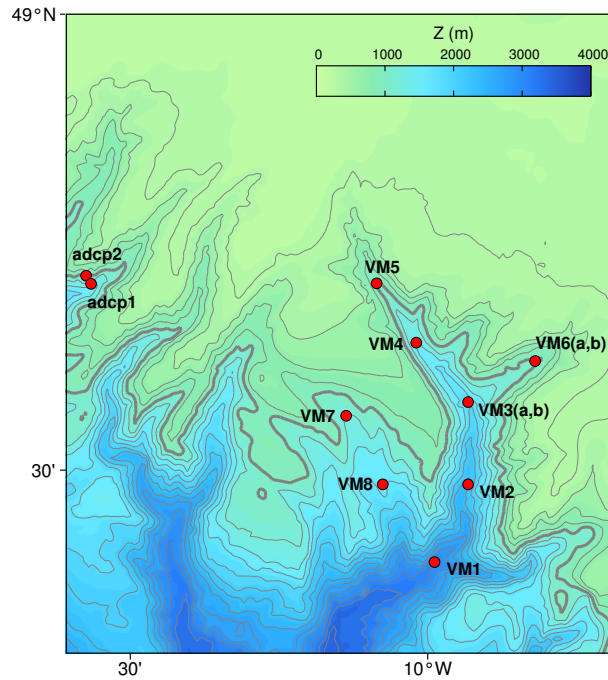


**Figure 3.1:** Locations of observations used for assessment of model skill. The 1000 m contour is marked in bold and contours are plotted every 200 m

### 3.3 METHODOLOGY

The model was run with an arbitrary start date (1st January 2012) and so must be synced to the time period covered by the observations. Comparison between the barotropic  $M_2$  surface elevation over the canyon in the current model, and the TPXO 7.2 inverse model of Egbert and Erofeeva (2002) for the same time period of the model run (Figure 3.2), show that the model output should broadly replicate the TPXO 7.2 output for the same time period. Hence, adjusting the model phase so that barotropic  $M_2$  surface elevation matches that of TPXO 7.2 data extracted over a different time period should sync the model to that new time period. Surface elevation phase does not vary much over the canyon (Figure 3.2), hence barotropic  $M_2$  surface elevation amplitude and phase from the middle of the domain ( $48^{\circ}30'N$   $10^{\circ}W$ ) were extracted from TPXO 7.2 for the two different periods when the ADCP and Seaglider data were obtained. This was then compared to the model surface elevation, also extracted from that location, and a phase correction (ADCP data, 0.16 rad; Seaglider data, 1.90 rad) applied to the model output to sync the model with observations.

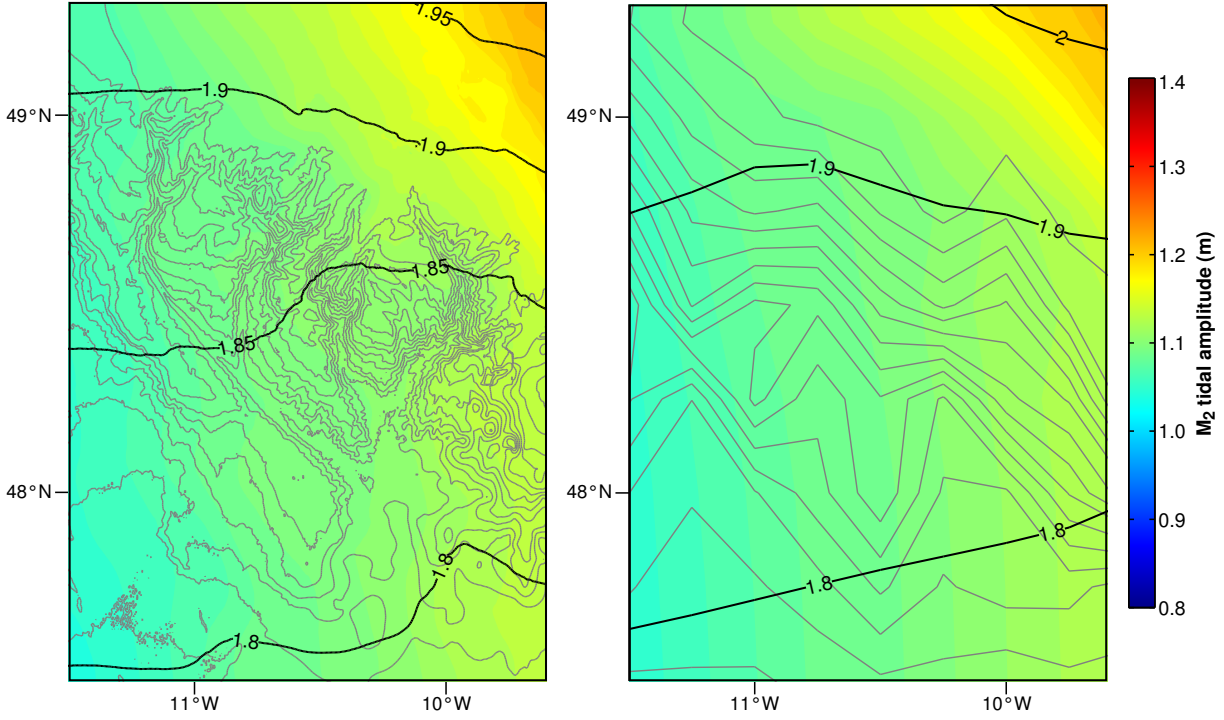


**Figure 3.2:**  $M_2$  barotropic surface elevation amplitude and phase (radians) for the current model (left) and TPXO 7.2 model (right). Bathymetric contours are plotted every 200 m using the different models respective bathymetries.

### 3.3.1 HARMONIC TIDAL ANALYSIS

Harmonic tidal analysis is used to calculate the amplitude and phases of the  $M_2$  tidal constituent in both the ADCP and Seaglider time series so that the data can be directly compared with the harmonic output from the model. The general form of harmonic tidal analysis for a time series  $x(t)$  is

$$x(t) = \bar{x} + \sum_{i=1}^N [A_i \cos(\omega_i t) + B_i \sin(\omega_i t)] + x_r(t) \quad (3.1)$$

where  $\bar{x}$  is the mean value of the time series,  $x_r(t)$  is the residual time series with zero time-mean,  $i$  is the tidal constituent and  $\omega_i$  is the angular frequency of the constituent (Thomson and Emery, 2014). Linear least-squares regression is used to find the constants  $\bar{x}$ ,  $A_i$  and  $B_i$  and hence the amplitude of the tidal constituent,  $x_{0i} = (A_i^2 + B_i^2)^{1/2}$ , and the phase lag,  $\phi_i = \tan^{-1}(B_i/A_i)$ , can be calculated. Equation

(3.1) can then be rewritten as,

$$x(t) = \bar{x} + \sum_{i=1}^N [x_{0i} \cos(\omega_i t - \phi_i)] + x_r(t) \quad (3.2)$$

The number of tidal constituents that can be resolved is dependant on the length ( $T$ ) of the time-series. Two constituents can be clearly separated if

$$|\Delta\omega| T/2\pi > 1 \quad (3.3)$$

where  $|\Delta\omega|$  is the difference in angular frequency between the two constituents. The respective lengths of both the Seaglider station time series ( $\sim 36$  hours) and ADCP time series ( $\sim 6$  days) are long enough so that the  $M_2$  and  $K_1$  constituents of the tide can be seperately resolved. However, both time series are too short to seperate the  $S_2$  and  $O_1$  constituents from the  $M_2$  and  $K_1$  constituents respectively. Only the  $M_2$  and  $K_1$  constituents (Table 3.3) are therefore included in the regression.

**Table 3.3:** Details of the tidal constituents fit by harmonic analysis to the observational data.

Constituent	Period (hours)	Angular frequency ( $\times 10^{-5}$ rad s $^{-1}$ )
Principal lunar semi-diurnal, $M_2$	12.42	14.05
Luni-solar diurnal, $K_1$	23.93	7.29

As the semi-diurnal  $M_2$  and diurnal  $S_2$  constituents of the equilibrium tide cannot be seperately resolved for both sets of observational data, it becomes necessary to apply an amplitude modulation factor to account for the position of each observation in the spring-neap cycle so that the observations can be compared directly with the model. The spring-neap cycle of the internal tide for both sets of data was removed by assuming it was phase-locked to the spring-neap cycle of the surface tide. Using the TPXO 7.2 inverse model, the spring-neap modulation of surface elevation,  $mod_{sn}$ , is approximated as

$$mod_{sn}(t) = 1 + \frac{A_{S_2}}{A_{M_2}} \cos\left(\frac{2\pi t}{T_{sn}} - \phi_{sn}\right) \quad (3.4)$$

where  $A_{S_2}$  and  $A_{M_2}$  are the respective amplitudes of the  $S_2$  and  $M_2$  tide,  $T_{sn}$  is the period of the spring-neap cycle (14.8 days) and  $\phi_{sn}$  is the phase of the spring-neap cycle (2.5 rad). The modulation was then used to create a correction factor ( $1/mod_{sn}$ )

which can be applied to a signal to remove the influence of the  $S_2$  tide.

### 3.3.2 ERROR ESTIMATES

To compare the model output and observations, we use a single error estimate calculated by combining amplitude and phase (Cummins and Oey, 1997; Carter et al., 2008),

$$E = \sqrt{\frac{1}{2}(A_o^2 + A_m^2) - A_o A_m \cos(\phi_o - \phi_m)} \quad (3.5)$$

where subscripts  $o$  and  $m$  indicate observed and modelled phases ( $\phi$ ) and amplitudes ( $A$ ). This error estimate is equivalent to the root mean square (rms) difference between the model and observations over one tidal cycle (Cummins and Oey, 1997) or the rms of the real and imaginary vector differences (Carter, 2010). The average rms error ( $\bar{E}$ ) can then be calculated using  $\bar{E} = n^{-1} \sum_n E$ , where  $n$  is the number of observations. As per Cummins and Oey (1997), the relative rms error is defined as

$$R_E = \frac{E}{A_o} \quad (3.6)$$

and hence the average relative rms error  $\bar{R}_E = n^{-1} \sum_n R_E$ .

To gain an understanding of the physical basis for different values of  $E$  and  $R_E$ , some idealised scenarios (as shown in Figure 3.3) are considered. If both the observed and modelled signals are identical in phase but differ in amplitude so that  $A_m = \frac{1}{2}A_o$  (Figure 3.3(a)),  $E$  can be shown to equal  $\frac{a_o}{2\sqrt{2}}$  and hence  $R_E = 35.4\%$ . For a scenario where the amplitude of both signals is identical but there is a phase shift ( $\phi_o - \phi_m$ ) of  $\pi$  (Figure 3.3(b)),  $E$  is equal to  $\sqrt{2}A_o$  and hence  $R_E = 141\%$ .

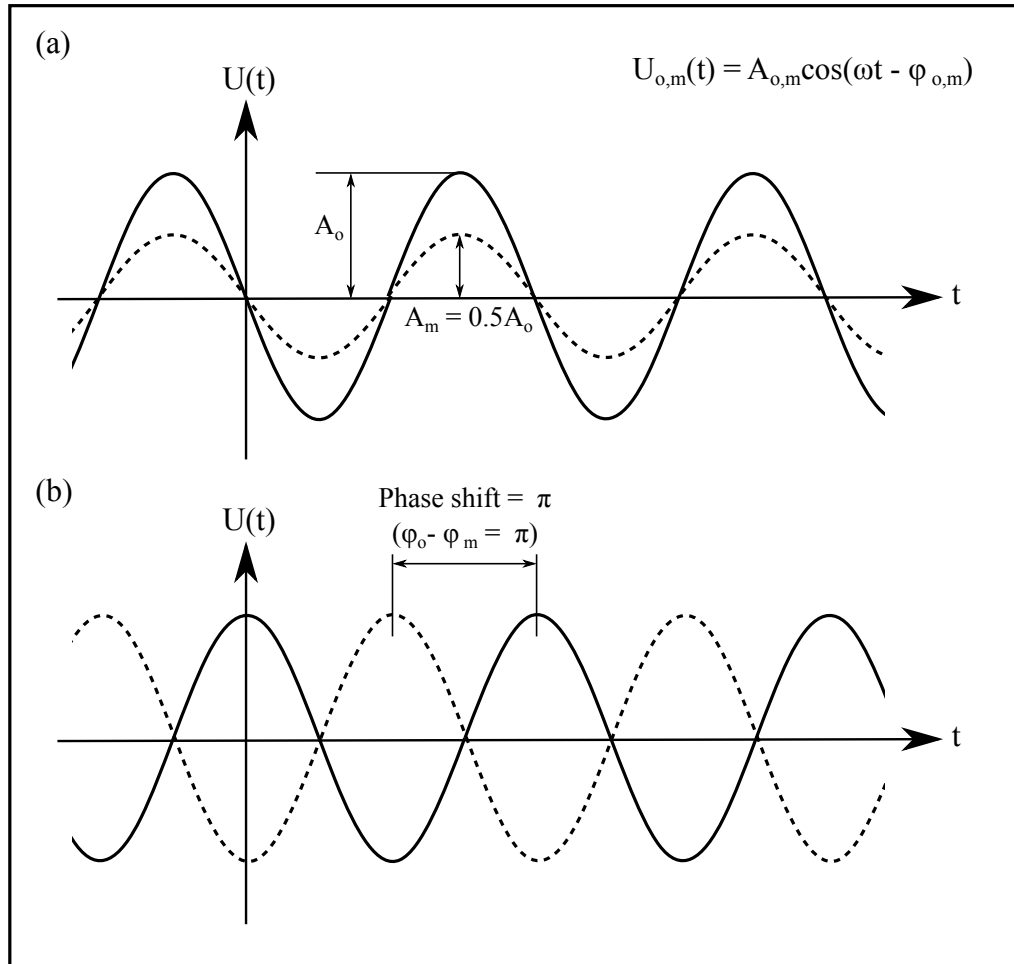


**Figure 3.3:** Schematic showing time-series of observed (solid line) and modelled (dashed line) signals where (a) the observed amplitude is twice the modelled amplitude and (b) where there is a phase shift of  $\pi$  between the observed and modelled signal.

## 3.4 MODEL AND OBSERVATIONAL DATA COMPARISON

### 3.4.1 ADCP DATA

The horizontal velocity time series for the two ADCPs detailed in Section 3.2 are shown in Figures 3.4 and 3.5. The meridional and zonal components of velocity from the instruments was rotated to along- and across canyon directions determined using the local orientation of the thalweg. Both time series start after neap tide, with spring tide occurring on day 164. A semi-diurnal signal is observed in both along- and across-canyon directions for *adcp2*, whilst *adcp1* has a less sinusoidal semi-diurnal signal in the along canyon direction only.

Along-canyon velocities recorded by *adcp1* show a strong semi-diurnal signal, however, this signal is absent in the across-canyon velocities (Figure 3.4). During springs, maximum along-canyon velocities are  $0.2 \text{ m s}^{-1}$  in a down canyon direction (southwest) whilst across-slope velocities are smaller,  $\sim 0.05 \text{ m s}^{-1}$ , and not oriented in a particular direction. In contrast, both along- and across-canyon velocities recorded by *adcp2* show a strong semi-diurnal signal (Figure 3.5). During springs, maximum along-canyon velocities are  $0.3 \text{ m s}^{-1}$ , and similar to *adcp1*, in a down canyon direction. Across-slope velocities are smaller ( $\sim 0.1 \text{ m s}^{-1}$ ) and in no prevailing direction.

To compare the ADCP data with the velocity amplitudes and phases of the bottom sigma layer in the model, vertical averages of observed velocity are calculated. The depth range covered by *adcp1* is larger (40 m) than the thickness of the bottom sigma level (25.9 m) in the model at the deployment location. Only the first 12 bins (26 m) are therefore vertically-averaged. As *adcp2* is higher in frequency, its range is only  $\sim 14.5 \text{ m}$ , and hence it doesn't cover the depth range of the bottom sigma layer within the model at that location (18.5 m). The velocity data are thus vertically-averaged over the entire dataset and are assumed to be representative of the entire sigma level. One matter of concern however is the discrepancy between ADCP depth (calculated from pressure records) and the model depth at the deployment location. The model depth for *adcp1* is 1294 m, significantly shallower than the deployment depth of 1346 m. The difference for *adcp2* is not as serious; model depth is 926 m whilst the deployment depth is 938 m. This raises questions about how well the model bathymetry actually replicates the actual structure of the canyon, due to small scale bathymetry not being resolved.

An  $M_2$  harmonic fit was made to the vertically-averaged velocities over the period  $\pm 18$  hours either side of the spring tide (36 hours) and a spring-neap correction factor ( $1/\text{mod}_{sn}$ , Section 3.3.1), applied (0.75 at spring tide). As shown in Figure 3.4, the  $M_2$  fit to the along- and across-canyon velocities for *adcp1* are out of phase with the model by approximately  $\pi/2$ , and the along-canyon velocity amplitudes differ by up to 44%. The harmonic fit to the across-canyon velocity is not expected to be very accurate however as the signal is quite a low amplitude and incoherent. The  $M_2$  fit to the *adcp2* data compares more favourably with the model output (Figure 3.5): with only a small phase difference and similar amplitudes to the model. The phase

between the along- and across-canyon observed velocities suggests a rectilinear tide that is not orientated along or across canyon.

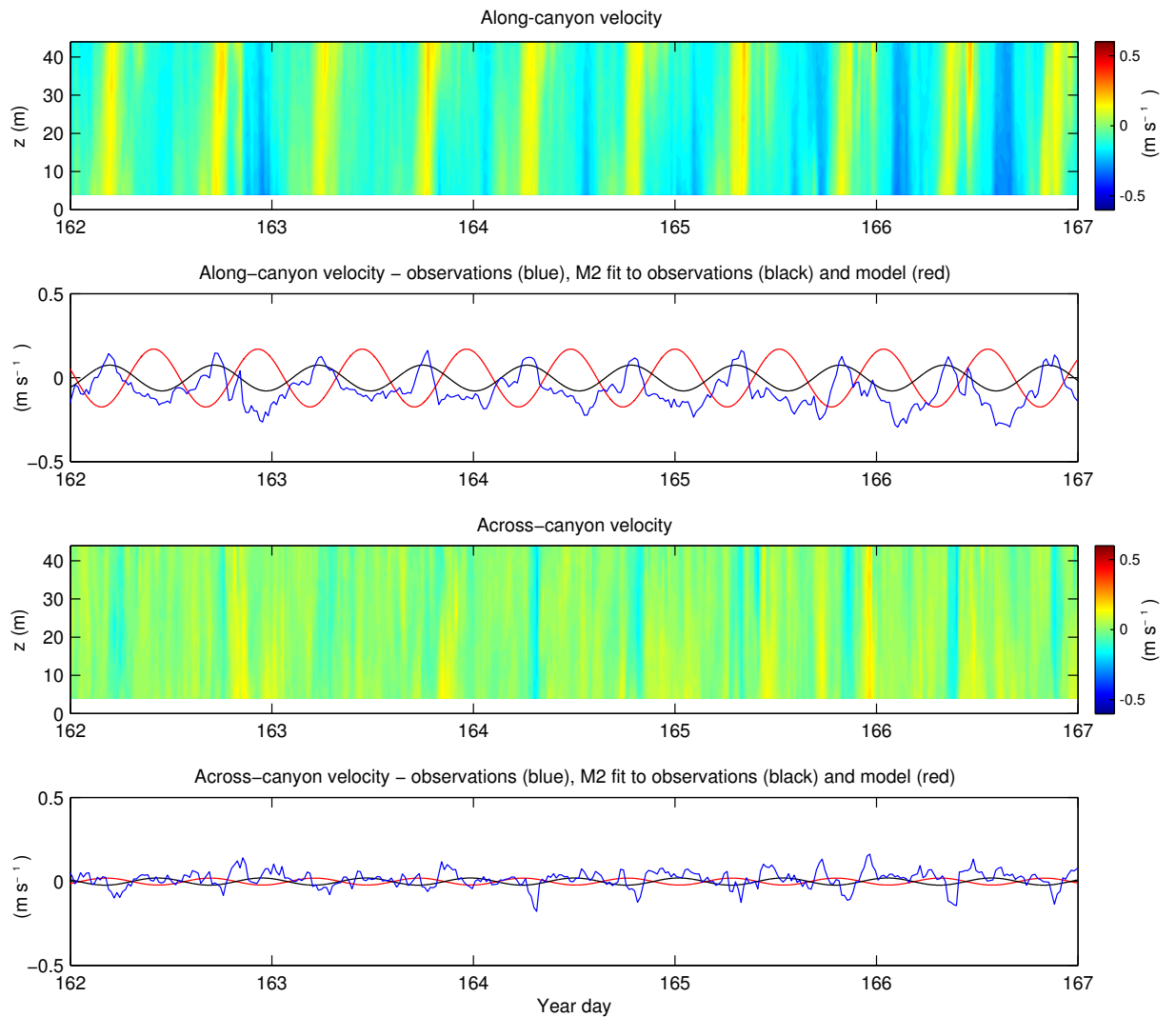


**Figure 3.4:** *adcp1* time-series of along- and across-canyon velocities and depth-averaged along- and across-canyon velocities (blue lines).  $M_2$  harmonic fits to both the observations (black), with a spring-neap correction applied, and model output (red) at the *adcp1* location are also shown.

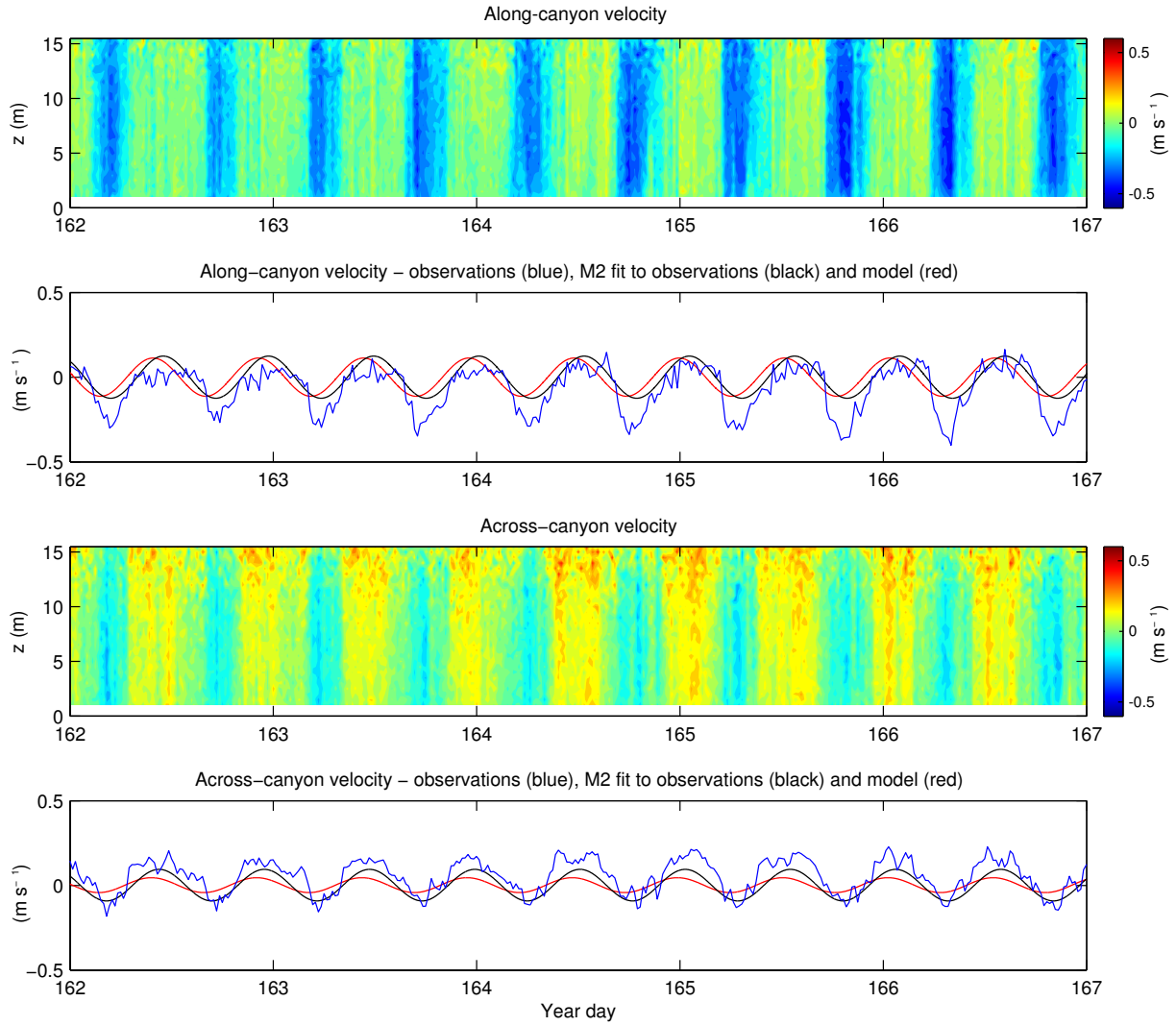


**Figure 3.5:** *adcp2* time-series of along- and across-canyon velocities and depth-averaged along- and across-canyon velocities (blue lines).  $M_2$  harmonic fits to both the observations (black), with a spring-neap correction applied, and model output (red) at the *adcp2* location are also shown.

### ERROR ESTIMATES

Absolute and relative rms error estimates between the observational data and model are calculated using the method detailed in Section 3.3.2 and presented in Table 3.4 alongside the model and ADCP  $M_2$  amplitudes and phases. The relative rms error for *adcp1* is much larger than that of *adcp2* for both the along- and across-canyon velocities, reaching a maximum of 233.3% in the along-canyon direction. The value of  $R_E$  for both the along- and across-canyon velocity components in *adcp2* are very similar (40.5% and 43.6%, respectively), whilst for *adcp1* they are quite different

(223.3% and 139.4%, respectively). Why *adcp1* is so different to the model, yet *adcp2* is so similar, is not fully clear and is discussed further in Section 3.5.

**Table 3.4:** Comparison of  $M_2$  velocity amplitudes and phases between the model and ADCPs.

Station	Orientation	Modelled		Observed		$E$ $\text{ms}^{-1}$	$R_E$
		A ( $\text{ms}^{-1}$ )	P ( $^\circ$ )	A ( $\text{ms}^{-1}$ )	P ( $^\circ$ )		
<i>adcp1</i>	Along-canyon	0.1724	-1.0651	0.0768	2.5796	0.1715	223.3%
	Across-canyon	0.0207	2.3570	0.0213	-0.8324	0.0297	139.4%
<i>adcp2</i>	Along-canyon	0.1129	-1.1437	0.1244	-0.5413	0.0504	40.5%
	Across-canyon	0.0438	-1.2346	0.0931	-0.7716	0.0406	43.6%

### 3.4.2 SEAGLIDER DATA

An iRobot Seaglider was deployed over Whittard Canyon for 22 days, primarily over Limb 4 (Figure 2.8), and occupied 8 stations with two stations (VM3a and VM3b) occupied twice (roughly at spring and neap tide). Each station occupation was at least 35 hours during which time the glider made 13-20 dives to 1000 m or the seabed (whichever was shallower) <sup>2</sup>. Profiles of temperature and salinity were measured during both the glider's ascent and descent and processed separately yielding 26-40 profiles over 35-42 hours for each station occupation. This is adequate to separately resolve the  $M_2$  and  $K_1$  internal tides (Nash et al., 2005). Almost all the profiles were within 2.5 km of the target locations, based on GPS fixes when the glider was at the surface. Subsurface sample locations were approximated by linearly interpolating latitude and longitude onto sample time. The temperature and salinity profiles were averaged in 5-m depth-bins and potential density profiles calculated using the TEOS-10 equation of state (McDougall and Barker, 2011).

For each station occupation, the time-average potential density profile and N2 profile were calculated then vertical isopycnal displacement calculated from the density perturbations. A  $M_2$  and  $K_1$  harmonic analysis was applied to isopycnal displacement at each depth level, yielding profiles of  $M_2$  and  $K_1$  displacement amplitudes and phases <sup>3</sup>.  $K_1$  displacement amplitude was small during all station

<sup>2</sup>Only 9 dives over 22 hours at VM8.

<sup>3</sup>Only a  $M_2$  harmonic analysis for VM5 and VM.

occupations so only the  $M_2$  internal tide is considered here.

The spring-neap cycle of the internal tide was removed using a spring-neap correction factor ( $1/mod_{sn}$ , Section 3.3.1) calculated from the spring-neap modulation interpolated onto the time of the average time of each station occupation. The resulting correction factor for each station occupation (0.75 to 1.47) was applied to observed vertical isopycnal displacement amplitude in order to remove the influence of the  $S_2$  tide. Vertical isopycnal displacement amplitude was extracted from the model at each station location, after a  $+0.005^\circ$  shift was applied to model latitudes and longitudes to account for the offset between model bathymetry and the bathymetry measured by the altimeter on the Seaglider. The resulting profiles are shown in (Figures 3.7-3.7).

There is a reasonably good fit between observed and modelled isopycnal displacement, however, the model generally underestimates displacement amplitude. The relationship between observed and modelled phases however is not so clear; some profiles are almost identical in phase (e.g. VM2 and VM3b), some show a consistent phase offset (e.g. VM4 and VM5) and some have very different structures (e.g. VM1).

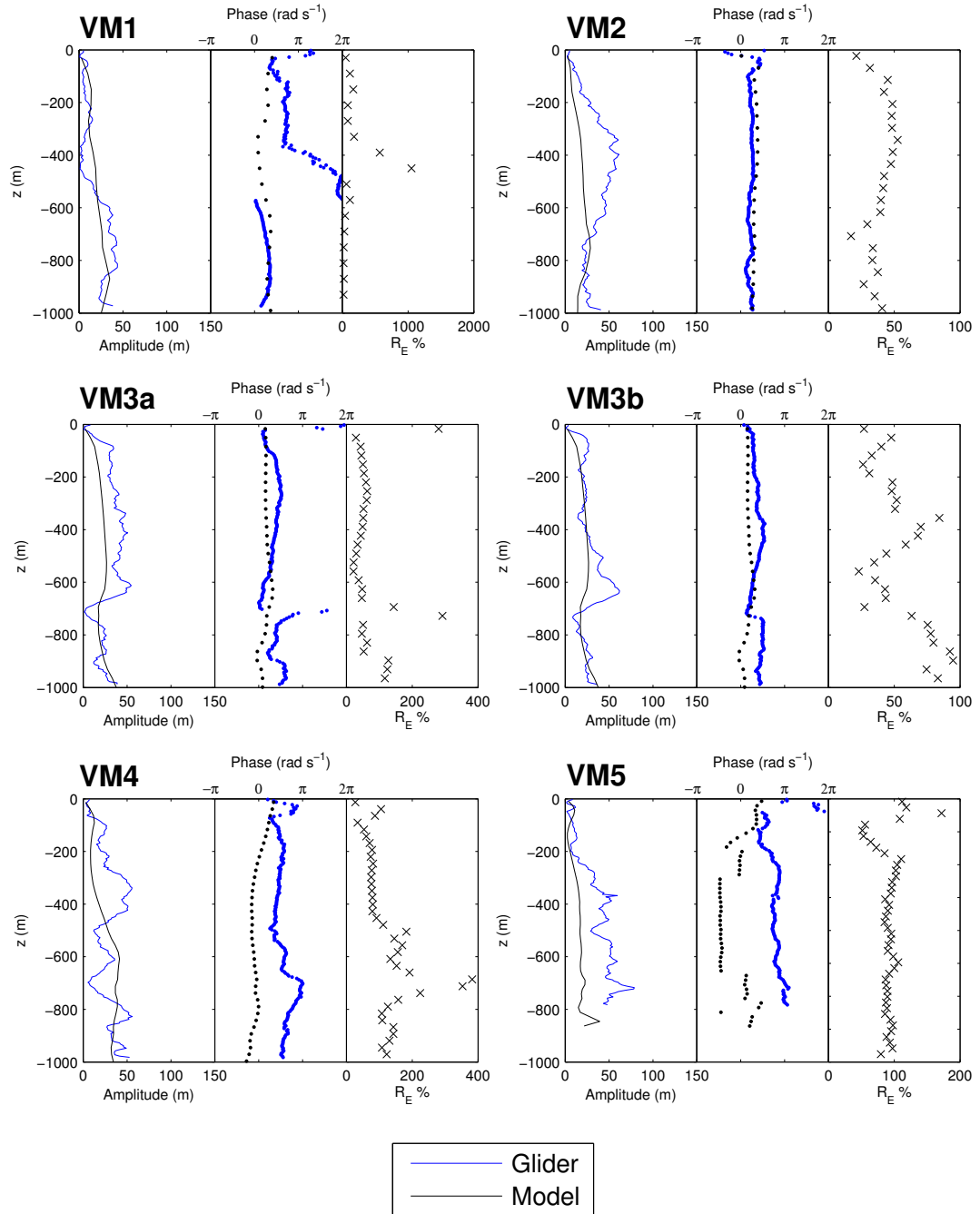


**Figure 3.6:** Comparison between  $M_2$  isopycnal displacement amplitude (left panel) and phase (centre panel) for glider stations VM1, VM2, VM3a, VM3b, VM4 and VM5 (blue) and the current model (black). The depth structure of relative rms error,  $R_E$ , is shown in the right panel.

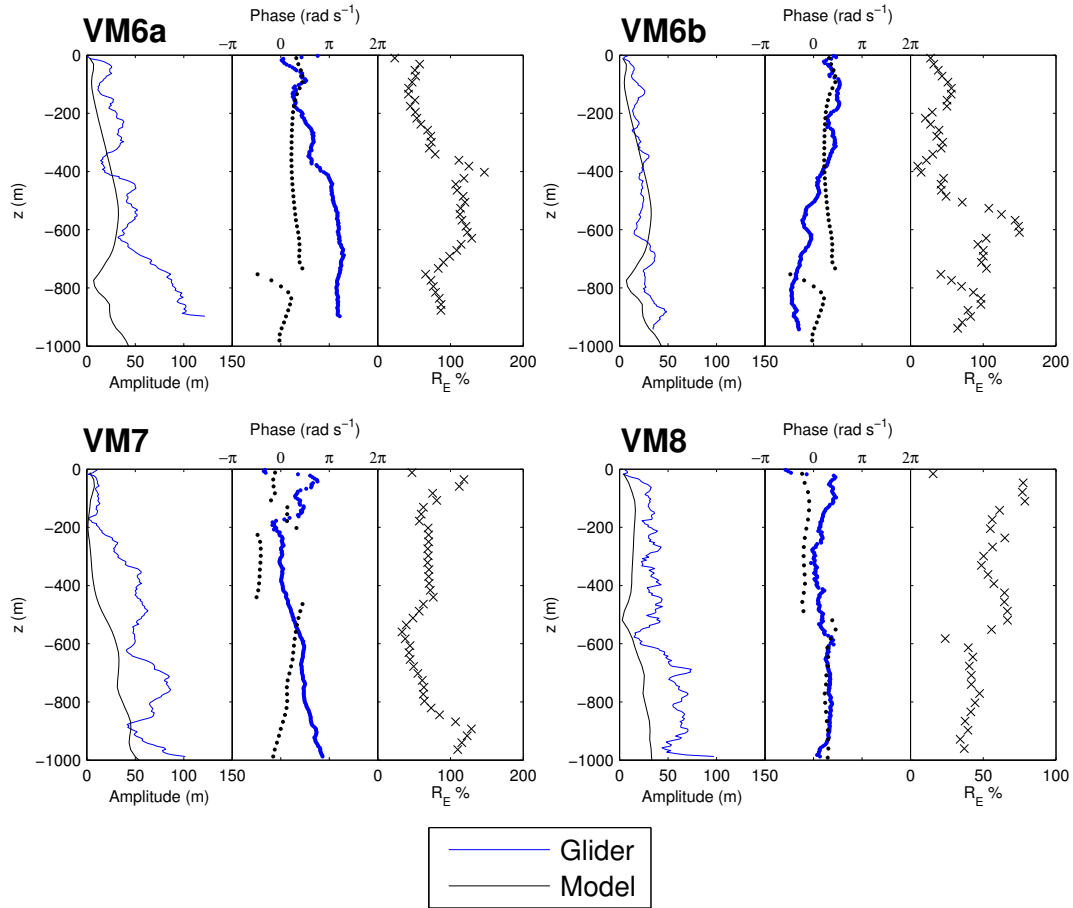


**Figure 3.7:** Comparison between  $M_2$  isopycnal displacement amplitude (left panel) and phase (centre panel) for glider stations VM6, VM7, VM8a and VM8b (blue) and the current model (black). The depth structure of relative rms error,  $R_E$ , is shown in the right panel.

### 3.4.3 ERROR ESTIMATES

The depth-averaged absolute and relative rms error estimates between the observational data and model are calculated using the method detailed in Section 3.3.2 and presented in Table 3.5. The depth-averaged relative rms errors ranges from 38.7% to 165.6% with an average value of 82.0%. The depth structure of  $R_E$  is shown in the righthand panel of Figures 3.6-3.7 and highlights how variable the rms error is with depth. No consistent relationship between error and depth is found.

**Table 3.5:** Average RMS error ( $\bar{E}$ ) and average relative RMS error ( $\bar{R}_E$ ) between the model and Seaglider data.

	$\bar{E}$ (m)	$\bar{R}_E$
<b>VM1</b>	10.5	165.6 %
<b>VM2</b>	13.7	38.7 %
<b>VM3a</b>	16.0	73.8 %
<b>VM3b</b>	13.7	54.4 %
<b>VM4</b>	32.0	122.6 %
<b>VM5</b>	31.1	92.6 %
<b>VM6a</b>	38.9	85.3 %
<b>VM6b</b>	16.5	65.1 %
<b>VM7</b>	31.7	70.8 %
<b>VM8</b>	20.5	51.1 %

### 3.5 DISCUSSION AND CONCLUSIONS

The calculated error between the model output and observational data at first glance appears high, however previous work in Monterey Canyon by Carter (2010) using POM found similar RMS errors, ranging between 30% - 209%. The interpretation of the model-data comparison presented here should take into consideration that all the validation locations used are within topographically complex regions. Vertical wall and rocky overhangs are key geomorphological features within Whittard Canyon (Huvenne et al., 2011; Johnson et al., 2013), however, the resolution of the model used here (500 m) limits how much of this structure can actually be resolved. Furthermore, the morphology of the canyon is likely to be evolving constantly due to erosional and depositional processes (e.g. Amaro et al. (2015)). The bathymetry used within the model is therefore an approximation of the actual canyon morphology, and hence the model is not expected to resolve all the features of the internal tide within the canyon that observations may record. For example, the complex structure in isopycnal displacement phase observed by the Seaglider (Figures 3.6-3.7), but not replicated in the model output, is likely due to the inability of the model to resolve higher modes, with a limit set by bathymetric resolution (Zilberman et al., 2009).

The discrepancy between model bathymetry and observations exists for both the ADCP and Seaglider datasets. ADCP depths, calculated from ROV pressure records, and the model depth at deployment location vary for both *adcp1* and *adcp2*, with differences of 52 m and 12 m respectively. This could be accounted for by the model not resolving the bathymetry sufficiently. Altimeter records for the Seaglider data indicated that recorded depths at a given location were shallower than those in the model bathymetry. When compared with other available bathymetric datasets it was determined that the model bathymetry was offset, and hence a latitude and longitude shift applied to correct for this. When the original model bathymetry was produced (Section 2.2.2), shifts were applied to the GEBCO portion of data to correct the offset between it and the higher resolution INFOMAR data, with the assumption that the INFOMAR data was correctly geolocated. Although some of this manipulation explains the observed offset in the Seaglider dataset, it doesn't explain all of it, raising questions about the accuracy of geolocation within widely available data products.

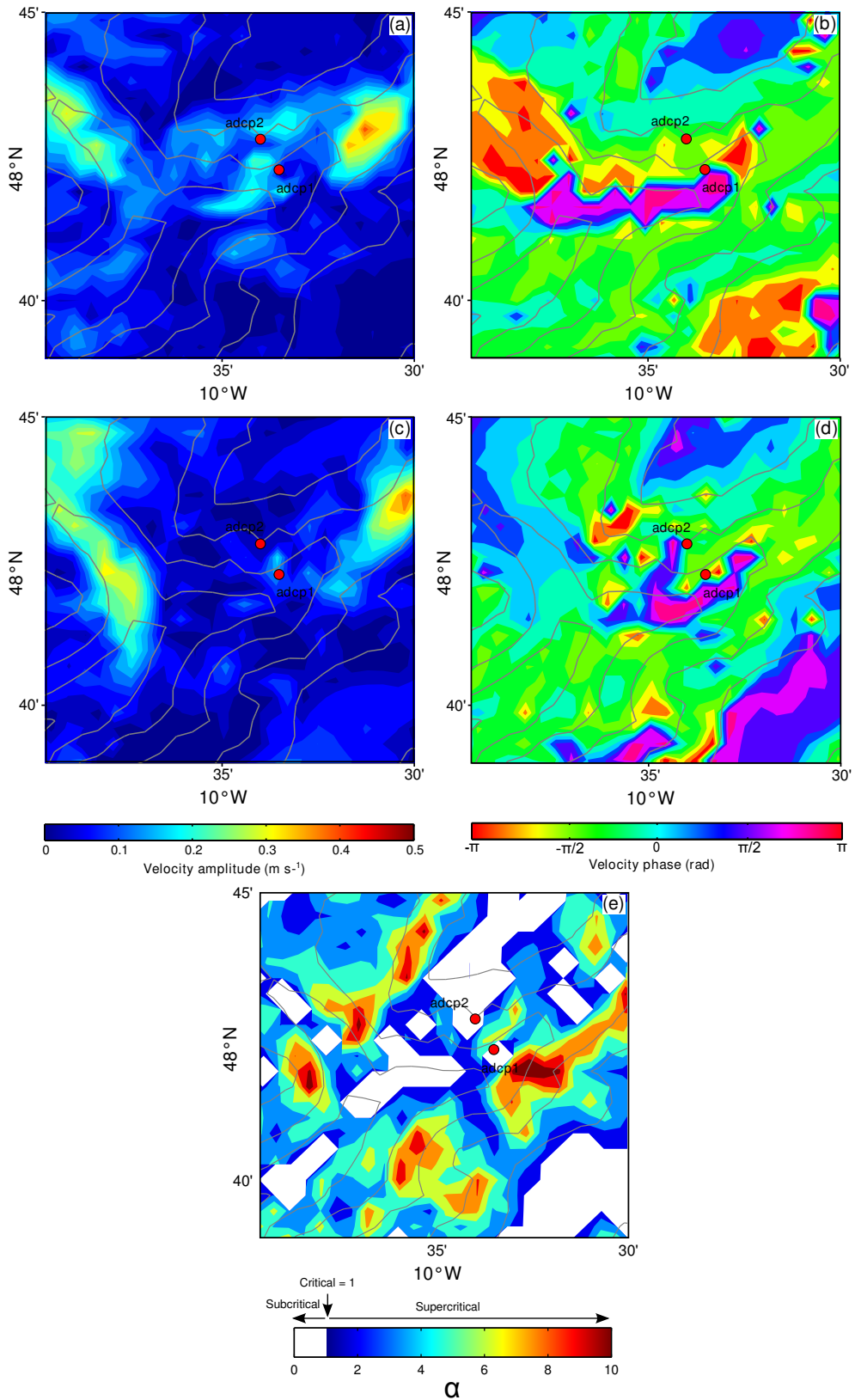


**Figure 3.8:** (a) Amplitude and (b) phase of modelled near-bottom total (barotropic and baroclinic) zonal  $M_2$  velocity in the region surrounding *adcp1* and *adcp2*. (c) Amplitude and (d) Phase of modelled near-bottom total meridional  $M_2$  velocity in the region surrounding *adcp1* and *adcp2*. (e) Maps of criticality ( $\alpha$ ) for the region surrounding *adcp1* and *adcp2*. Contours are plotted every 300 m.

A significant difference was observed between not only the calculated errors, but also the raw recorded velocities at *adcp1* and *adcp2*, despite their geographic proximity. Figure 3.8 shows that velocity phase, and to a lesser extent amplitude, in the model in the region of the ADCP deployments is highly variable. This may explain some of the differences observed between the two measurements and the resulting errors, however, the quality of the *adcp1* is still suspect due to its incoherent nature. An in-depth analysis of the dataset to assess quality, however, is beyond the scope of this project. The variability in phase within the model also has implications for error calculations with the Seaglider data too. The data were distributed in a 5 km watch circle and compared with the model output at the centre of the watch circle. Given that there is variability in the model in phase over that length scale, the errors calculated are therefore reasonable.

The assumption that the spring-neap cycle of the surface tide and the internal tide are phase-locked was used to sync model output with the observations, however, this assumes local internal tide generation. As Gerkema (2002) states, the phase of the baroclinic spring-neap cycle is dependant on the phase difference between the  $M_2$  and  $S_2$  internal tide, and hence will not always be synchronous with the barotropic spring-neap cycle. Evidence for phase-locking is provided by the Seaglider observations at VM3a and VM3b (taken at different parts of the spring-neap cycle), which after modulation, display similar amplitudes.

In conclusion, the errors calculated between the model and observations are reasonable when the shortcomings of the model and observations are considered. Bathymetric resolution is a key determinant of model skill, however increasing bathymetric resolution to sufficiently resolve the complex bathymetry encountered in Whittard Canyon is too computationally expensive and still would not be able to resolve features such as overhangs. Given the length scales of the  $M_2$  internal tide, it may not be necessary to have such high bathymetric resolution to be able to resolve the key features of the internal tide (further investigated in Chapter 5), however, finer scale features of interest to biologists and geologists (Chapter 6) will not be resolved.

# 4

## INTERNAL TIDES IN WHITTARD CANYON

### 4.1 INTRODUCTION

This chapter investigates the dynamics of the internal tide within Whittard Canyon using the control model setup as defined in Chapter 2 (32 tidal cycles, *summer* stratification and the *medium* domain size). The internal tide within Whittard Canyon has been postulated to have a potentially huge impact on the biology within the canyon (Robert et al., 2015) and also play a role in the generation of nepheloid layers (Wilson et al., 2015b). However, although internal tides around the Celtic Sea shelf edge region have been well studied, information about internal tides within Whittard Canyon are limited. Internal tides within sinuous submarine canyons have been modelled using POM previously (e.g. Hall and Carter, 2011; Gregg et al., 2011) but to our knowledge, no previous attempt at modelling the internal tide within a branched canyon has been made before. This study therefore provides a view on a different type of canyon than is often studied.

In this chapter, the key generation sites for the internal tide within the canyon are identified, and the three-dimensional structure of the internal tide described. A crude energy budget is calculated and the propagation of the internal tide on-shelf investigated. A more complicated canyon limb naming scheme than Figure 2.8 is used in this chapter, and is shown in Figure 4.1.

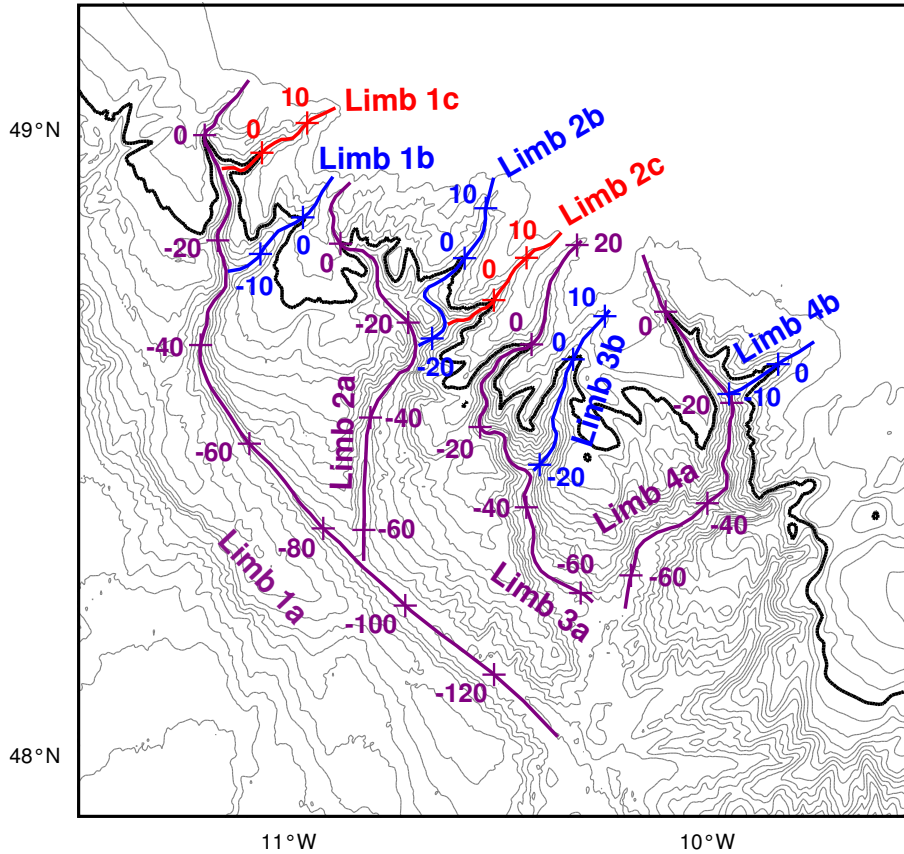


**Figure 4.1:** Location of limbs and along-thalweg sections used. Distance along each thalweg, referenced to the 1000-m isobath (positive shallower than 1000 m, negative deeper than 1000 m) is marked in either 20-km or 10-km intervals.

In Section 4.2 the main generation sites for the internal tide within Whittard Canyon are identified. In Section 4.3 the spatial structure and variability of the internal tide within Whittard Canyon are discussed and an initial energy budget calculated. In Section 4.5 the internal tide propagation on-shelf is examined.

## 4.2 INTERNAL TIDE GENERATION

The sloping topography of Whittard Canyon and its surrounding area provide many potential internal tide generation sites through the scattering of the barotropic tide (Bell, 1975; Baines, 1982). As shown by Rainville et al. (2010), internal tides originating from different sources lead to complex patterns of constructive and destructive interference, with beams of depth-integrated energy flux appearing and disappearing, making it difficult to interpret internal tide generation. However, realistic interpretation about internal tide generation can be made by comparing depth-integrated baroclinic  $M_2$  fluxes (Figure 4.2 (a)) with barotropic-to-baroclinic  $M_2$  energy conversion (Figure 4.2 (b)) (e.g. Monterey Canyon (Hall and Carter, 2011)).

### 4.2.1 REMOTE GENERATION

Much of the internal tide energy entering Whittard Canyon appears to originate from the region to the east of the canyon, where the depth-integrated energy fluxes are consistent with regions of high ( $>0.2 \text{ W m}^{-2}$ ) barotropic-to-baroclinic conversion. Internal tide generation to the east of the canyon can be roughly divided into two areas: the upper limbs of Shamrock Canyon to the east of Brenot Spur, and also the western flank of Brenot Spur, which is incised by the Explorer and Dangeard Canyons (as described by Stewart et al. (2014)). Baroclinic energy appears to radiate from these major generation sites: a strong and narrow beam of baroclinic energy propagates northwest around Brenot Spur and onto the shelf via Limb 4a, whilst a second strong, but wider, beam of baroclinic energy propagates southwest from Shamrock Canyon onto the abyssal plain. As discussed in Section 2.3.1, the strength of the northwest propagating beam appears to be due to the interaction between generation within the canyon, generation to the west of Brenot Spur and at Shamrock Canyon. When a domain size excluding the Shamrock Canyon region is considered, the pattern of depth-integrated baroclinic energy flux is very different, with the strong, northwest propagating beam being largely absent (Figure 2.11 (a)).

The northwest propagating beam appears to be constrained by the morphology of Limb 4a: large depth-integrated baroclinic energy fluxes ( $>8 \text{ kW m}^{-1}$ ) are directed northwest up-canyon along its upper reaches (-30 km along the thalweg referenced

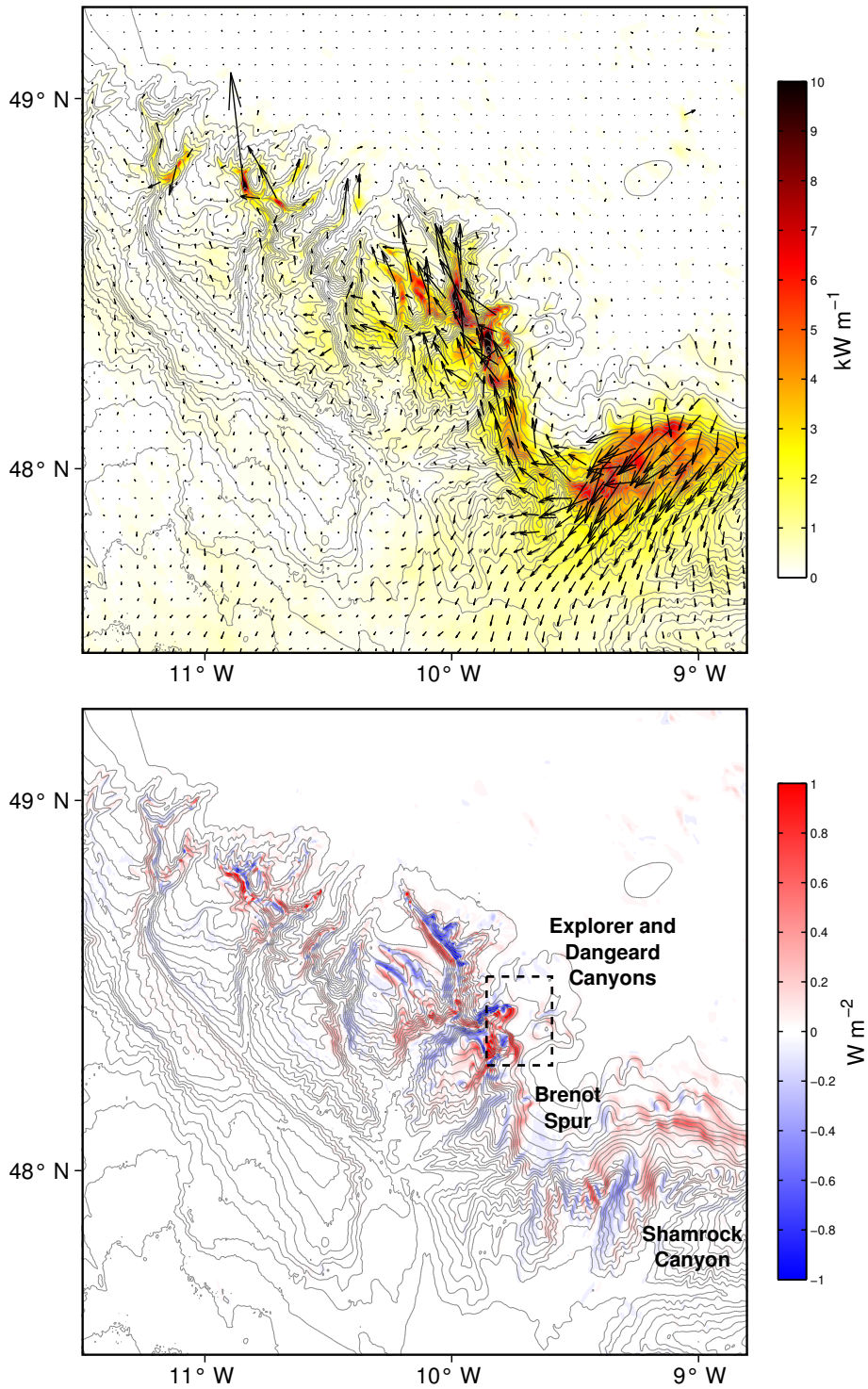


**Figure 4.2:** (a) Depth-integrated baroclinic  $M_2$  energy flux in the Whittard Canyon region. Vectors are plotted every 40 model grid points ( $\approx 20$  km) in each direction. The underlying colour is the energy flux magnitude. (b) Barotropic-to-baroclinic  $M_2$  energy conversion. Positive values indicate sources of baroclinic energy. Depth contours are plotted every 200 m.

to the 1000-m isobath, Figure 4.1) and the beam is greatly reduced in strength by the corrugated western flank of Limb 4a. Values of depth-integrated baroclinic energy throughout the rest of the canyon are much lower in comparison to those in Limb 4a, indicating either a lesser, or completely absent, influence on the canyon from the remote generation sites to the east.

#### 4.2.2 LOCAL GENERATION

Internal tide generation also occurs within the canyon and is identifiable by regions of positive barotropic-to-baroclinic conversion corresponding to both up and down-canyon depth-integrated baroclinic energy fluxes e.g. the western flank of Limb 4a along its lower reaches, Limbs 2b and 2c, the upper reaches of Limb 2a, the western flank of Limb 3a and Limb 1b. In the upper reaches of Limb 4a and Limb 2a, regions of strongly positive ( $>0.8 \text{ W m}^{-2}$ ) and negative ( $<-0.8 \text{ W m}^{-2}$ ) conversion occur adjacent to one another, implying that local internal tide generation is in part balanced by baroclinic energy loss to the barotropic tide. Negative energy conversion originates from the phase difference between remote and locally generated internal tides (Zilberman et al., 2009; Kelly and Nash, 2010) indicating that there are multiple generation sites. This ‘twinning’ of positive and negative energy conversion also occurs in Limb 1a and Limb 3a, but the magnitude of the energy conversion involved is much lower ( $<-0.4 \text{ W m}^{-2}$ ,  $>0.4 \text{ W m}^{-2}$ ). The spatial distribution of energy conversion is fairly consistent throughout the canyon, with positive conversion tending to occur on the western flanks of the canyon limbs and negative conversion tending to occur on the eastern flanks.

## 4.3 INTERNAL TIDE PROPOGATION THROUGH WHITTARD CANYON

In the upper reaches of Whittard canyon, depth-integrated baroclinic  $M_2$  energy fluxes are generally up-canyon, as expected by topographic focusing of an offshore generated internal tide. However, there are clear examples of down-canyon values too e.g. Limb 1b.

### 4.3.1 BAROCLINIC TIDAL CURRENTS

Near-bottom horizontal baroclinic  $M_2$  tidal current ellipses along the canyon thalwegs are shown in Figure 4.3. In the lower reaches of all the main limbs, current velocities are low ( $<0.1 \text{ m s}^{-1}$ ) and the tidal ellipses fairly circular. Moving up-canyon the semimajor axes of the ellipses becomes increasingly orientated along the canyon axis and highly rectilinear (i.e. the semiminor axis is insignificant compared to the semimajor axis) in the upper reaches of all the main limbs. The correlation between semimajor axis orientation and the thalweg suggests topographic steering of the internal tide. In the upper limbs of the canyon, the semimajor axes of the near-bottom tidal ellipses increases, with values up to  $0.4 \text{ m s}^{-1}$  being reached.

Observations of bottom currents within the canyon are limited, however those that exist appear to be in agreement with the modelled currents. The deepest measurements ( $>4000 \text{ m}$ ) have recorded bottom currents displaying weak semi-diurnal frequencies and velocities  $\leq 10 \text{ cm s}^{-1}$  (Van Weering et al., 2000; Amaro et al., 2015). Measurements in shallower regions indicate increasingly energetic bottom currents with reducing depth e.g.  $0.16 \text{ m s}^{-1}$  recorded by Reid and Hamilton (1990) (3752 m) and maximum speeds greater than  $0.24\text{-}0.40 \text{ m s}^{-1}$  measured by Duros et al. (2011) (1000 m).

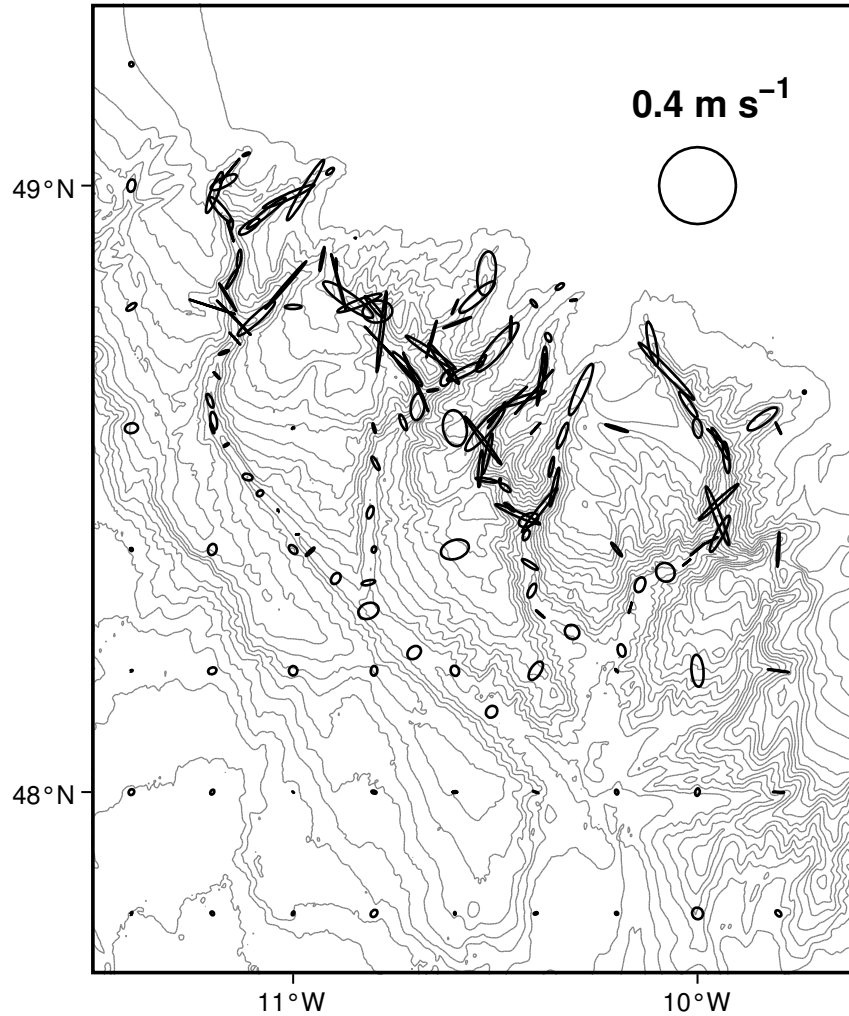


**Figure 4.3:** Modelled near-bottom horizontal baroclinic  $M_2$  tidal current ellipses. Current ellipses shallower than 300 m are omitted for clarity. Depth contours are plotted every 200 m.

### 4.3.2 KINETIC AND POTENTIAL ENERGY

Baroclinic horizontal kinetic energy (HKE) density is calculated as per the method in Section 2.2.3. Depth-integrated HKE within the canyon is maximum ( $\sim 10 \text{ kJ m}^{-2}$ ) in Limbs 4a, 2a and 1b (Figure 4.4 (a)) and closely mirrors the spatial distribution of depth-integrated baroclinic energy flux as shown in Figure 4.2 (a). HKE is also elevated in the region to the east of Brenot Spur, identified as a key generation site.

Available potential energy (APE) density is calculated as per the method in Section 2.2.3. Depth-integrated APE is intensified over a larger proportion of the canyon than HKE, reaching a maximum ( $> 12 \text{ kJ m}^{-2}$ ) in Limbs 4a, 2a, 2b and 1b and also the region to the east of Brenot Spur (Figure 4.4 (b)). The background value of

depth-integrated APE across the whole domain, however, is reduced in comparison to depth-integrated HKE; depth-integrated HKE is elevated ( $\sim 3 \text{ kJ m}^{-2}$ ) over much of the shelf slope in between canyon limbs, whereas depth-integrated APE is not.

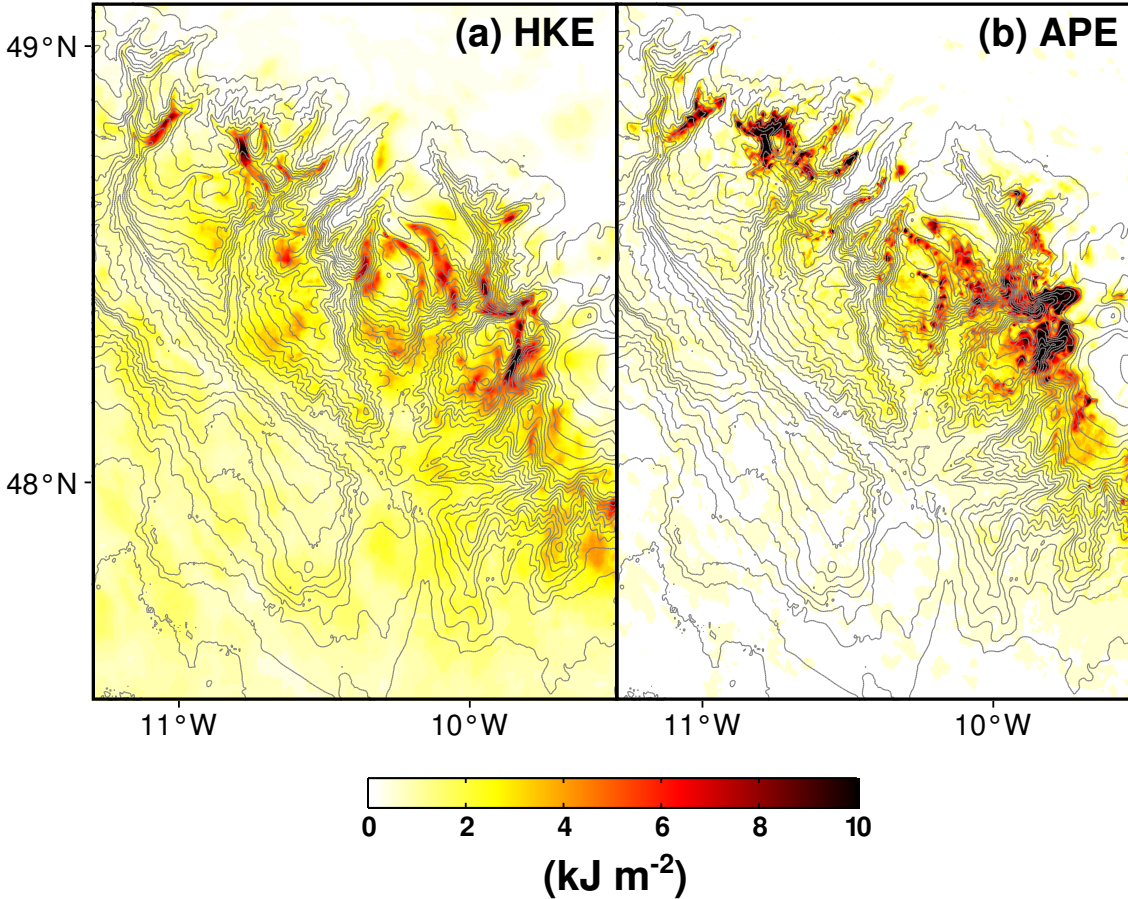


**Figure 4.4:** (a) Depth-integrated baroclinic  $M_2$  HKE in Whittard Canyon. (b) Depth-integrated  $M_2$  APE. Depth contours are plotted every 200 m.

The ratio HKE/APE is calculated for the upper reaches of Whittard Canyon and averaged within the regions outlined in Figure 4.15. The calculated values (Table 4.1) are significantly smaller than the theoretical value for a freely propagating  $M_2$  internal tide in this region (3.99, Section 2.2.3). This discrepancy has previously been seen in other canyons e.g. Monterey Canyon, and it was hypothesised by Petrucio et al. (1998) that excess APE was a consequence of across-canyon motion being constrained by the canyon topography. The morphology of Whittard Canyon could potentially have a similar effect, however, HKE/APE throughout the upper reaches is  $< 1$  (APE  $>$  HKE), inconsistent with free hydrostatic internal waves.

The excess APE suggests that either the internal tide is inherently nonlinear or,

as argued by Kunze et al. (2002), that the vertical isopycnal displacement caused by barotropic tidal flow over seafloor topography is the cause; in Monterey Canyon, removing the barotropic contribution to isopycnal displacement before calculating APE increased HKE/APE closer to the theoretical value (Hall and Carter, 2011). To account for this, we follow the method of Kunze et al. (2002) and calculate the barotropic contribution to isopycnal displacement ( $\xi_{bt}$ ) using a linear least squares fit to  $\xi(z)$  (Equation (6.2)), with zero at the surface. The barotropic contribution  $\xi_{bt}$  is then subtracted from  $\xi(z)$  and APE recalculated. Although the ratio is increased for all regions and is  $>1$ , it is in most cases  $<50\%$  of the theoretical value.

**Table 4.1:** HKE and APE (italics indicates recalculation of APE after the barotropic contribution to isopycnal displacement has been removed) integrated over the regions shown in Figure 4.15 and the resulting HKE/APE ratio (italics indicate where recalculated APE has been used).

	<b>HKE (TJ)</b>	<b>APE (TJ)</b>	<b><i>HKE/APE</i></b>
<i>Limb1a</i>	0.33	0.34/0.15	0.66/1.44
<i>Limb1b</i>	0.41	0.56/0.23	0.73/1.83
<i>Limb2</i>	1.87	2.96/1.29	0.63/1.44
<i>Limb3</i>	0.82	1.01/0.41	0.81/1.99
<i>Corrugation</i>	1.90	2.19/0.88	0.87/2.16
<i>Limb4</i>	0.99	1.50/0.66	0.66/1.51

Another possible explanation for excess APE is that partly standing internal waves are present within the canyon. Partially standing waves (the superposition of two free waves, with the same frequency but different amplitudes) result in the oscillation of HKE/APE between zero and infinity over the length of half of the wavelength of the waves (Martini et al., 2007). Down-canyon energy fluxes are observed in the depth-integrated maps of baroclinic energy flux (Figure 4.2 (a)) and also near the bottom of the canyon thalweg in the across- and along-canyon sections in Section 4.3.3. It is possible that superposition of the internal tide propagating up-canyon, and waves reflected from the supercritical canyon walls propagating down canyon form partially standing waves. This is further discussed in Section 4.3.3 using depth-integrated baroclinic  $M_2$  HKE and APE with distance along the canyon.

### 4.3.3 3D STRUCTURE OF THE $M_2$ INTERNAL TIDE

The three-dimensional structure of the internal tide is shown using along-canyon and across-canyon sections as defined in Figure 4.1. The thalwegs were picked manually using minimum slope and the depth contours to guide the picking. Distance along the canyon is referenced to the 1000-m isobath; positive distances are towards the head of the canyon and negative distances are towards the mouth of the canyon. For the along-canyon sections, both the along-canyon and across-canyon components of the baroclinic energy flux are shown, respectively defined as the energy flux tangential and normal to the localised thalweg orientation. Distance across the canyon is referenced to the thalweg; positive values are on the right when looking up canyon.

#### ALONG-CANYON SECTIONS

Along-canyon sections of depth-integrated along-canyon baroclinic  $M_2$  energy flux, HKE and APE, along-canyon and across-canyon baroclinic  $M_2$  energy flux, HKE and APE are shown in Figures 4.5 to 4.8. Sections for the minor limbs are provided in Appendix B.

With regards to the across- and along-canyon baroclinic fluxes, it is important to note that the colourbars used for limb 2a and 4b are different as they are much more energetic than limb 1a and 3a and so a different scale was appropriate. The across-canyon baroclinic energy flux, shown in panel (c) of Figures 4.5 to 4.8 is of a smaller magnitude than the along-canyon energy flux for all limbs. The small-scale spatial structure can mainly be attributed to the meandering path of the thalweg rather than a change in the direction of the energy flux, and possibly an artefact of interpolation. The along-canyon sections of baroclinic energy flux (shown in panel (b) of Figures 4.5 to 4.8) however show clear patterns of near-bottom intensification over the depth range of 1000 to ~2500 m, suggesting that topographic focusing is occurring within the canyon in all of the limbs (e.g. Gordon and Marshall, 1976). The clearest examples of near-bottom intensification however occur in limbs 1a, 3a and 4b, where there is also high along-canyon baroclinic energy flux near the surface and the seabed with near-zero at mid-depth. This is expected mode-1 structure. Much of the along-canyon baroclinic energy fluxes are positive i.e. up-canyon. However there are clear examples where down-canyon energy fluxes occur, such as in limb 1a where limbs 1b and 1c join limb 1a, where limb 2b joins 2a and limb 4b joins 4a, suggesting internal tide

generation within all of these minor limbs, which is then propogating down-canyon into the main limb.

Near-bottom elevated HKE and APE in across-sections of HKE and APE (shown in panels (d) and (e) of Figures 4.5 to 4.8) correspond to areas of bottom intensification in along-canyon baroclinic energy flux for all limbs. When HKE and APE are depth-integrated, a coherent pattern between all limbs is difficult to identify. However, some similarities can be seen between limbs 2a and 4a where HKE and APE are in roughly in phase with one another, whereas in limbs 1a and 3a this is not the case. The difference in phase could imply the presence of partially standing waves, however the meandering canyon path of the thalweg complicates the signal and it is beyond the scope of this study to determine whether this is the case.

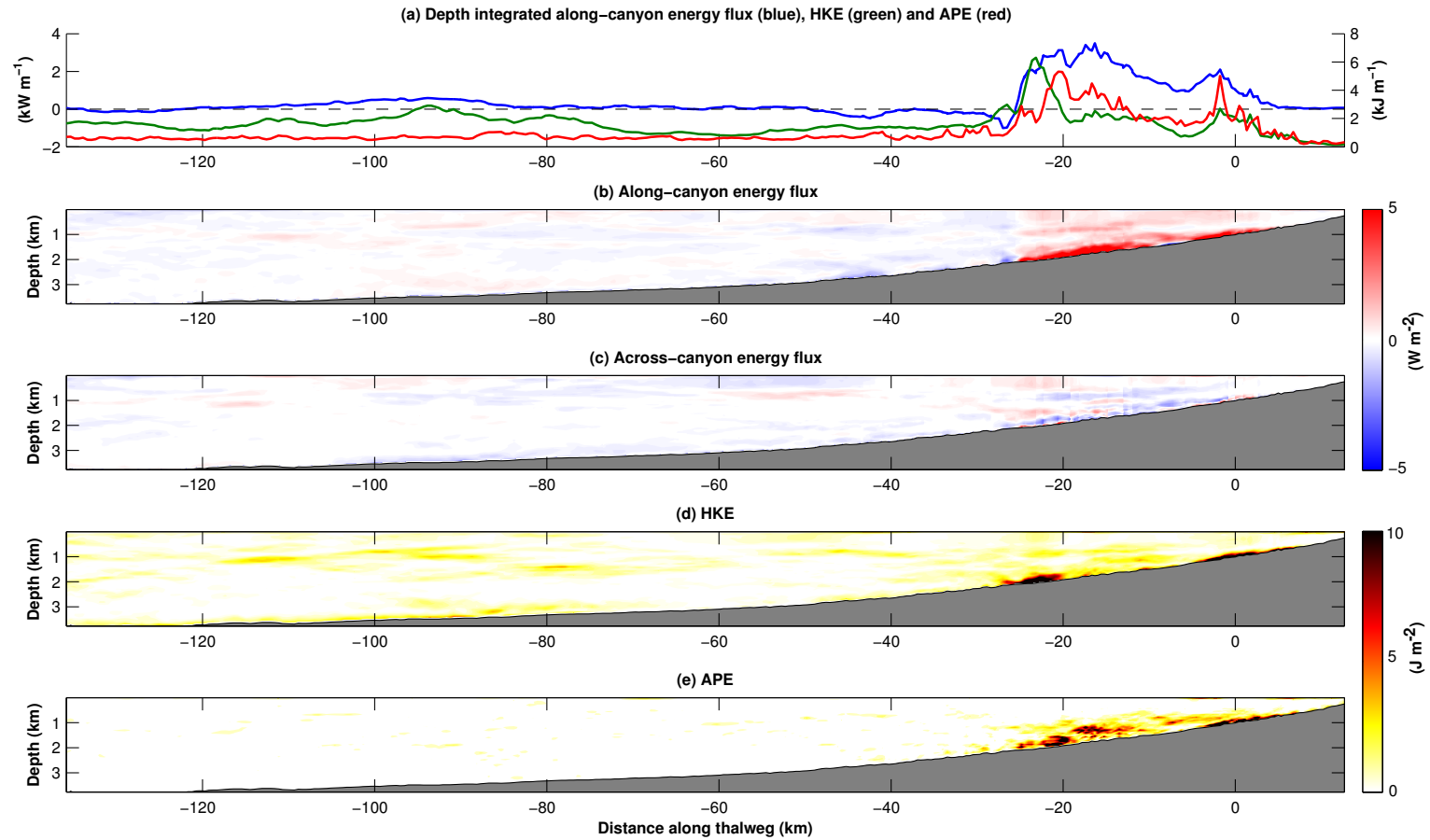


**Figure 4.5:** Limb 1a along-canyon sections (a) Depth-integrated along-canyon baroclinic  $M_2$  energy flux (blue), HKE (green) and APE (red) with distance along the thalweg. (b) Along-canyon and (c) cross-canyon baroclinic  $M_2$  energy flux with distance along the thalweg. Positive along-canyon values are towards the head of the canyon. Positive cross-canyon values are to the left when looking up canyon. (d) Along-canyon HKE. (e) Along-canyon APE. Distance along the canyon is referenced to the 1000-m isobath; positive distances are towards the head of the canyon and negative distances are towards the mouth of the canyon.

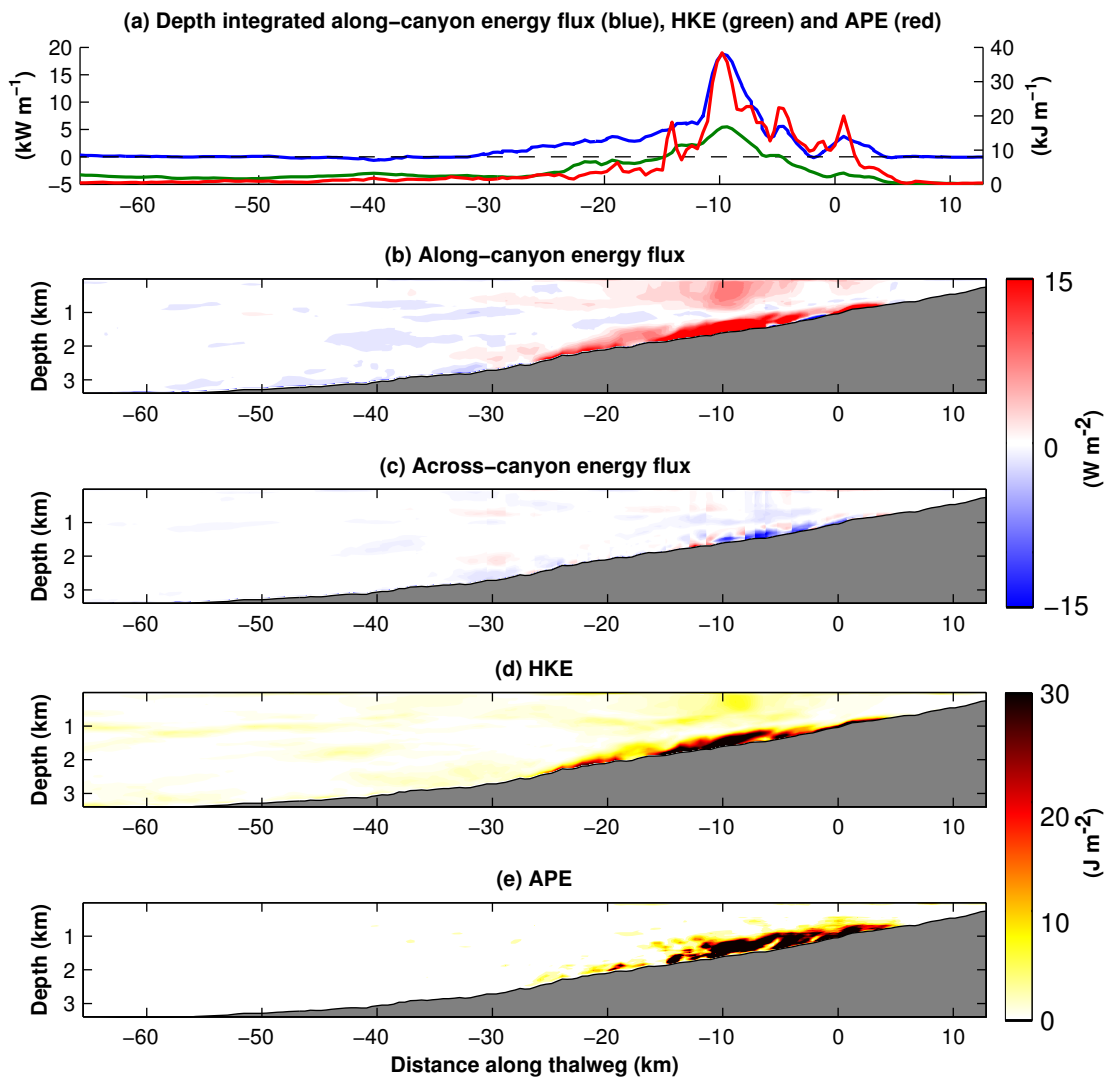


**Figure 4.6:** Limb 2a along-canyon sections. See Figure 4.5 for explanation. Note that the vertical scales are different.

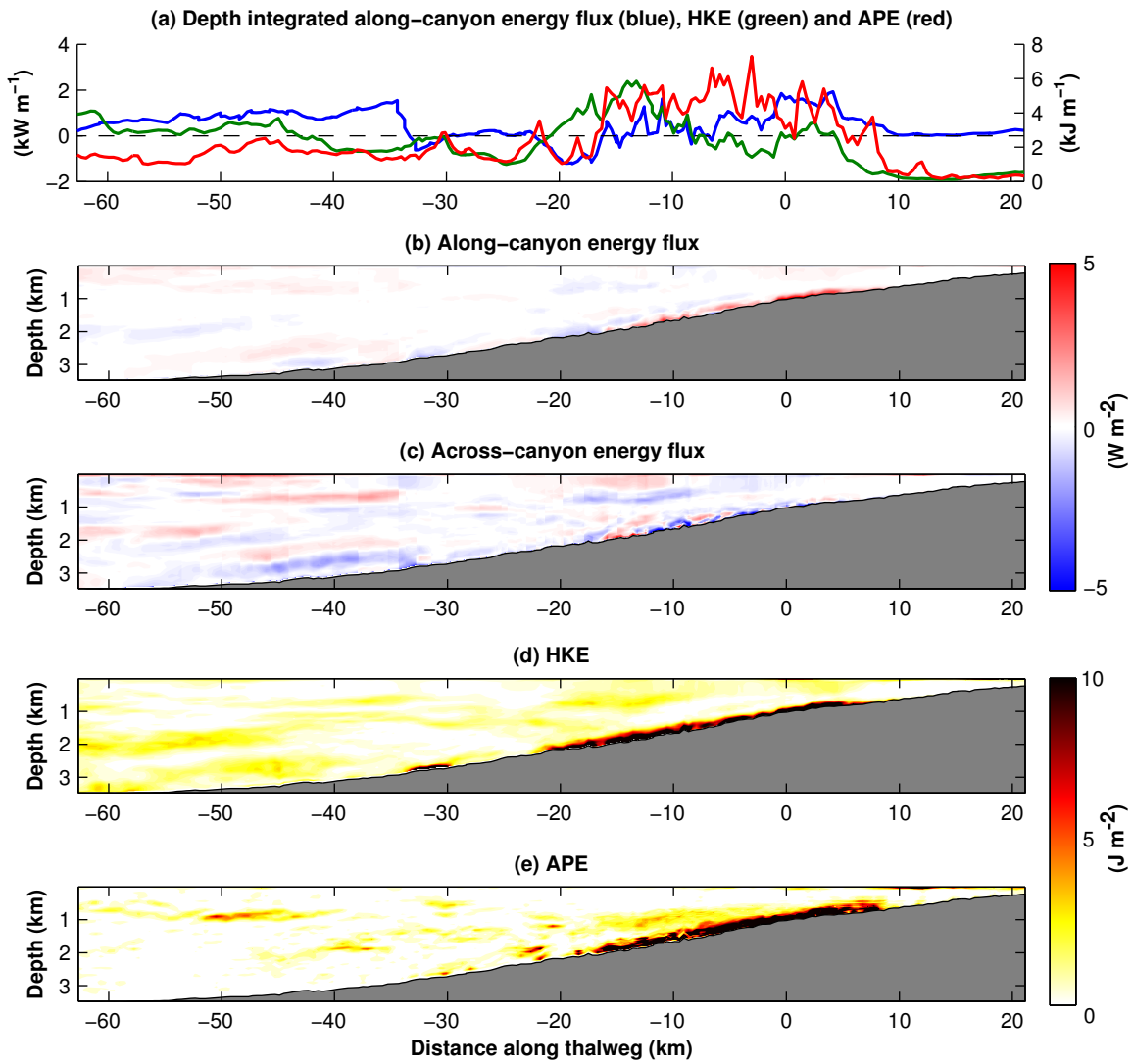


**Figure 4.7:** Limb 3a along-canyon sections. See Figure 4.5 for explanation. Note that the vertical scales are different.

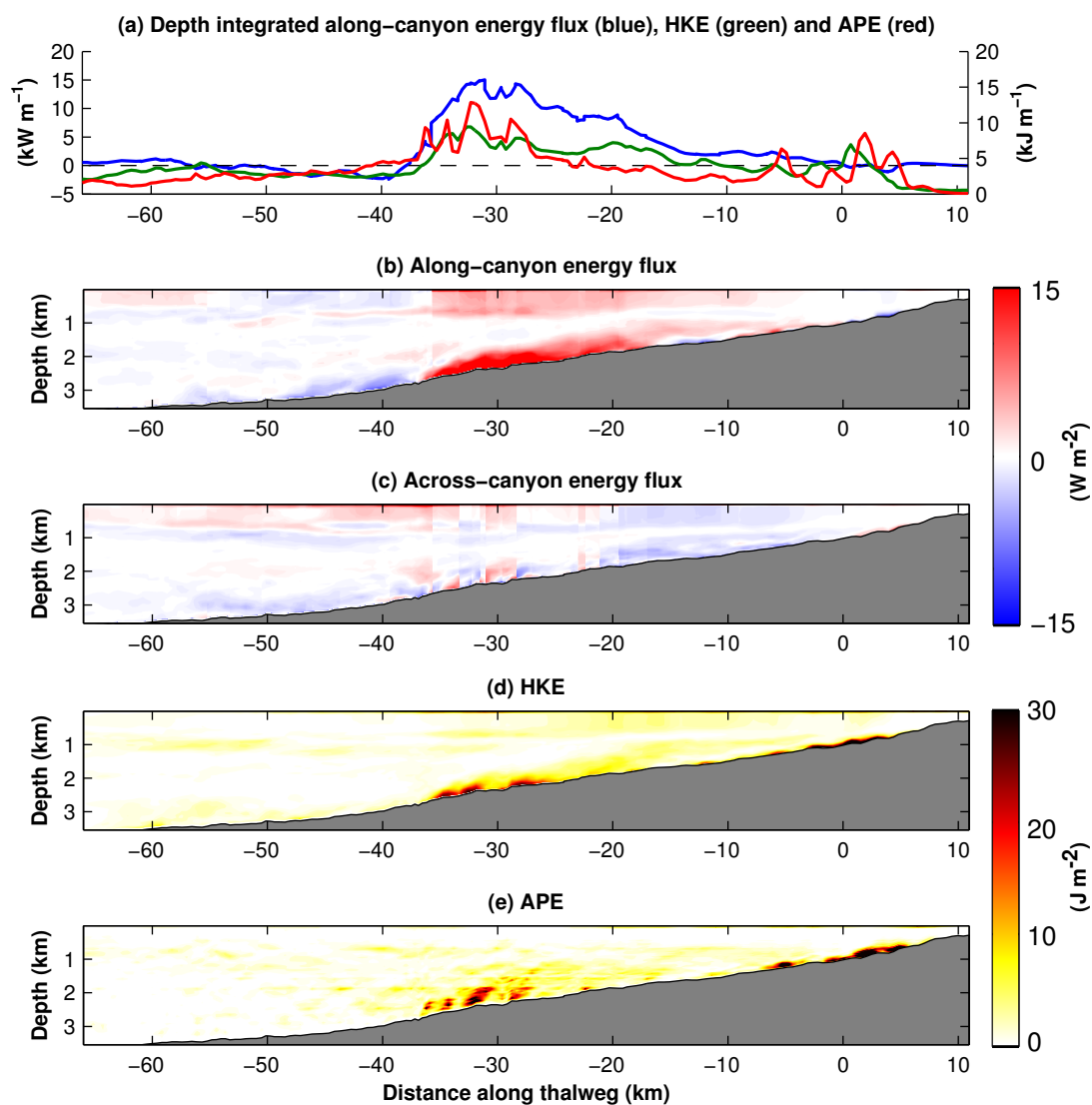


**Figure 4.8:** Limb 4a along-canyon sections. See Figure 4.5 for explanation.

### ACROSS CANYON SECTIONS

Limb 4 is a particularly energetic internal tide hotspot in Whittard Canyon, therefore across-sections of baroclinic energy flux for Limb 4a are provided (Figure 4.9). The across-canyon sections are generally not as informative as the along-canyon sections for the other limbs, they do demonstrate bottom-intensification of baroclinic energy flux, however due to the meandering path of the thalweg and the interpolation required to extract the sections, they are somewhat suspect. The across-canyon sections show that moving towards the head of the canyon, the baroclinic energy flux is bottom-intensified, with a typically mode-1 structure becoming dominant (Figure 4.9 (b)) but that the core of baroclinic energy flux propagating up the limb is absent by the 1000-m isobath (Figure 4.9 (a)). There is also some observable asymmetry in the core of baroclinic energy flux, but perhaps this is not that surprising as the cross-section of the canyon limbs are not symmetrical. The negative baroclinic energy flux observed in Figure 4.9 (c) appears to be linked to the limb, not part of the Whittard Canyon proper, that intersects the limb here.

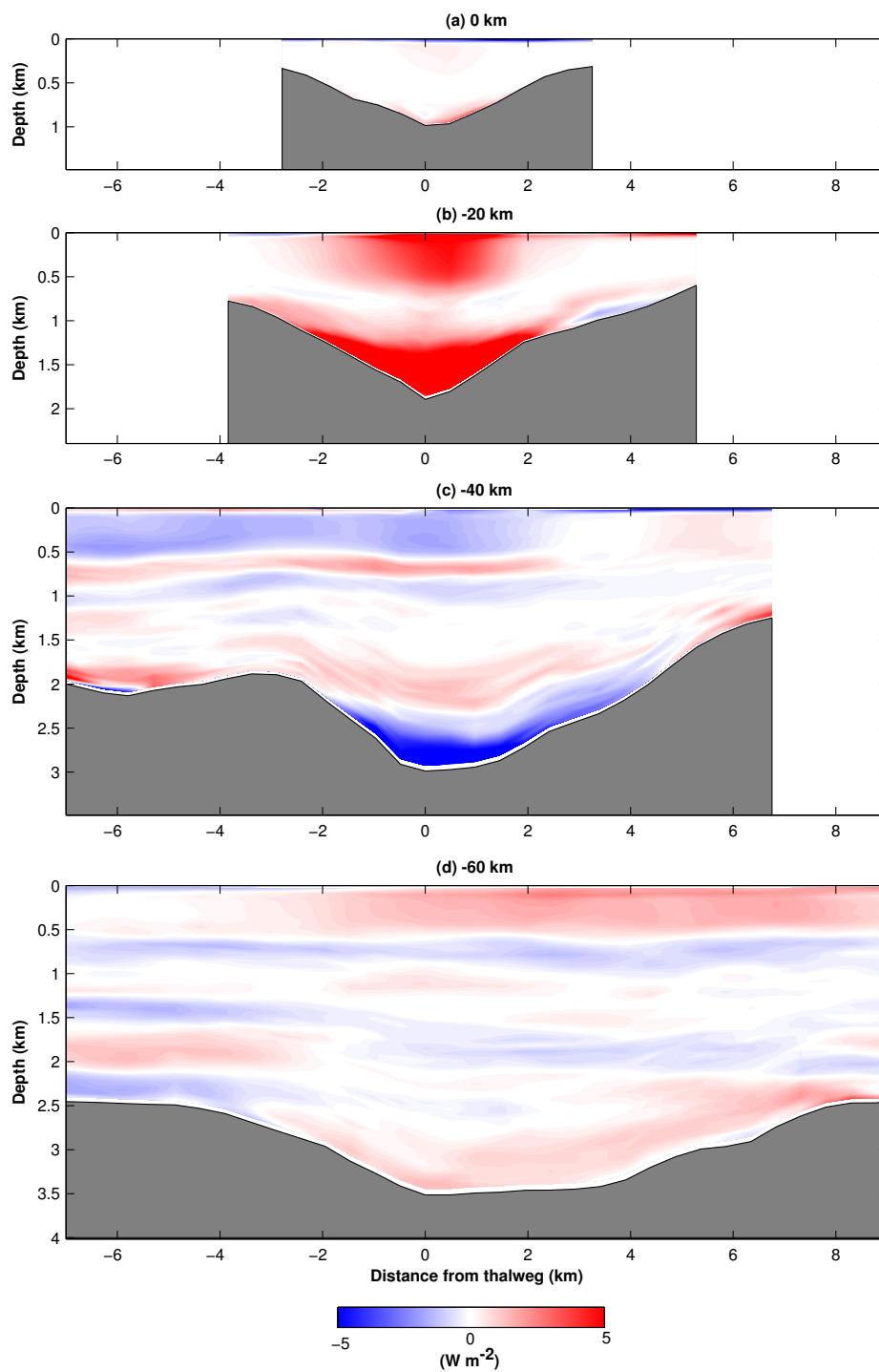


**Figure 4.9:** Along-canyon baroclinic  $M_2$  energy at cross-sections located at (a) -60 km, (b) -40 km, (c) -20 km, and (d) 0 km along the thalweg of Limb 4a (referenced to the 1000-m isobath). flux with distance along the thalweg. Positive along-canyon values are towards the head of the canyon.

#### 4.3.4 INTERNAL TIDE REFLECTION

As seen in the along- and across-canyon sections, bottom intensification of the internal tide occurs throughout the upper reaches of the canyon. The reflection of internal waves can lead to trapping and focusing of internal wave energy within canyons (Gordon and Marshall, 1976; Hotchkiss and Wunsch, 1982) resulting in bottom intensification. We therefore examine the reflective behaviour of the internal tide approaching the sloping canyon thalweg and walls to assess whether reflection of the internal tide within the canyon can explain the spatial patterns of baroclinic energy flux observed in Section 4.3.

The onshore-offshore propagation direction of deep water internal waves that have encountered a topographic slope can be calculated using the ratio of the topographic slope to the internal wave characteristic slope (criticality),

$$\alpha = \frac{s_{topog}}{s_{wave}} = \frac{\partial H / \partial x}{[(\omega^2 - f^2) / (N^2 - \omega^2)]^{1/2}} \quad (4.1)$$

where  $H$  is the total depth,  $x$  across-slope distance,  $\omega$  the angular frequency of the wave,  $f$  the inertial frequency and  $N$  the buoyancy frequency. If  $\alpha < 1$  (subcritical), after reflection, waves will continue to shoal. If  $\alpha > 1$  (supercritical), waves will travel back into deeper water after reflection. If  $\alpha = 1$  (critical), nonlinear effects and potential wave breaking can occur.

The map of criticality for the current model run (Figure 4.10) shows that much of the upper reaches of Whittard Canyon (depths less than 1000 m) are supercritical with respect to the  $M_2$  tide, whereas the abyssal plain, shelf and thalwegs of the lower reaches of the canyon (where they are typically U-shaped) are subcritical. The regions of the canyon bathymetry which are critical with respect to the  $M_2$  are not shown as they are not visible at this scale, however this region forms a thin band between the subcritical and supercritical regions.

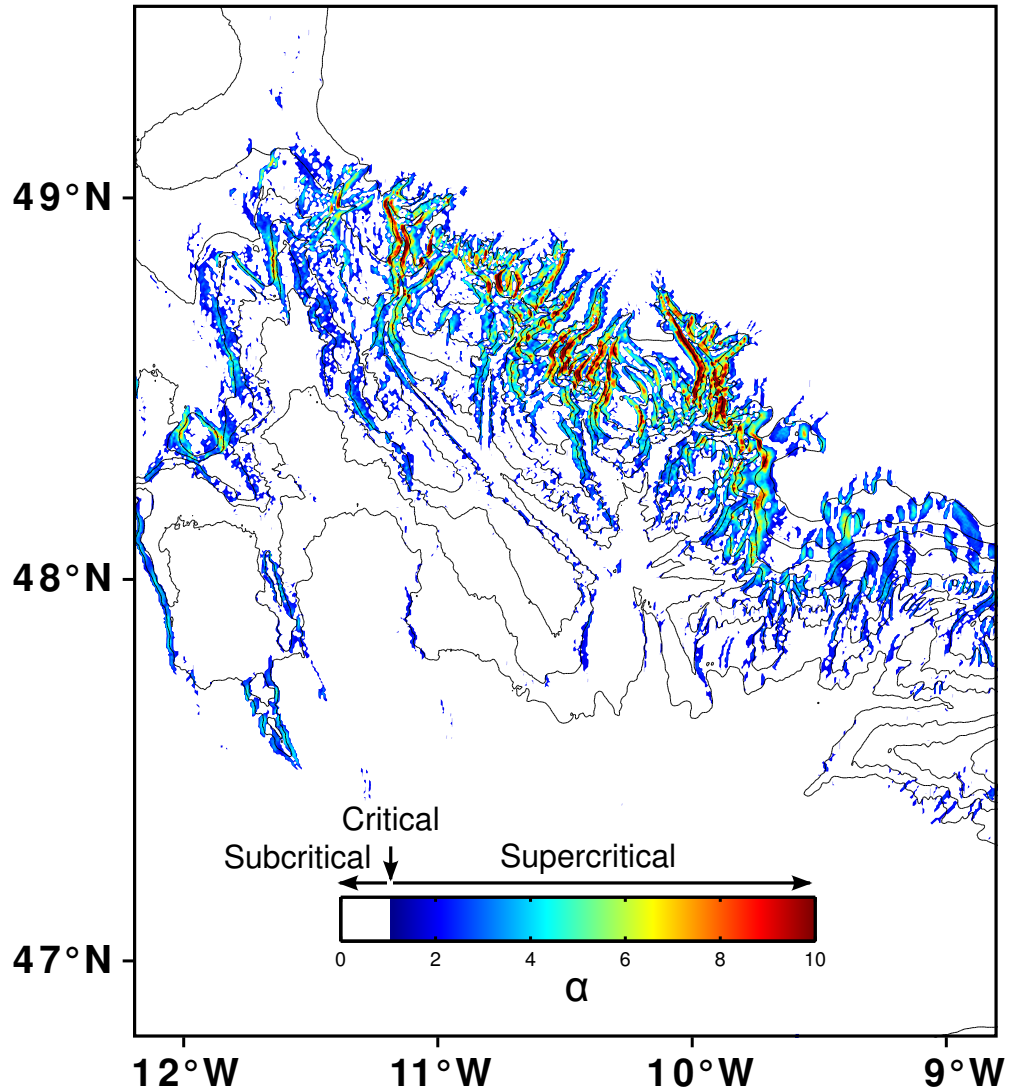


**Figure 4.10:** Map of the ratio of the topographic slope to the  $M_2$  characteristic slope,  $\alpha$  (criticality). Depth contours are plotted every 500 m.

The ocean, however, is inherently three-dimensional in nature. Therefore it is more instructive to think of internal waves as sheets intersecting topography (Carter and Merrifield, 2006). The slope of an internal tide beam that encounters topography is dependant on the orientation of the section with respect to the internal wave sheet. If the section is in the same plane as the sheet, the slope of the beam will equal  $s_{wave}$ . If the section is perpendicular to the sheet, the beam will be horizontal. To get a true measure of criticality it is therefore important to also know the direction of propagation of the internal tide. We therefore calculate  $\alpha$  for the along thalweg sections defined in Figure 4.1 assuming that the internal tide is propogating up-canyon, following a direct path along the thalweg. In reality, the internal tide is

unlikely to follow the small-scale meandering path of the thalweg, and more likely to travel a more direct path and cut across topography. A path that follows the thalweg will have a gentler topographic slope than one travelling a more direct path, and therefore the values of  $\alpha$  presented here are likely to be underestimates as the topographic gradients used in the calculation are lower than in reality. We use the experimental results of McPhee-Shaw and Kunze (2002) to define a ‘near-critical’ regime where topographic slopes match the condition  $0.8 < \alpha < 1.3$ . This broader definition of the critical regime is also less limiting than a strict definition of critical slopes only occurring at  $\alpha = 1$ ; the shortcomings of interpolating along the meandering thalweg, and also the somewhat unrealistic stratifications used, make such an exact value meaningless. The value of  $\alpha$  is then further smoothed using a running mean filter (5km) to aid diagnosis. The signal is likely noisy due to  $N^2$  profile used.

The along-canyon sections of  $\alpha$  are shown alongside the along-canyon baroclinic energy flux in Figures 4.11 to 4.14. Limb 1a, 2a and 4a are all similar in that the regions where  $\alpha$  is dominantly critical corresponds to where baroclinic energy flux is bottom intensified. Furthermore, the upper reaches of limb 1a, 2a and 4a are all supercritical with respect to the  $M_2$  characteristic slope. Limb 3a is markedly different for a number of reasons: firstly, it is concave in appearance compared to the other limbs, secondly, the head of the canyon is not supercritical and thirdly, the region of elevated baroclinic energy flux doesn’t correspond to values of  $\alpha$  that are critical. Investigations of internal tide reflection from convex slopes and concave slopes, however, do not show a reduction in mixing due to reflection for concave slopes as compared with the other slopes (Legg and Adcroft, 2003). It is therefore likely that it is the lack of a supercritical head that results in baroclinic energy not being focused as much in this limb.

For limb 4a,  $M_2$  internal tide characteristic slopes are calculated using the internal wave dispersion relation (Equation 1.1) and plotted on top of the section. They show that supercritical reflection at the head of the canyon reflects internal tide energy back into the canyon, the lack of such a mechanism in limb 3a may help to explain its reduced energy in comparison to the other limbs.

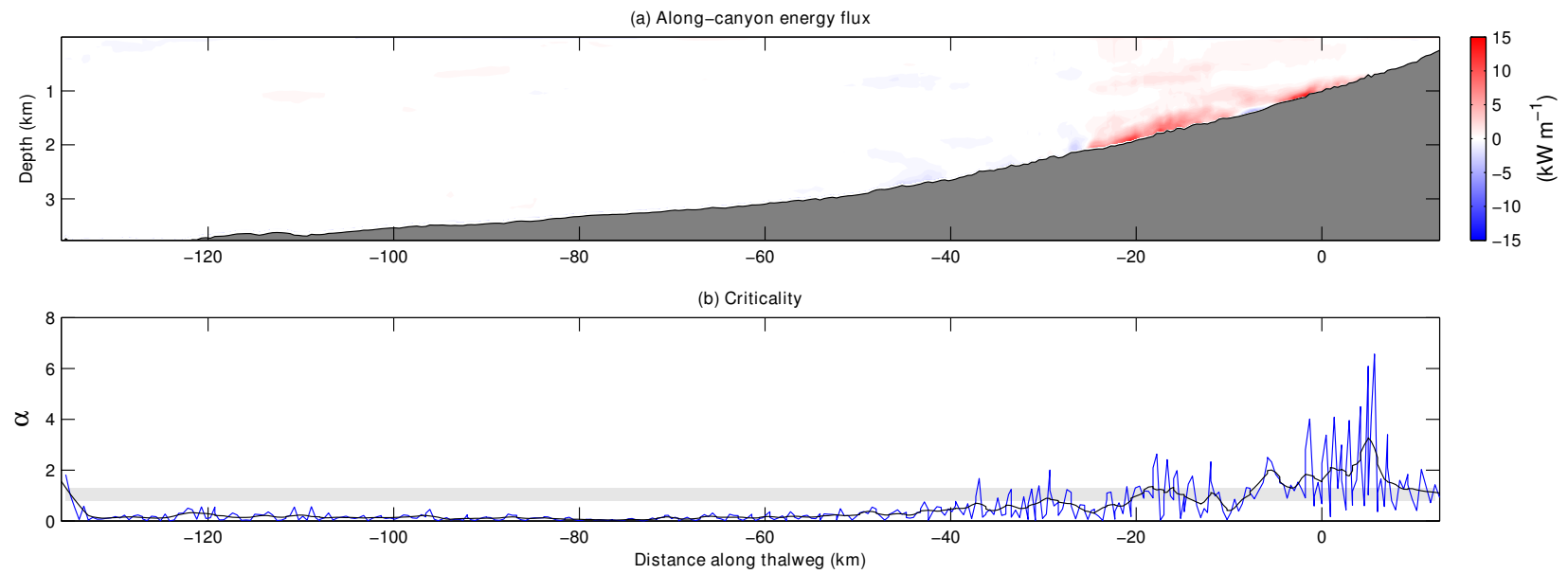


**Figure 4.11:** Limb 1a: (a) Along-canyon baroclinic  $M_2$  energy flux, with distance along the thalweg for Limb 1a. Positive along-canyon values are towards the head of the canyon. (b)  $\alpha$  with distance along the thalweg (blue) and  $\alpha$  smoothed with a running mean using a  $\sim 5$  km filter (black). The grey shaded region denotes the ‘near-critical region’ ( $0.8 < \alpha < 1.3$ ).

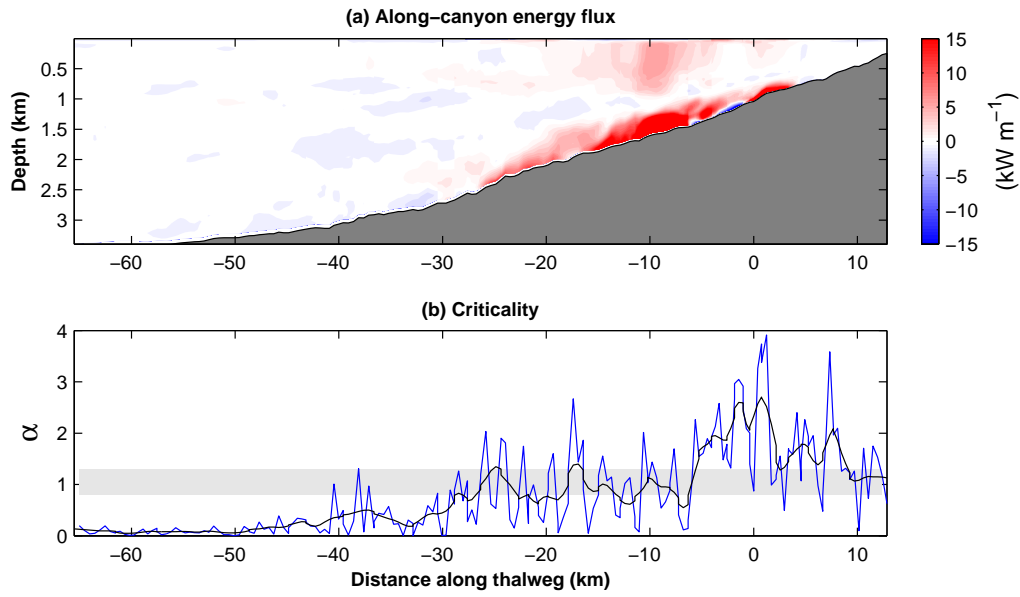


Figure 4.12: Limb 2a (see Figure 4.11 for explanation)

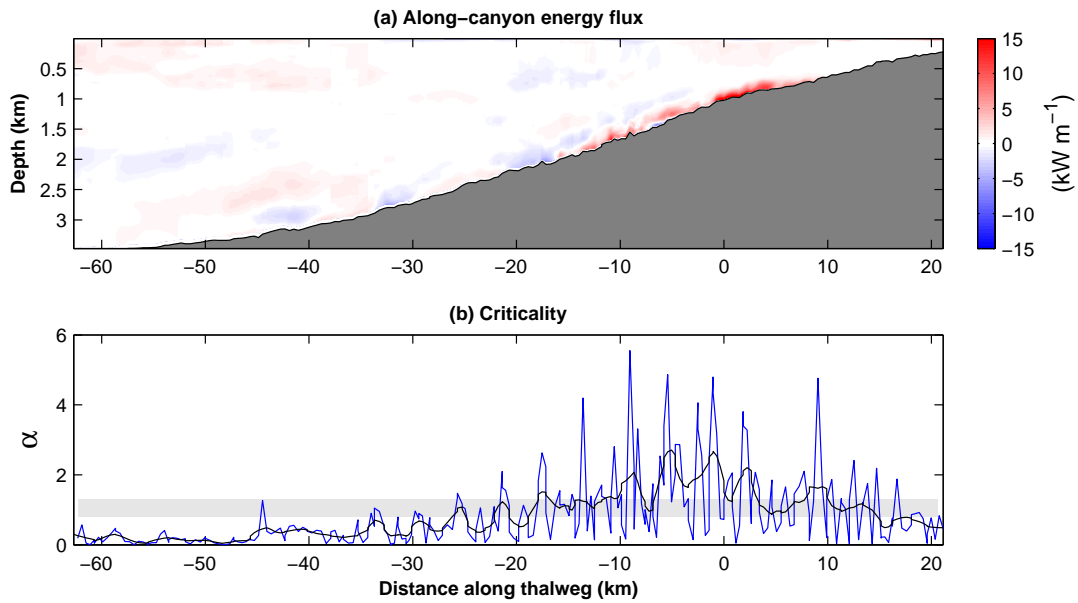
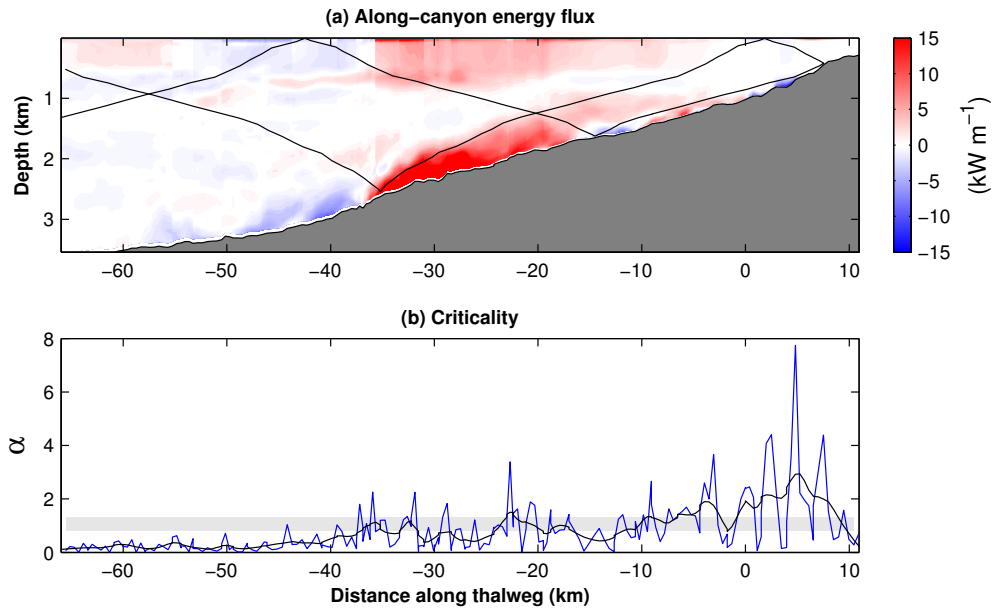


Figure 4.13: Limb 3a (see Figure 4.11 for explanation)



**Figure 4.14:** Limb 4a (see Figure 4.11 for explanation). An  $M_2$  internal tide characteristic slope for an internal tide propagating up canyon is calculated using the internal wave dispersion relation and is plotted over the section.

To better assess the differences in slope criticality between the main limbs, the fraction of the thalweg slope depth (between 500 m and 3000 m) that is subcritical, supercritical and near-critical for each main limb is calculated (Table 4.2). It becomes clearer that there are two main regimes: almost half of the thalweg slope by depth for limb 2a and limb 4a is supercritical to the  $M_2$  internal tide, whilst for Limb 1a and Limb 3a less than a third of the slope is supercritical to the  $M_2$  internal tide. Limb3a is notable for having the largest fraction of near-critical slope (0.49), followed by limb 1a.

**Table 4.2:** Fraction of depth between 500 m and 3000 m depth that are subcritical, supercritical and near-critical for the main limbs within Whittard Canyon.

	$\alpha < 0.8$	$0.8 < \alpha < 1.3$	$\alpha > 1.3$
<b>Limb 1a</b>	0.35	0.37	0.28
<b>Limb 2a</b>	0.25	0.28	0.47
<b>Limb 3a</b>	0.21	0.49	0.30
<b>Limb 4a</b>	0.26	0.27	0.48

#### 4.4 CANYON ENERGY BUDGET

As discussed previously, different patterns of modelled barotropic-to-baroclinic energy conversion and baroclinic energy flux are seen in the various limbs. To investigate these differences in more detail, and to estimate dissipation within the canyon, the upper canyon was divided into 6 regions (Figure 4.15). Each region was defined using the spatial pattern of depth-integrated baroclinic energy flux as a guide, and also the 300-m isobath, which was used to define the northernmost extent of each region. For each region, baroclinic energy flux divergence (net energy flux out of the region) and net barotropic-to-baroclinic energy conversion are calculated (Table 4.3). Assuming that all net energy (net energy conversion minus energy flux divergence) into each region is dissipated, baroclinic energy dissipation can then be calculated.

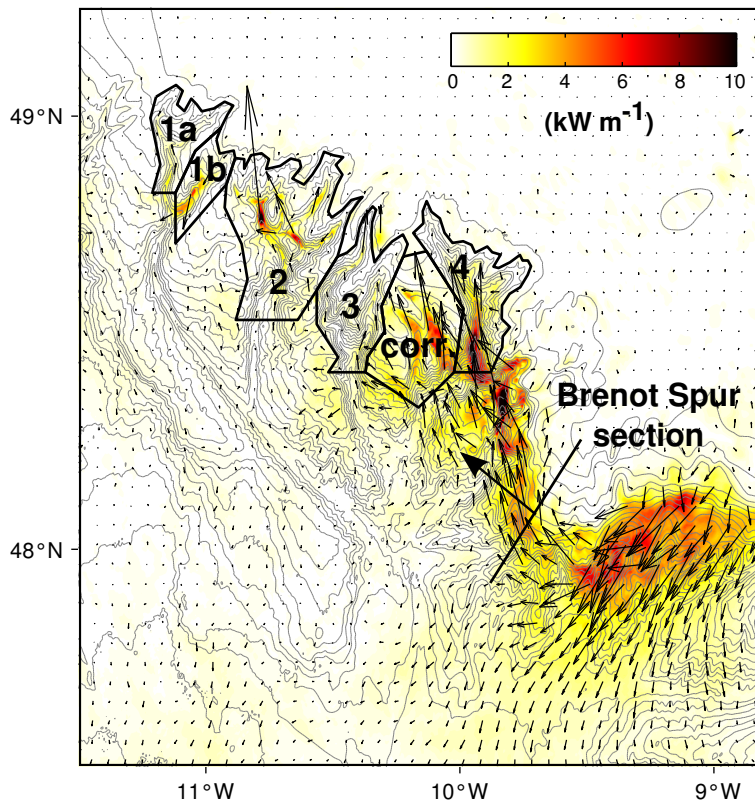


**Figure 4.15:** Depth-integrated baroclinic  $M_2$  energy flux in the Whittard Canyon region. Vectors are plotted every 40 model grid points ( $\approx 20$  km) in each direction. The underlying colour is the energy flux magnitude. Depth contours are plotted every 200 m. The regions used to calculate the canyon energy budget are outlined in black and correspond to the canyon limb naming convention used in this thesis. A corrugated region (corr.) is also used. The Brenot Spur section is also included and the arrow indicates the direction of the flux calculated (44 MW).

**Table 4.3:** Model baroclinic energy estimates integrated over the regions shown in Figure 4.15, including: baroclinic energy flux divergence, barotropic to baroclinic energy conversion and baroclinic energy dissipation.

	Flux Divergence (MW)	Conversion			Dissipation	
		Positive (MW)	Negative (MW)	Net (MW)	Total (MW)	Rate ( $\times 10^{-8} \text{ W kg}^{-1}$ )
<i>Limb1a</i>	-1.8	15.9	8.0	7.9	9.7	3.79
<i>Limb1b</i>	7.7	15.5	3.0	12.5	4.8	2.10
<i>Limb2</i>	2.9	101.7	31.3	70.3	67.4	5.20
<i>Limb3</i>	-2.9	32.6	15.9	16.8	19.7	2.65
<i>Corrugation</i>	-35.2	65.8	28.9	36.9	72.1	7.65
<i>Limb4</i>	-15.4	81.6	60.4	21.3	36.7	6.37

As anticipated from the cessation of the northwest propagating beam of depth-integrated baroclinic energy flux (Figure 4.2), baroclinic energy flux divergence is strongly negative (i.e. convergent) in *Limb4* and the *Corrugation* region (-15.4 MW and -35.2 MW, respectively). The positive value of energy flux divergence in *Limb1b*, corresponds to the down-canyon depth-integrated baroclinic energy fluxes seen in Figure 4.2, indicating that baroclinic energy is leaving the canyon and entering *Limb1a*. However, it is not as easy to diagnose as obvious a cause of the positive value of flux divergence in *Limb2* from the pattern of depth-integrated baroclinic energy flux.

All regions within Whittard Canyon display positive net energy conversion, with the largest value occurring in *Limb2* (70.3 MW). Positive conversion implies local internal tide generation whilst negative values indicate work done on the barotropic tide by the baroclinic tide (Zilberman et al., 2009), therefore it is instructive to also look at the positive and negative components of energy conversion. The largest value of positive energy conversion occurs in *Limb2* (101.7 MW), although both *Limb4* and the *Corrugation* region also have large amounts of positive conversion (81.6 and 65.8 MW, respectively). Local internal tide generation in association with positive energy conversion is partially compensated by negative energy conversion occurring within these regions, although the degree to which this occurs varies spatially. For example, 74% of positive energy conversion is compensated for by negative energy conversion

within *Limb4a* whilst in *Limb1b* only 19% is compensated for.

Total baroclinic energy dissipation in the upper canyon (sum of all 6 regions), inferred from both baroclinic energy flux divergence and barotropic-to-baroclinic energy conversion, is 0.21 GW. Net energy conversion in the upper canyon is 0.17 GW (81% of total energy), and so has a significant effect on total baroclinic energy dissipation. The resulting dissipation (net energy conversion minus flux divergence) is largest in the *Corrugation* region (72.1 MW) and *Limb2* (67.4 MW). However, to compare individual regions it is important to take into account the relative size of each region by dividing total dissipation by the mass of seawater in each region (using a constant seawater density of  $1025 \text{ kg m}^{-3}$ ). The dissipation rate is highest in the *Corrugation* region ( $7.65 \times 10^{-8} \text{ W kg}^{-1}$ ) and *Limb4* ( $6.37 \times 10^{-8} \text{ W kg}^{-1}$ ), providing further evidence that they are significant sinks of the baroclinic energy entering the canyon from the generation regions to the east (Section 4.2). It is interesting to note that dissipation is high in *Limb2* and *Limb4* but for very different reasons: residual energy in *Limb2* is primarily due to local internal tide generation (large positive net energy conversion) whilst for *Limb4* negative flux divergence contributes as much to total dissipation as positive net energy conversion. Dissipation rates in the other limbs (*Limb1a*, *Limb1b* and *Limb3*) are smaller as a result of lower flux divergence and energy conversion.

## 4.5 INTERNAL TIDE PROPOGATION ON SHELF

Depth-integrated baroclinic energy fluxes on the continental shelf (defined here as any depths less than 300 m) are typically an order of magnitude smaller than those throughout Whittard Canyon ( $<0.5 \text{ kW m}^{-1}$ ) (Figure (4.16 (a))). However, there are regions of elevated energy fluxes ( $>1 \text{ kW m}^{-1}$ ) near the head of the canyon, notably at the head of Limb 3, where energy fluxes  $>2 \text{ kW m}^{-1}$  occur. There appears to be no consistent orientation for the energy fluxes along the shelf break, with the orientation changing from on-shelf to off-shelf over short distances e.g. between 50 and 100 km along the 300-m isobath (Figure (4.16 (a))).

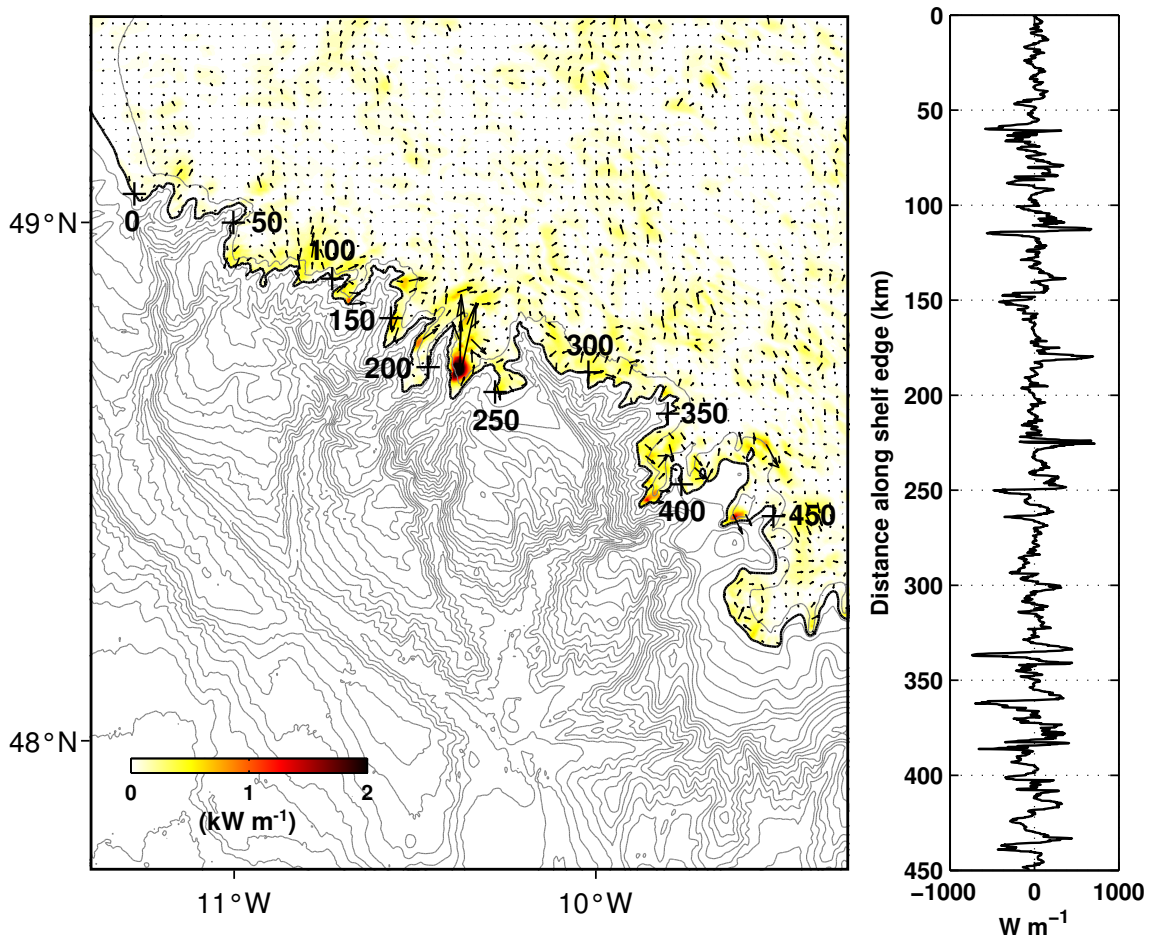


**Figure 4.16:** (a) Depth-integrated baroclinic  $M_2$  energy flux on the continental shelf. Vectors are plotted every 5 model grid points ( $\approx 2.5 \text{ km}$ ) in each direction. The underlying colour is the energy flux magnitude. Depth contours are plotted every 200 m and the black line is the 300-m isobath, the approximate depth of the shelf break. Distance along the 300-m isobath is marked with a cross at 50 km intervals (b) Depth-integrated across-slope baroclinic  $M_2$  energy flux with distance along the 300-m isobath. Positive values indicate a flux onto the shelf.

The baroclinic energy flux across the shelf edge is defined here as the baroclinic energy flux normal to the 300-m isobath (Figure 4.16 (b)). The resulting energy flux is noisy because of the meandering path of the isobath, similar to the situation encountered with the along canyon sections (Section 4.3.3). Along most of the 300-m isobath the depth-integrated energy flux typically fluctuates between  $\pm 100 \text{ W m}^{-1}$ , however, at the head of Limb 4 the depth-integrated energy flux is elevated and fluctuates between  $\pm 300 \text{ W m}^{-1}$ . Peaks in on-shelf depth-integrated energy flux of order  $700 \text{ W m}^{-1}$  occur at the head of Limb 2 and Limb 3. Peaks in off-shelf depth-integrated energy flux of order  $700 \text{ W m}^{-1}$  occur over the head of Limb 4, and smaller off-shelf fluxes ( $600 \text{ W m}^{-1}$ ) occur over the heads of Limb 1b and Limb 2. Integrated along the length of the 300-m isobath, the net on-shelf baroclinic energy flux is 3.38 MW. However, when split into positive (28.7 MW) and negative (-25.3 MW) components, it becomes clear that a significant amount of energy is not only going on-shelf, but is also entering the canyon from generation on the shelf.

## 4.6 DISCUSSION AND CONCLUSIONS

Within this section, the above results are discussed and overall conclusions made about the generation, propagation and dissipation of the baroclinic  $M_2$  internal tide in Whittard Canyon.

### 4.6.1 INTERNAL TIDE GENERATION

Following on from the sensitivity studies in Chapter 2, Shamrock Canyon and the western flank of Brenot Spur are identified as a key generation site where elevated depth-integrated baroclinic energy fluxes ( $> 0.2 \text{ W m}^{-2}$ ) occur in parallel with regions of high barotropic-to-baroclinic conversion ( $> 6 \text{ kW m}^{-1}$ ). A beam of baroclinic energy flux propagates northwest from these source areas and onto the shelf via limb 4a, seemingly constrained by the limb morphology. The strength of the northwest propagating beams appears to be due to the interaction between local generation within the canyon and its original remote source, resulting in baroclinic energy fluxes within limb 4a that are  $> 8 \text{ kW m}^{-1}$ .

Internal tide generation also occurs locally, but variably so in different limbs: limb 2 and limb 4 show more positive barotropic-to-baroclinic conversion occurring within them than in limb 1 and 3. Limbs 2a and 4a also display ‘twinning’ of regions of strongly positive and negative barotropic-to-baroclinic energy conversion. This asymmetric conversion over the upper canyon limbs, where negative conversion occurs on the eastern side, and positive conversion occurs over the western side has been observed previously in numerical models of canyons. Petrucio et al. (2002) observed asymmetric conversion in simulations of Monterey Canyon, suggesting that the asymmetrical form of conversion was due to the Earth’s rotation. However, a more recent idealised canyon modelling study by Zhang et al. (2014) of symmetric canyons also found that barotropic-to-baroclinic energy conversion rates were typically asymmetric. They suggest that the cross-canyon asymmetrical pattern is caused by multiple-scattering effects on one canyon side slope, caused by the phase variation in the internal-tide sources.

Areas of negative energy conversion (energy transfer from the baroclinic tide back to the barotropic tide) in our model can be explained by a flux-conversion

feedback. The  $p'$  term occurs in both the energy flux and conversion equations, however it has both local ( $p'_{local}$ ) and remote ( $p'_{remote}$ ) components. Depending on the phase of  $p'_{remote}$ , it can either enhance or suppress local  $E_{conv}$  (Kelly and Nash, 2010). The remote source of pressure perturbation over the canyon can be considered fixed, however the vertical velocity,  $w_{Bt}$ , caused by barotropic flow across sloping topography will vary over the canyon width and the resulting  $p'_{local}$  will also have a phase offset from this term. Therefore if the resulting  $p'$  term is approximately  $180^\circ$  out of phase with  $w_{Bt}$ , then conversion will be negative. If the resulting  $p'$  term is approximately  $0^\circ$  out of phase with  $w_{Bt}$ , then conversion will be positive (Figure 4.17). The asymmetry observed implies that local internal tide generation is modulated by remote generation sites, and as such, the domain size of the model needs to be sufficiently large enough to contain all the remote generation sites that can impact local generation within the canyon. This conversion-feedback mechanism is also expected to affect the along shelf propagation of internal waves.

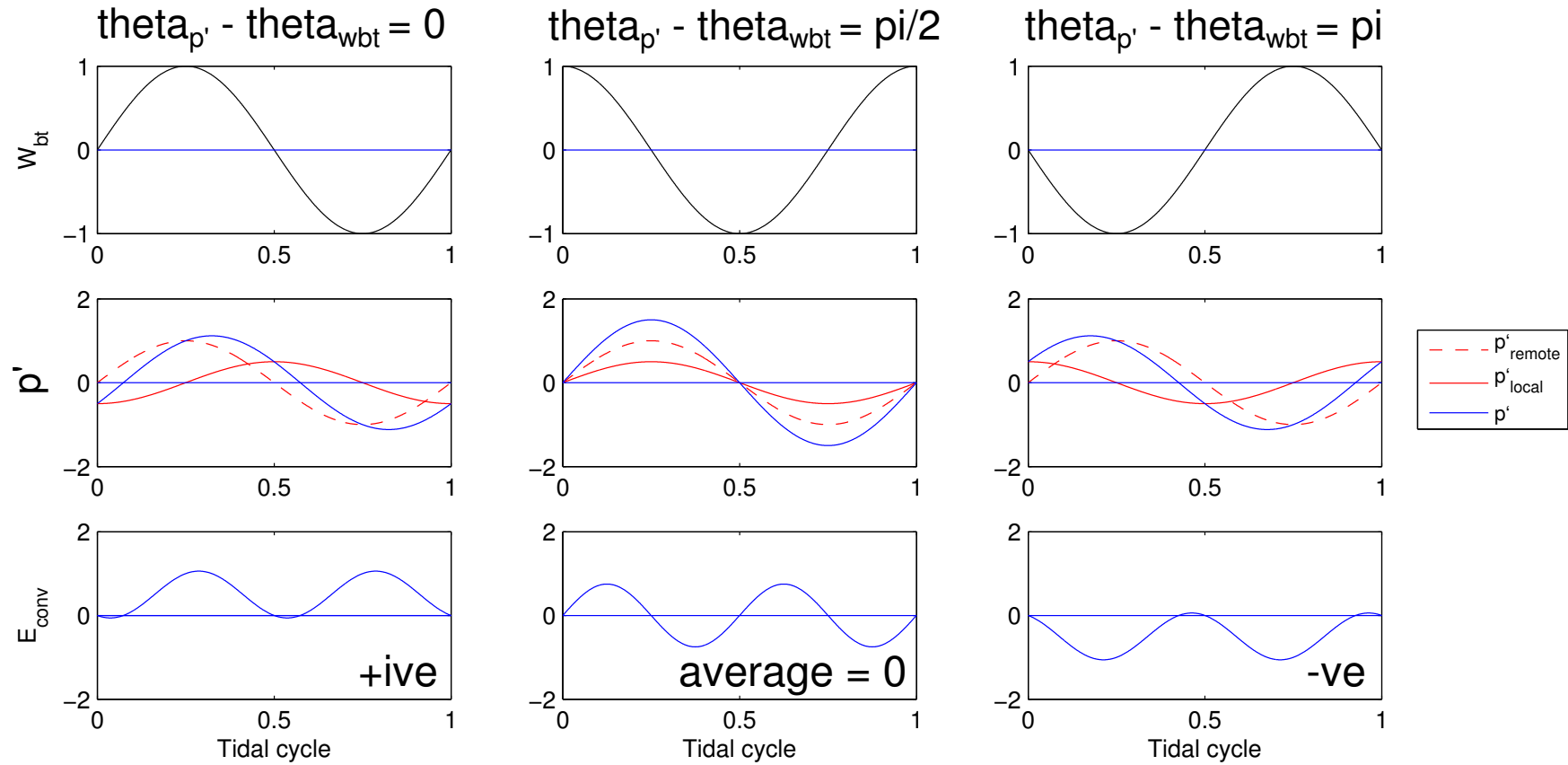


**Figure 4.17:** Flux-conversion feedback showing how a fixed remote source ( $p'_{remote}$ ), but variable local generation ( $p'_{local}$  and  $w_{BT}$ ) leads to conditions where positive (left), zero (centre) and negative (right)  $E_{conv}$  occur

#### 4.6.2 INTERNAL TIDE PROPOGATION THROUGH WHITTARD CANYON

The internal tide within Whittard Canyon is topographically steered, with enhanced internal tide bottom currents reaching  $0.4 \text{ m s}^{-1}$  in the upper reaches of the canyon, in broad agreement with published values (Amaro et al., 2016). Depth-integrated baroclinic energy fluxes are dominantly up-canyon, however, some occurrences of down-canyon fluxes occur too, primarily in minor limbs e.g. limb 1b. Depth-integrated baroclinic energy flux within the canyon is elevated, but variably so in different limbs. Limb 4 is the most energetic, and this is attributed to it being directly in the path of the northwest propogating beam of baroclinic energy flux originating in the Shamrock Canyon and Brenot Spur region. HKE and APE are also elevated over the upper reaches of the canyon, however, excess APE suggests that partially standing waves, caused by the superposition of waves, may be present within the canyon. However, it is hard to diagnose whether they are definitely present using the diagnostics used in this thesis.

Along-canyon sections of the various limb also indicate different internal tide regimes within the canyon: limb 2a and 4a are more energetic than limbs 1a and 3a. However, all limbs show near-bottom intensification of the internal tide over the depth range of 1000 to 2500 m, suggesting that topographic focusing of the internal tide occurs in all limbs. Limbs 1a, 3a and 4b also display a clear mode-1 structure, which is also seen in across-canyon sections of limb 4a. Negative baroclinic energy fluxes are also encountered, however they predominantly occur in the minor limbs. The reflective behaviour of internal waves in the different limbs is also different, as indicated by along-canyon sections of criticality. Cores of baroclinic energy flux are correlated with the depths over which the thalweg slope is dominantly critical with respect to the internal tide characteristic slope for most of the limbs with the head of the canyon heads typically being supercritical. This further helps to explain the near bottom intensification of the internal tide within the canyon. A three-dimensional focusing mechanism has been proposed by Vlasenko et al. (2016) in the minor canyons to the east of Whittard Canyon, and it is therefore likely that a similar process is acting here.

It is important to note that the current model doesn't capture the variability in stratification that has been observed in the different limbs (Wilson et al., 2015b),

due to the use of a horizontally uniform stratification across the whole domain. Diffusivities in the model are set to zero so that stratification is not lost due to mixing in the absence of a restoring buoyancy flux, this means that stratification in the model cannot evolve as it would in the canyon limbs in reality. Changes in stratification can change the propagation behaviour of an internal tide (Mohn et al., 2014), therefore in reality the propagation of the internal tide is likely to differ in the upper reaches of the canyon limbs where stratification breaks down.

### 4.6.3 CANYON ENERGY BUDGET

The dissipation rates along the shelf in our model are highly variable, even over just the region occupied by Whittard Canyon, varying between  $2.10 \times 10^{-8} \text{ W kg}^{-1}$  and  $7.65 \times 10^{-8} \text{ W kg}^{-1}$ . Dissipation rates calculated for other canyons using POM forced only by the  $M_2$  tidal constituent are comparable to the results presented here e.g.  $3.99 \times 10^{-8} \text{ W kg}^{-1}$  for Monterey Canyon (Hall and Carter, 2011) and  $7.66 \times 10^{-8} \text{ W kg}^{-1}$  for Ascension Canyon (Gregg et al., 2011). The highly variable dissipation results calculated here across different limbs in the canyon have implications for mixing parameterisations at the shelf edge in models, and offer an opportunity to refine such parameterisations by including the effect of dendritic canyons at the shelf edge.

### 4.6.4 INTERNAL TIDE PROPOGATION ON SHELF

The depth-integrated across-slope baroclinic energy flux along the 300-m isobath, is highly variable along the length of the shelf edge occupied by Whittard Canyon, with positive and negative on-shelf fluxes being observed. Values reaching up to  $700 \text{ W m}^{-1}$  are reached, however the interpolation along the winding 300-m isobath creates a noisy signal which oscillates from negative to positive values. Observations of energy flux onto the shelf from Whittard Canyon are limited, however, measurements taken to the east of Whittard Canyon show that the semi-diurnal tide drives  $28\text{-}48 \text{ W m}^{-1}$  of energy on-shelf (Hopkins et al., 2014) with the positive on-shelf energy flux also being modulated by nonlinear interactions with the vertical shear of inertial oscillations, leading to increases of  $25\text{-}43 \text{ W m}^{-1}$  in the energy flux. There appears to be no constant orientation for the energy fluxes along the shelf break. The across-shelf internal wave energy flux is often assumed to be controlled

by the orientation of the shelf break (Garrett and Kunze, 2007), however, observations show that the propagation of internal waves onto the Celtic Sea Shelf is in random directions (Holt and Thorpe, 1997; Pingree et al., 1981), in agreement with our model. This is likely due to the corrugated nature of the shelf edge, as has been shown in other regions e.g. the Virginia continental slope (Nash et al., 2004).

The internal tide generated at the Celtic Sea shelf break has been observed as a coherent signal up to 170 km onto the shelf (Inall et al., 2011). Much of the energy generated at the shelf edge is dissipated at or near the shelf break with an estimated shoreward energy decay scale of 42 km (Inall et al., 2011). The decay scale in our model is likely to not be realistic due to non-linear effects not being resolved in the model, they can only be inferred.

It is likely that changes in stratification would change the propagation of the internal tide onto the shelf. Reduced near-surface stratification in a winter stratification scenario is likely to inhibit the baroclinic energy flux released onto the shelf. This could be investigated quite easily in the future by changing the stratification in the model.

#### 4.6.5 CONCLUSIONS

The internal tide within Whittard Canyon is spatially complex, however, through this work the key generation sites have been identified. Shamrock Canyon and the region to the west of Brenot Spur are key remote sources of baroclinic energy. Local generation also occurs within the canyon, but is modulated by a flux-conversion feedback that is dependant on the phase of the remotely generated internal waves. The results presented here highlight how important choosing the correct domain size is for barotropic-to-baroclinic conversion to be estimated accurately, as if key remote sources are omitted, even local generation is affected. The Bay of Biscay to the east, and the corrugate slope to the north of Whittard Canyon may be a source of farfield generation for Whittard Canyon, so it is advised that a much larger domain size be used to identify whether this is the case. Furthermore, internal tide barotropic-to-baroclinic conversion is also dependant upon bathymetry, therefore sufficiently high resolution topography is required to accurately estimate conversion. The effect of smoothing the bathymetry is examined in Chapter 5, following the work of Zilberman

et al. (2009).

The internal tide is enhanced throughout all limbs in the canyon, but variably so, relating to different remote sources of internal tides and differing reflection regimes. The propagation of the internal tide is dominantly up-slope and the corresponding baroclinic energy flux is bottom intensified along depths of 1000-2500 m which correlates with the position of the permanent thermocline within the region. The permanent thermocline associated with the MOW is likely to act as a waveguide for freely propagating internal waves, focusing energy at the seabed (Puig and Palanques, 1998). This work provides confirmation that internal wave activity is enhanced over the region associated with the permanent thermocline, with implications for biology (Amaro et al., 2016) and the formation of nepheloid layers (Wilson et al. (2015b).



# 5

## **EFFECTS OF BATHYMETRIC RESOLUTION ON THE MODELLING OF INTERNAL TIDES**

### **5.1 INTRODUCTION**

The length scales at which internal waves operate over (kilometres) and which topography can vary over are vastly different. High resolution bathymetry, on the order of metres is available for the Whittard Canyon, however, increasing bathymetric resolution within POM is computationally expensive and it is unclear what topographic resolution the model requires to accurately simulate the internal wave field. Previous work by Zilberman et al. (2009) on the Mid-Atlantic Ridge identified the importance of using high resolution bathymetry to accurately model barotropic-to-baroclinic energy conversion over such topography using POM. To our knowledge, however, no such sensitivity study has been carried out for canyon-type morphologies.

This chapter investigates how changing the resolution of the bathymetry used affects modelled barotropic-to-baroclinic energy conversion, baroclinic energy flux and inferred dissipation and whether, given the scale of internal tides, such high resolution bathymetry is needed.

## 5.2 BATHYMETRIC GRIDS

A number of bathymetric grids were created by smoothing the *medium* domain size bathymetry (outlined in Section 2.2.2) using a 1.5 km, 5.5 km and 15 km square mean filter. The first value (1.5 km) was chosen as this is just below the resolution of the GEBCO 30 arcsecond bathymetry, smoothing using this filter therefore results in bathymetry where less of the topographic variability and roughness within the canyon is resolved than in the 500 m bathymetric grid. The second value (5.5 km) was chosen as this is greater than the width of most of the upper canyon limbs, hence, smoothing using this filter results in bathymetry that still resolves the major canyon limbs. The dominant features in the 500-m resolution bathymetry (Figure 5.1 (a)) are retained in both the 1.5-km and 5-km bathymetries; the individual limbs of Whittard Canyon can be identified. In the 15-km smoothed bathymetry, however, the individual limbs cannot be identified (Figure 5.1 (b)). The final value (15 km) therefore results in bathymetry that begins to resemble an idealised shelf profile with no canyon incising it, and so begins to demonstrate how different the internal wave field around the shelf edge would be without a canyon. The resulting bathymetries are named after the square mean filter used to smooth them, hence, in this chapter the *medium* model run is referred to as the 500-m bathymetry and the other bathymetries as the 1.5-km, 5.5-km and 15-km bathymetries.

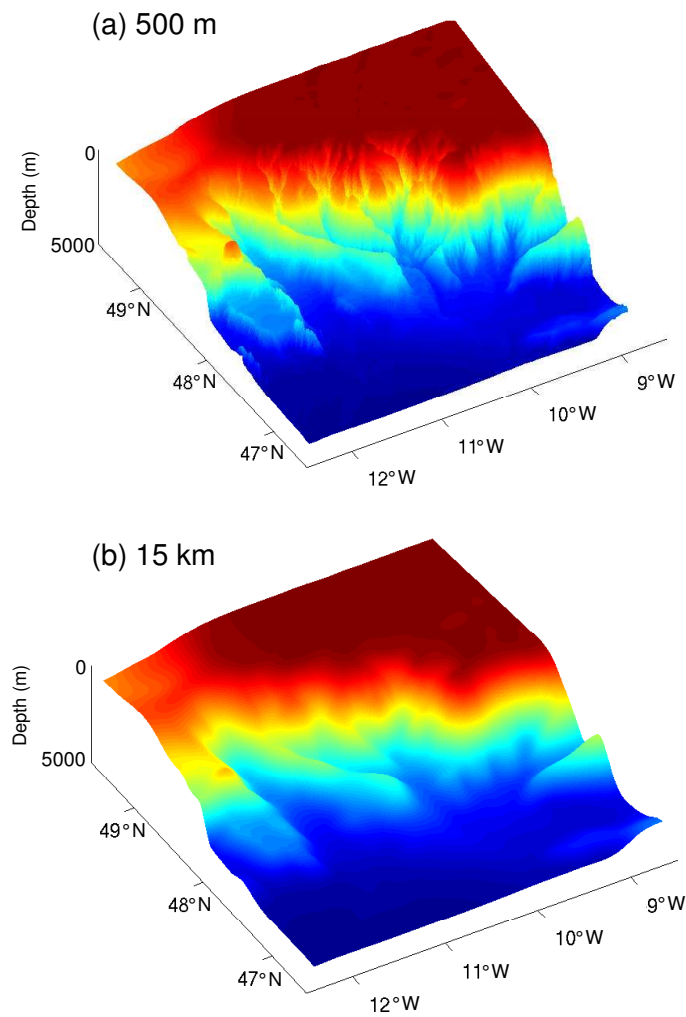


**Figure 5.1:** The model bathymetries used in the (a) 500 m and (b) 15 km runs.

It is difficult to visually identify the more subtle differences between the bathymetries using 3D plots, therefore to quantify the differences, the topographic height and slope spectra <sup>1</sup> for the different bathymetries are computed as per the method of Zilberman et al. (2009). The spectra are functions of  $(\kappa, \phi)$ , where  $\mathbf{k} = (k, l) = \kappa (\cos \phi, \sin \phi)$  is the horizontal wavenumber, integrated over  $\phi$  (Figure 5.2).

The topographic height spectra for all bathymetries are similar over the scale range corresponding to internal modes 1 to 3 ( $0.5 \times 10^{-4} \text{ rad m}^{-1}$  and 116.4 km to  $1.6 \times 10^{-4} \text{ rad m}^{-1}$  and 39.3 km). Beyond this range, the 5.5-km bathymetry is different to the other bathymetries over scales corresponding to internal modes 5 ( $2.7 \times 10^{-4}$  and

<sup>1</sup>The 2D power spectrum is radially averaged

23.3 km) and above. The topographic spectra for the 500-m and 1.5-km bathymetries are very similar, only exhibiting differences over scales corresponding to internal modes 20 ( $1.1 \times 10^{-3}$  and 5.7 km) and above. The topographic slope spectra for the 500-m and 1.5-km runs are also very similar, only differing over scales corresponding to internal modes 30 ( $1.6 \times 10^{-3}$  and 3.9 km) and above. The topographic slope spectra for the 1.5-km and 5.5-km bathymetries differ from the 500-m and 1.5-km bathymetries spectra over all scales.

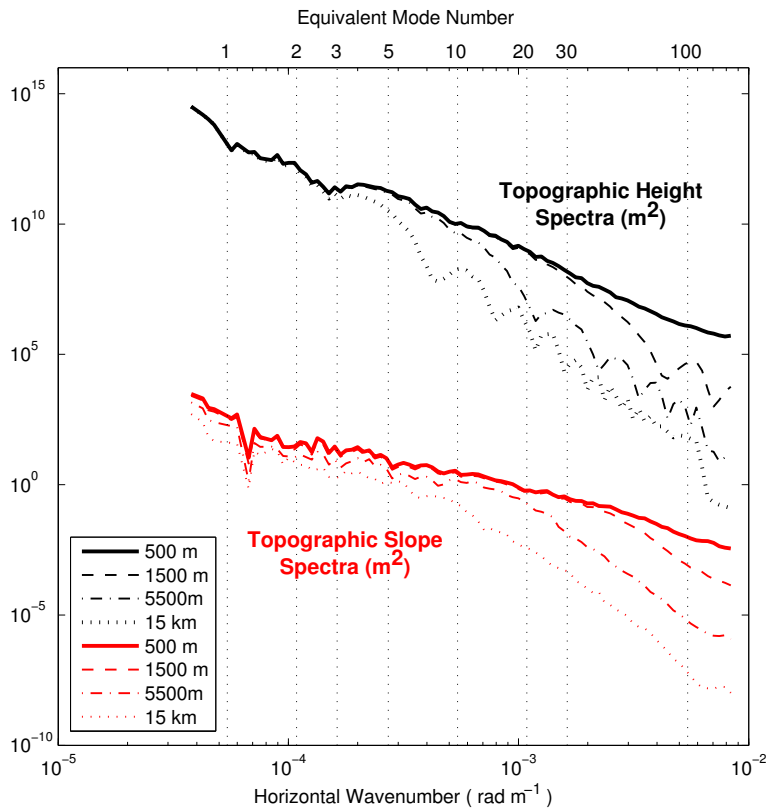


**Figure 5.2:** Topographic height and slope spectra for the 500 m, 1500 m, 5500 m and 15 km bathymetries. The equivalent internal mode wavenumbers are shown for reference.

### 5.2.1 CRITICALITY

Smoothing bathymetry is likely to change the reflection behaviour of internal waves, due to the behaviour's dependence on topographic slope amplitude (Equation 4.1, Section 4.3.4). The reflection behaviour of an internal wave encountering bathymetry, characterised by the ratio  $\alpha$ , is shown for all four model runs (Figure 5.3). As expected, due to the steep nature of canyon walls, much of the upper reaches of Whittard Canyon in the 500-m run are supercritical with respect to the  $M_2$  internal tide,

whereas the abyssal plain, shelf and thalwegs of the lower reaches of the canyon (where they are U-shaped) are subcritical. With smoothing, the area of the domain that is supercritical decreases, as does the maximum value of  $\alpha$ . The 1.5-km run is broadly similar to the 500-m run, however a significant difference arises in the 5.5-km run; the head of the canyons are no longer supercritical. Instead the entire length of the thalweg, from canyon mouth to head is subcritical with respect to the  $M_2$  internal tide. The pattern of  $\alpha$  in the 15-km run bears little resemblance to the original pattern in the 500-m run, however, the region to the west of Brenot Spur is still supercritical with respect to the  $M_2$  internal tide.

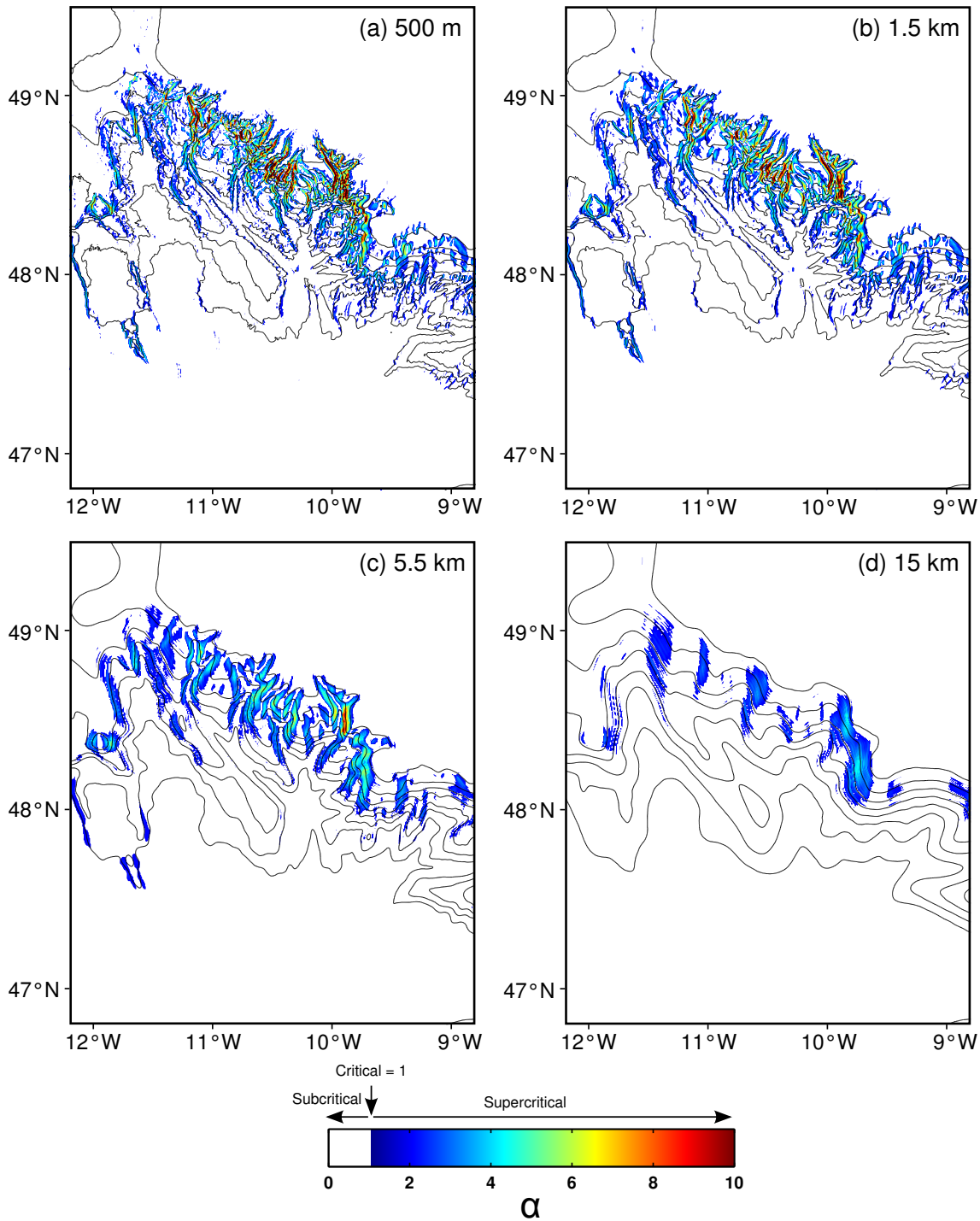


**Figure 5.3:** Maps of  $\alpha$  for the (a) 0.5 km gridded bathymetry (b) bathymetry smoothed with a 5.5 km mean filter. Depth contours are plotted every 500 m.

Smoothing the bathymetry increases the percentage of the domain that is subcritical and decreases the percentage of the domain that is supercritical (Table 5.1), however the percentage of the domain that is near-critical (defined as

$0.8 < \alpha < 1.3$ ) remains fairly constant. The mean supercritical value is similar for the 500-m and 1.5-km model runs (2.8 and 2.7, respectively), however, with increased smoothing, this drops to 1.6 for the 15-km case. Similarly, the maximum supercritical value decreases significantly from 18.2 in the 500-m run to 4.5 in the 15-km runs.

	<i>Subcritical</i> $\alpha < 0.8$	<i>Near-critical</i> $0.8 < \alpha < 1.3$	<i>Supercritical</i> $\alpha > 1.3$	<i>Mean</i> <i>supercritical</i> <i>value</i>	<i>Maximum</i> <i>supercritical</i> <i>value</i>
<b>500-m</b>	85.5 %	5.5 %	9.0 %	2.8	18.2
<b>1.5-km</b>	86.5 %	5.4 %	8.1 %	2.7	14.0
<b>5.5-km</b>	89.6 %	5.2 %	5.2 %	2.1	10.0
<b>15-km</b>	94.7 %	3.4 %	1.9 %	1.6	4.5

**Table 5.1:** Percentage of domain that is sub-critical, near-critical (defined as  $0.9 < \alpha < 1.1$ ) and supercritical for the 0.5 km, 1.5 km and 5.5 km model.

## 5.3 MODELLING RESULTS

All model runs use a similar setup to the control run as defined in Chapter 2 i.e. 32 tidal cycles, *summer* stratification and the medium domain size, but with different bathymetries, namely the 500-m, 1.5-km, 5.5-km and 15-km grids.

### 5.3.1 BAROTROPIC-TO-BAROCLINIC ENERGY CONVERSION

The spatial pattern of barotropic-to-baroclinic energy conversion is similar for the 500-m and 1.5-km model runs (Figures 5.4 (a,b)) but with reduced amplitude in the 1.5-km case. With increased smoothing, the amplitudes of conversion are further reduced and regions of positive conversion in the 500-m and 1.5-km runs, namely conversion in Limbs 1 and 3, are absent in both the 5.5-km and 15-km runs (Figures 5.4 (c,d)). The spatial pattern of barotropic-to-baroclinic energy conversion closely mirrors the distribution of supercritical regions for each model run, as shown in Figure 5.3. The main positive conversion sites within Whittard Canyon are localised over the steep flanks of the canyon limbs. Positive energy conversion in Shamrock Canyon and the region to the east of Whittard Canyon is a persistent feature of all model runs, further confirming the findings of Chapter 4 that this region is an important source of baroclinic energy within this area. Negative conversion is also

reduced in both the 5.5-km and 15-km runs in comparison to the higher resolution runs. Negative energy conversion originates from the phase difference between remote and locally generated internal tides (Zilberman et al., 2009; Kelly and Nash, 2010), hence a reduction in negative conversion perhaps indicates that smoothing of the bathymetry results in the reduction of local generation sites in the limbs of the canyon.

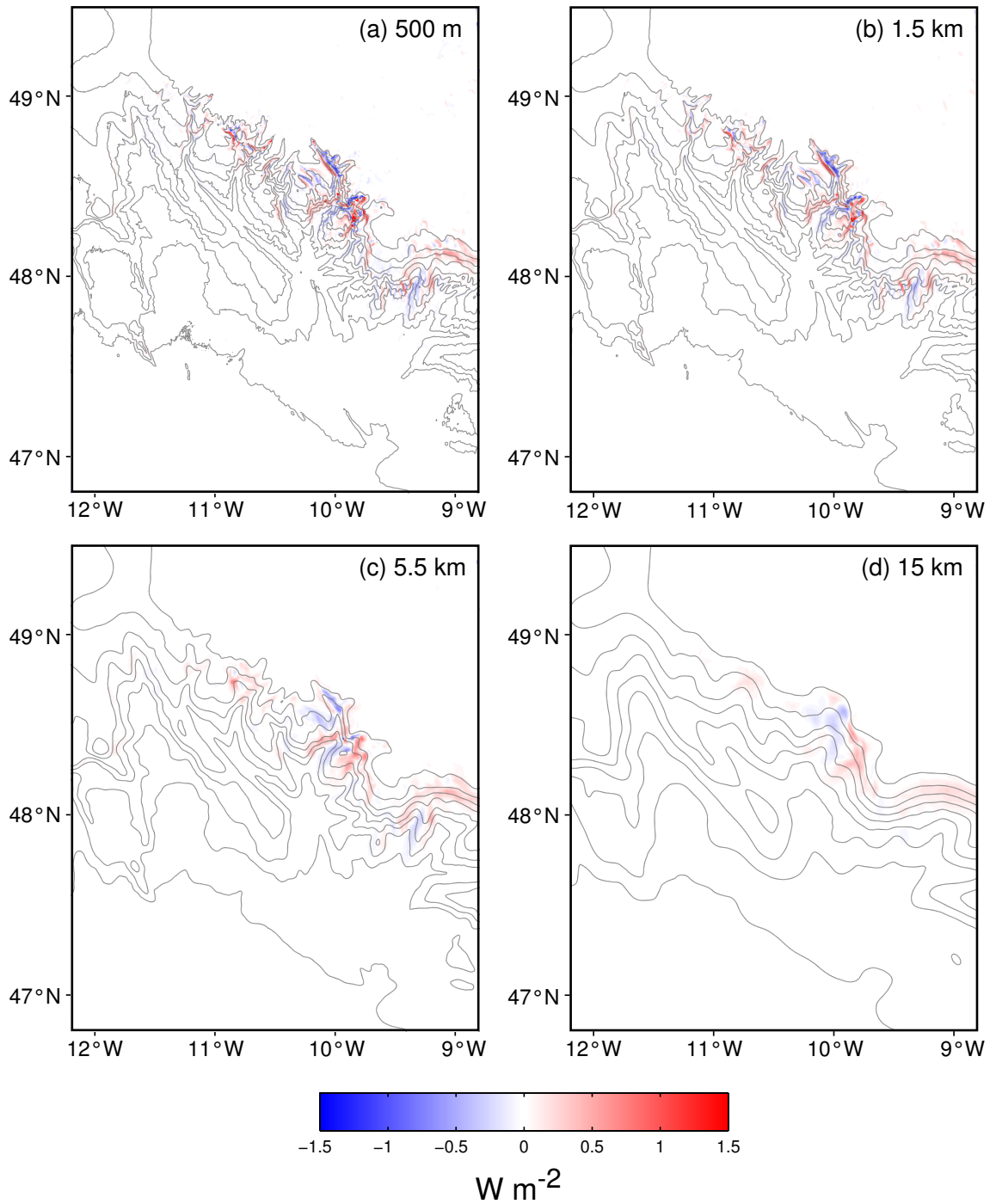


**Figure 5.4:**  $M_2$  barotropic-to-baroclinic energy conversion,  $E_{conv}$ , for the (a) 500-m, (b) 1.5-km, (c) 5.5-km and (d) 15-km model runs. Depth contours are plotted every 500 m.

Domain averaged and domain integrated barotropic-to-baroclinic energy conversion decrease with smoothing from  $7.9 mW m^{-1}$  and 0.66 GW, respectively, in the 500-m run to  $4.4 mW m^{-1}$  and 0.37 GW, respectively, in the 15-km run (Table 5.2). Domain-averaged conversion in the 500-m model run is 9.3%, 22.2% and 78.4%

higher than that for the 1.5-km, 5.5-km and 15-km runs. The total amount of conversion occurring in the Shamrock Canyon region, however, stays fairly consistent despite smoothing (0.17 GW in the 500-m run to 0.14 GW in the 5-km run). Once again, the conversion in the 500-m and 1.5-km runs is broadly similar; over the Whittard Canyon region the area-integrated conversion for the 500-m and 1.5-km runs are 0.32 and 0.31 GW, respectively.

Model run	Region	Area-integrated	Area-averaged
		$E_{conv}$ (GW)	$E_{conv}$ ( $\text{mWm}^{-2}$ )
500 m	Entire domain	0.66	7.9
	Whittard Canyon	<b>0.32</b>	<b>14.2</b>
	Shamrock Canyon	0.17	33.5
1.5 km	Entire domain	0.63	7.5
	Whittard Canyon	<b>0.31</b>	<b>13.5</b>
	Shamrock Canyon (partial)	0.17	33.5
5.5 km	Entire domain	0.54	6.5
	Whittard Canyon	<b>0.26</b>	<b>11.3</b>
	Shamrock Canyon	0.17	32.9
15 km	Entire domain	0.37	4.4
	Whittard Canyon	<b>0.16</b>	<b>7.0</b>
	Shamrock Canyon	0.14	27.5

**Table 5.2:** Area-integrated and area-averaged barotropic-to-baroclinic energy conversion for the 500-m, 1.5-km, 5.5-km and 15-km model runs for each entire domain, and within each domain, the Whittard Canyon region and the Shamrock Canyon region.

### 5.3.2 BAROCLINIC ENERGY FLUX

The spatial patterns of depth-integrated baroclinic energy flux for all model runs are surprisingly similar on a broad scale (Figure 5.5), given the significant differences observed in baroclinic energy conversion (Figure 5.4). All model runs show a beam of baroclinic energy flux propagating southwest from Shamrock Canyon, and another beam propagating northwest along the western flanks of Brenot Spur and into *Limb4*. The spatial patterns in the 500-m and 1.5-km runs on a finer scale, however, are more complex, with the orientations of baroclinic energy flux vectors being more variable. With increased smoothing, baroclinic energy flux is more or less absent from the western part of Whittard Canyon in the 1.5-km and 15-km model runs. However, the maximum baroclinic energy flux magnitudes increase with smoothing; the largest

fluxes are found in the 15-km run, reaching values  $>10 \text{ kW m}^{-1}$  over *Limb4*.

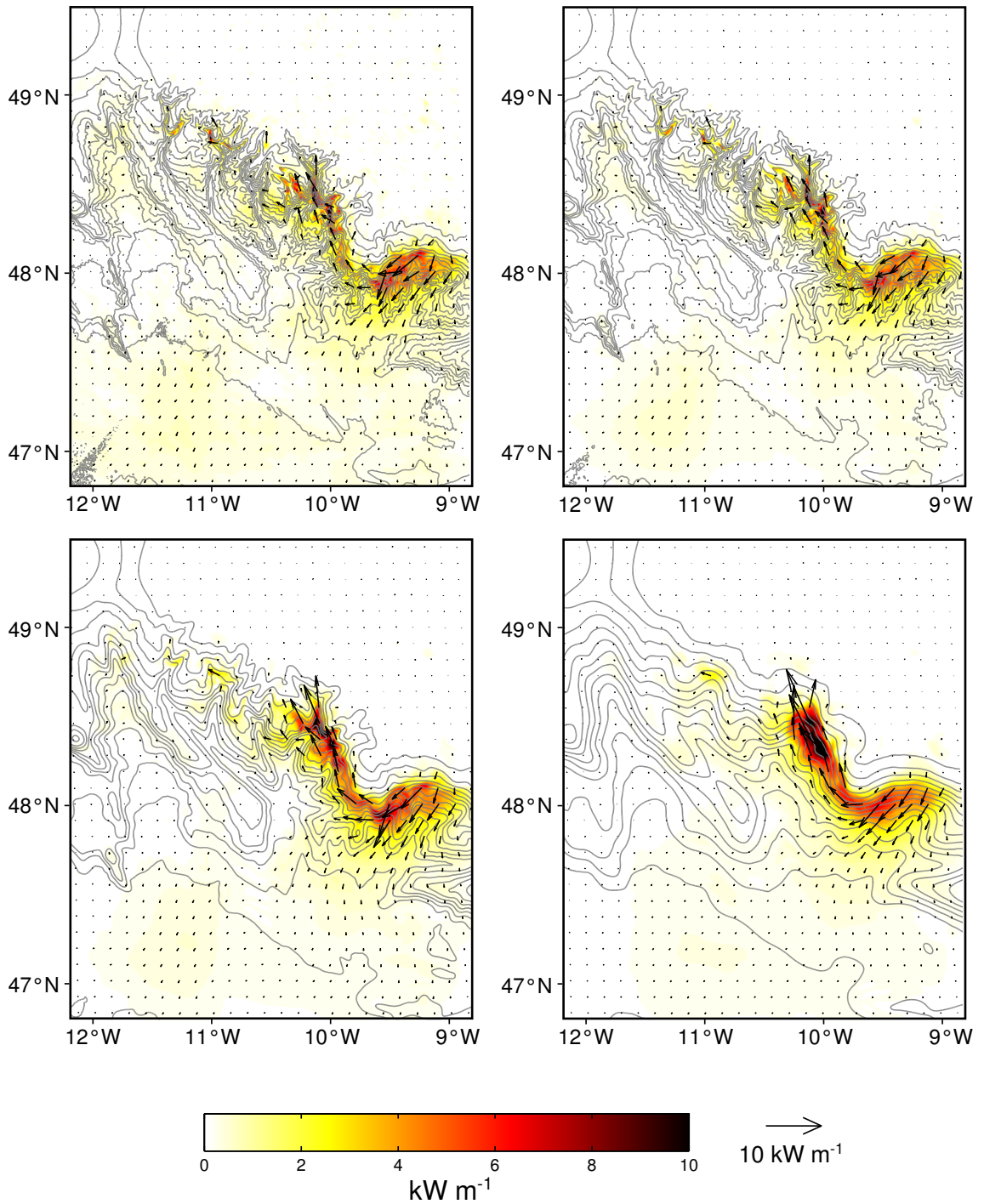


**Figure 5.5:** Depth-integrated baroclinic  $M_2$  energy flux for the (a) 500-m, (b) 1.5-km, (c) 5.5-km and (d) 15-km model runs. Vectors are plotted every 40 model grid points ( $\approx 20 \text{ km}$ ) in each direction. The underlying colour is the energy flux magnitude. Depth contours are plotted every 300 m.

Both domain integrated and domain averaged baroclinic flux divergence decrease

with smoothing (Table 5.3). However, when individual regions are looked at, this is not the case. Smoothing the bathymetry appears to increase the area-integrated baroclinic flux divergence over Shamrock Canyon, from 0.13 GW in the 500-m run to 0.16 GW in the 5.5-km run. In the 15-km run, it decreases back down to 0.14 GW. Over the Whittard Canyon, the pattern is the opposite; smoothing the bathymetry appears to decrease the area-integrated baroclinic flux divergence over Whittard Canyon, from -0.05 GW in the 500-m run to -0.07 GW in the 5.5-km run. In the 15-km run, it increases back up to -0.06 GW. The percentage of the converted barotropic-to-baroclinic energy that is radiated out of the domain increases with smoothing: 16.4%, 17.1% and 20.3% in the 500 m, 1.5 km and 5.5 km runs, respectively. However, the percentage of the total barotropic-to-baroclinic energy conversion within the domain that is converging on the Whittard Canyon region increases with smoothing, 5.5%, 5.7% and 9.4% in the 500 m, 1.5 km and 5.5 km runs, respectively.

Model run	Region	Area-integrated	Area-averaged
		$\nabla \cdot \mathbf{F}$ (GW)	$\nabla \cdot \mathbf{F}$ (mWm <sup>-2</sup> )
500 m	Entire domain	0.14	1.70
	Whittard Canyon	<b>-0.05</b>	<b>-2.20</b>
	Shamrock Canyon	0.13	25.7
1.5 km	Entire domain	0.12	1.50
	Whittard Canyon	<b>-0.06</b>	<b>-2.50</b>
	Shamrock Canyon (partial)	0.13	26.4
5.5 km	Entire domain	0.13	1.50
	Whittard Canyon	<b>-0.07</b>	<b>-3.20</b>
	Shamrock Canyon	0.16	30.9
15 km	Entire domain	0.10	1.20
	Whittard Canyon	<b>-0.06</b>	<b>-2.50</b>
	Shamrock Canyon	0.14	27.2

**Table 5.3:** Area-integrated and area-averaged baroclinic energy flux in the 500-m, 1.5-km, 5.5-km and 15-km model runs for each entire domain, and within each domain, the Whittard Canyon region and the Shamrock Canyon region (only *wc03* contains this complete region).

### 5.3.3 BAROCLINIC ENERGY DISSIPATION

Assuming that all net energy (net baroclinic-to-barotropic energy conversion minus baroclinic energy flux divergence) into each region is dissipated, baroclinic energy dissipation can be calculated. Inferred dissipation for the entire domain in each model run decreases with smoothing, from 0.52 GW in the 500-m run to 0.27 GW in the 15-km run (Table 5.4). Baroclinic dissipation within the Whittard Canyon region accounts for most of the dissipation in each model run. Furthermore, the percentage of total dissipation that the Whittard Canyon accounts for increases with smoothing, from 71.1% in the 500-m run, to 81.5% in the 15-km run. In contrast, baroclinic dissipation within Shamrock Canyon is small and the percentage of total dissipation that it accounts for decreases with smoothing (7.7%, 7.8%, 2.4% and 0.5% of total dissipation in the 500-m, 1.5-km, 5.5-km and 15-km runs, respectively).

<b>Model run</b>	<b>Region</b>	<b>Total dissipation (GW)</b>
<i>500 m</i>	Entire domain	0.52
	Whittard Canyon	<b>0.37</b>
	Shamrock Canyon	0.04
<i>1.5 km</i>	Entire domain	0.51
	Whittard Canyon	<b>0.37</b>
	Shamrock Canyon (partial)	0.04
<i>5.5 km</i>	Entire domain	0.41
	Whittard Canyon	<b>0.33</b>
	Shamrock Canyon	0.01
<i>15 km</i>	Entire domain	0.27
	Whittard Canyon	<b>0.22</b>
	Shamrock Canyon	0.00

**Table 5.4:** Inferred dissipation in the 500-m, 1.5-km, 5.5-km and 15-km model runs for each entire domain, and within each domain, the Whittard Canyon region and the Shamrock Canyon region (only *wc03* contains this complete region).

## 5.4 DISCUSSION AND CONCLUSIONS

The barotropic-to-baroclinic energy conversion estimates calculated here for model runs using differing resolutions of bathymetry highlight the importance of using the highest resolution bathymetry available. Using a 500-m gridded bathymetric dataset results in domain-averaged conversion rates that are 5.3%, 21.5% and 79.5% higher than model estimates using the 1.5-, 5- and 15 km smoothed bathymetries, respectively. Similar reductions in conversion with decreasing topographic resolution have been calculated when assessing tidal conversion at the Hawaiian islands (Carter et al., 2008) and at the Mid-Atlantic Ridge (Zilberman et al., 2009).

The main conversion sites in Whittard Canyon are located at near-critical and supercritical sites. Smoothing the bathymetry not only decreases the proportion of slopes which are supercritical, but also decreases the maximum value of supercritical slope observed. Hall et al. (2013) found that partially supercritical slopes reflected a similar proportion of internal wave energy as entirely supercritical slopes, and that the fraction reflected was dependent only on maximum slope criticality. The smoothed bathymetry is therefore likely to underestimate generation and also not accurately model the reflective behaviour of internal tides within this region.

The bathymetric resolution used also affects the ratio of baroclinic energy that is radiated versus local dissipation. The ratio of converted energy that is dissipated within the domain is 78.8 %, 81.0 %, 75.9 % and 70.3 % in the 500-, 1.5-, 5- and 15-km model runs. bathymetries. We hypothesise that as the roughness of the topography is resolved, increased topographic scattering from low to high modes occurs (e.g. Müller and Xu, 1992) The small vertical wavelengths and high shear of high mode internal tides make them more susceptible to mixing than their low mode counterparts (St. Laurent and Garrett, 2002), resulting in increased dissipation within the domain. To confirm this hypothesis it would be pertinent to follow the method of Zilberman et al. (2009) and analyse the modal structure of conversion and dissipation within the region. Figure 5.2 certainly indicates that with increased smoothing there is less variability of the topographic height and slope over spatial scales where scattering of low mode number internal waves are present. Bell (1975, 1974) state that tidal flow over high horizontal wavenumber vertical topography generates high wavenumber internal tides. Therefore, if high horizontal wavenumber bathymetry is not resolved

in the smoothed model runs then the modal structure of conversion will also differ.

It may not be intuitive to non-modellers that in fact, high resolution bathymetry can also be a hindrance. As shown in Chapter 4, the complex bathymetry results in correspondingly complex patterns of local and remote generation (Section 4.2), reflection of internal waves (Section 4.3.4) and feedback between conversion and flux (Section 4.6.1), resulting in an internal tide field that is not easy to decipher. Using lower resolution bathymetry results in simplified bathymetry that approaches the idealised modelling approach (e.g. Petrucio et al., 2002; Zhang et al., 2014) whereby, due to the limited number of parameters and simplified scenarios, processes can be elucidated more clearly. For example, depth-integrated baroclinic energy flux in the model run with the most smoothed bathymetry (Figure 5.5 (d)) shows that Shamrock Canyon and Brenot Spur are key generation sites without noise from baroclinic flux originating from conversion elsewhere in the canyon. This model run would therefore be a good starting point to analyse to unpick exactly why this region is such an effective generator of internal tides.

Obtaining high quality and complete high resolution bathymetric datasets can be difficult due to the onerous nature of data collection, leading to a reliance on global products. As discussed in Chapter 2, there was an incomplete high resolution (500 m) bathymetric dataset that had to be completed using the GEBCO 30-arcsecond grid, leading to artefacts. If accurate estimates of barotropic-to-baroclinic conversion are required, however, high resolution datasets are needed. To this end, we recommend that although the 1.5-km model is similar to the 500-m model run, for the purposes of understanding the 3D structure in the canyon, the bathymetric resolution needs to be as high as possible. However, if a larger domain size was needed, for example, to diagnose far field generation, it would be reasonable to use the 1.5-km model bathymetry to reduce the computational expense of running the model. In conclusion, the choice of bathymetric resolution to be used in oceanographic simulations requires a degree of pragmatism.



# 6

## INTERNAL TIDE LAYERS FOR PREDICTIVE HABITAT MODELS

### 6.1 INTRODUCTION

Submarine canyons are often termed 'biodiversity hotspots' (De Leo et al., 2010) and it is thought that oceanographic processes within canyons, such as internal tides, can contribute to habitat heterogeneity and hence modulate biological abundance and diversity. One way of testing whether internal tides are a control on habitats is to carry out an observational programme where data on both the biology and oceanography are collected simultaneously and then relationships inferred, however, this is time intensive and expensive. Within Whittard Canyon, Robert et al. (2015) have used predictive habitat models (PHMs) to link spatial variation in observed biological characteristics with bathymetry-derived environmental variables (e.g., slope, depth, aspect and roughness), however, they suggest that the addition of hydrodynamic variables related to internal tides may reduce the amount of unexplained variation and help to start identifying what specific processes cause the internal tide to modulate biology within the canyon.

In this chapter we discuss what variables can be extracted from POM and how they can be adapted to be used in PHMs, specifically looking at isopycnal displacement as an example. The resulting layers can then be utilised within PHMs developed and

described in Robert et al. (2015) so that the impact of internal tides on habitats within Whittard Canyon can be assessed. All layers produced use the control model setup as defined in Chapter 2 i.e. 32 tidal cycles, *summer* stratification and the *medium* domain size.

## 6.2 PRELIMINARY RESULTS

To determine whether incorporating modelled output was feasible, a layer consisting of a ‘snapshot’ of the modelled near-bottom velocity was produced. By ‘snapshot’, we mean the magnitude and direction of velocity at an arbitrary point of time. The layer produced combined both the baroclinic ( $M_2$  internal tide) and barotropic (surface tide) components of near-bottom velocity. This layer was then included within a PHM<sup>1</sup> of Whittard Canyon. The preliminary results suggest that the inclusion of tidal near-bottom velocities can help improve the model’s skill in predicting megafaunal abundance, species richness and diversity (Figure 6.1). Although the results are promising, they do not specifically test the impact of the internal tide on habitats solely, nor, as a simple snapshot, does the layer robustly represent the temporal variability of internal tides within the region.

---

<sup>1</sup>Predictive habitat modelling work carried out by Kathleen Robert (NOC)

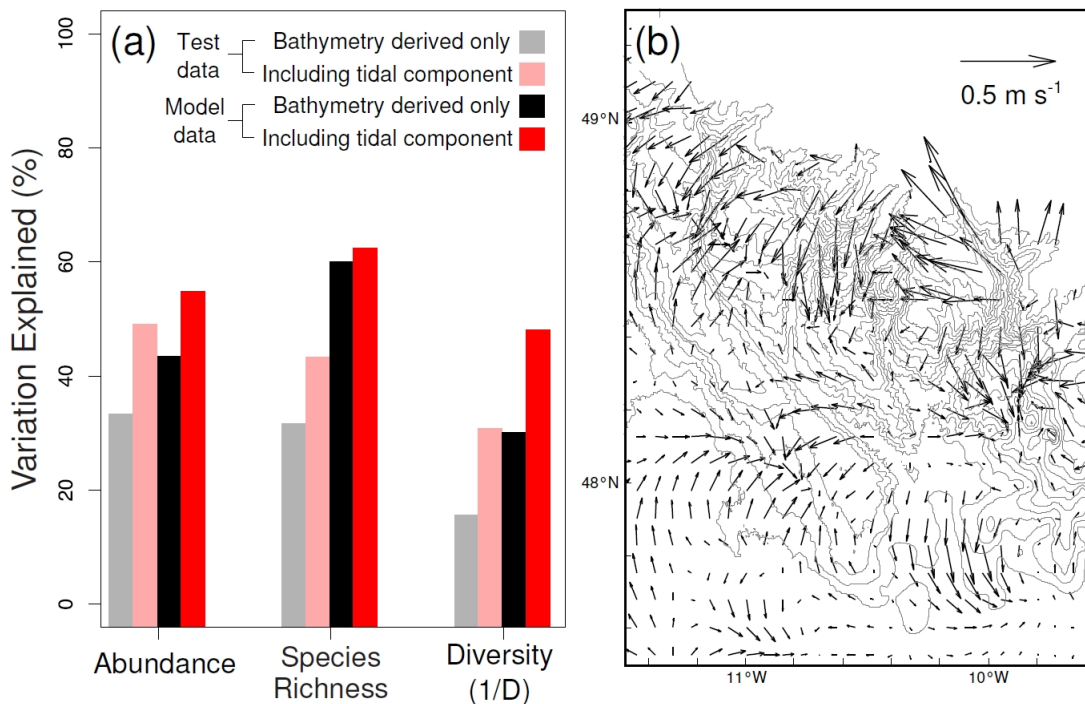


**Figure 6.1:** (a) Improvement in PHM performance through the inclusion of modelled near-bottom velocity as shown in (b). (b) Snapshot of modelled near-bottom velocity (barotropic plus baroclinic) used as a layer in the PHM. Vectors are plotted every 15 model grid points (7.5 km) and vectors shallower than 300 m are omitted for clarity. Depth contours are plotted every 300 m.

### 6.3 HYDRODYNAMIC VARIABLES SELECTION

Data for all variables to be used are taken from the near-bottom layer of the three-dimensional model, an approximation of the benthic boundary layer. The variables include:

- Horizontal flow parameters i.e. current speed and direction for both the barotropic and baroclinic components of velocity
- Vertical flow parameters, including the resulting barotropic and baroclinic isopycnal displacements (See Section 6.4)
- Variability in temperature and salinity derived from isopycnal displacements (See Section 6.4)
- Criticality,  $\alpha$  i.e the ratio of the topographic slope to the internal wave

characteristic slope as defined in Section 4.3.4

- Internal wave specific diagnostics i.e. baroclinic energy flux, barotropic-to-baroclinic energy conversion, HKE and APE as defined in Section 2.2.3

The dynamical scaling parameters and criticality require no further processing to be usable by PHMs as they are not time varying. POM, as described in Section 2.2.3, applies harmonic fits to the model and outputs amplitudes and phases. This is necessary as it would be too computationally expensive to output the raw values. For the purpose of producing layers, the maximum amplitude is therefore used.

## 6.4 ISOPYCNAL DISPLACEMENT

Creating a layer which captured isopycnal displacement caused by both the internal and surface tide is more involved than some of the other variables. However it was important to create such a layer as isopycnal displacements can advect the local stratification introducing variability in other parameters.

### 6.4.1 BAROTROPIC ISOPYCNAL DISPLACEMENT

The barotropic vertical velocity at the sea floor bottom,  $w_{Bt}$ , is caused by barotropic flow across sloping topography (Niwa and Hibiya, 2001; Zilberman et al., 2009), and is given by

$$w_{Bt} = -\mathbf{u}'_{Bt} \cdot \nabla H \quad (6.1)$$

where  $\mathbf{u}'_{Bt}$  is the depth-averaged horizontal velocity from the harmonic output of the model (Equation (2.5)) and  $H$  is the water depth (Garrett and Kunze, 2007). The associated isopycnal displacement can then be calculated using

$$[\xi_{BT_r}, \xi_{BT_i}] = [-w_{BT_i}, w_{BT_r}] / \omega \quad (6.2)$$

The resulting maps of barotropic isopycnal displacement amplitude and phase (Figure 6.2) show that barotropic isopycnal displacement is enhanced over the upper limbs of the canyon and is particularly high over Limb 4, with amplitudes up to 300 m being reached. The phase of barotropic isopycnal displacement phase is coherent,

but this should be expected as the barotropic forcing in the model doesn't vary much and is dependant on the topographic slope.

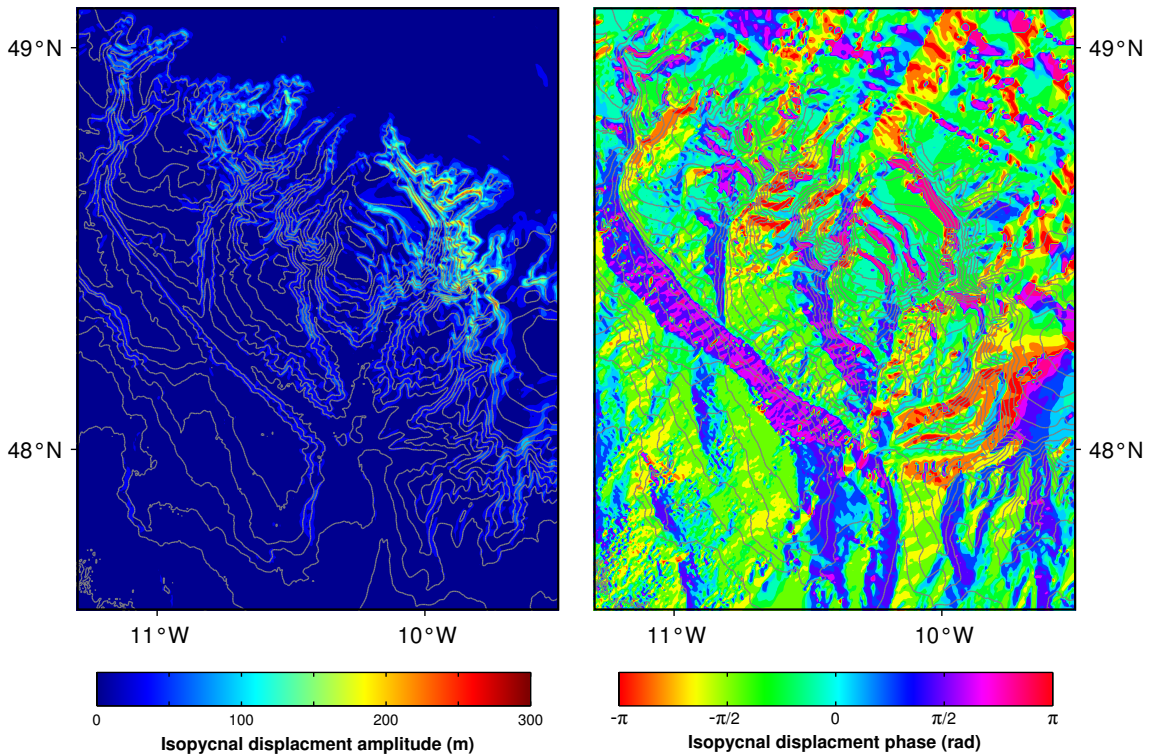


**Figure 6.2:** Barotropic isopycnal displacement amplitude (left) and phase (right). Contours are plotted every 300m

### 6.4.2 BAROCLINIC ISOPYCNAL DISPLACEMENT

Determining baroclinic isopycnal displacement in the model is not as simple as for the barotropic case. Using the baroclinic vertical velocity,  $w$ , at the sea floor bottom in the model to calculate isopycnal displacement is not possible as the model output for  $w$  goes to zero at the bathymetric boundaries. It is therefore not possible to calculate the baroclinic isopycnal displacement “seen” by a given point on the seafloor. Instead we consider what is happening around the point and use an algorithm to average the baroclinic vertical velocities in a horizontal plane around each point on the seafloor through the sigma-coordinate grid. For this purpose, we use two square mean filters: a  $3 \times 3$  grid point window (1 km) and a  $5 \times 5$  grid point window (2.5 km). The two square mean filters are used as the values for  $w$  at the boundaries next

to the bathymetry in the model are more suspect, hence by increasing the window over which values are averaged, we reduce the likelihood of erroneous values. The associated isopycnal displacement can then be calculated using

$$[\xi_{BC_r}, \xi_{BC_i}] = [-w_{BC_i}, w_{BC_r}] / \omega \quad (6.3)$$

The resulting maps of baroclinic isopycnal displacement amplitude and phase (Figure 6.3) have areas of missing data where the the average was taken around a point that is a topographic depression. The horizontal plane through the surrounding bathymetry therefore passes beneath the bathymetric grid's bottom boundary. The amount of missing data decreases with a larger square mean filter (Figure 6.3 (b)) as the average is calculated from more data points, so more of the horizontal plane being averaged over is likely to be above the bottom of the model's bathymetric grid.

Similar to barotropic isopycnal displacement, the baroclinic component is also enhanced over the upper limbs of the canyon, with amplitudes up to 300 m being reached. The phase of barotropic isopycnal displacement phase is incoherent (Figure 6.4), a product of the likely interaction between remotely and locally generated internal tides as discussed in Section 4.6.1.

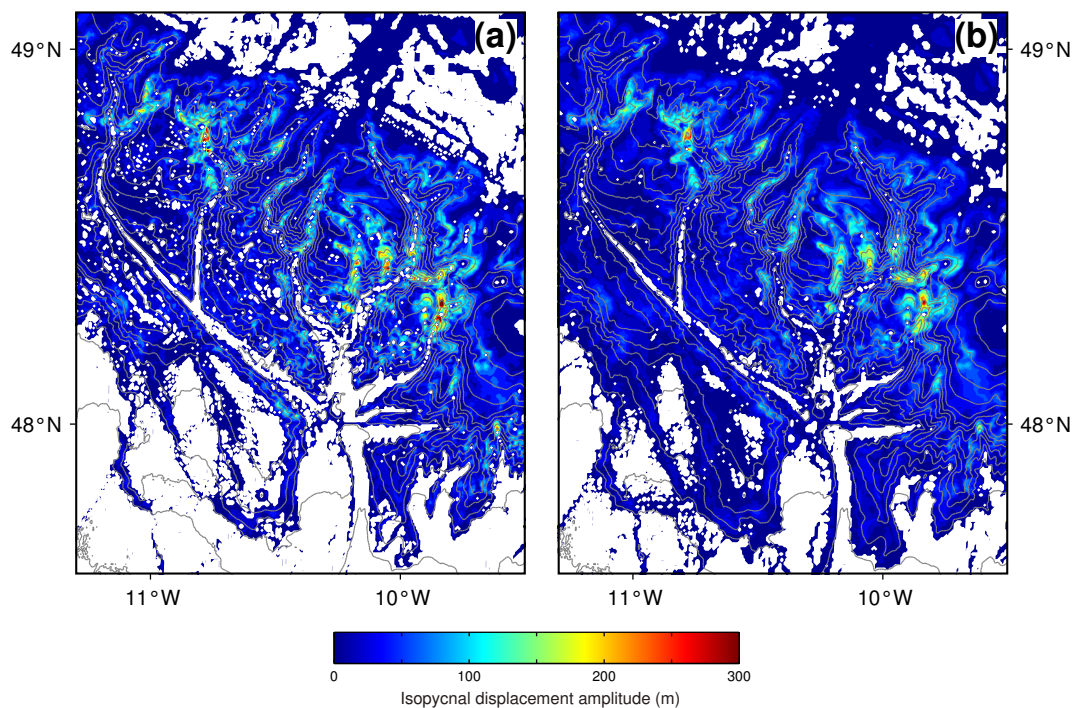


**Figure 6.3:** Baroclinic isopycnal displacement amplitude using (a) 1 km square average and (b) 2.5 km square average. Contours are plotted every 300 m.

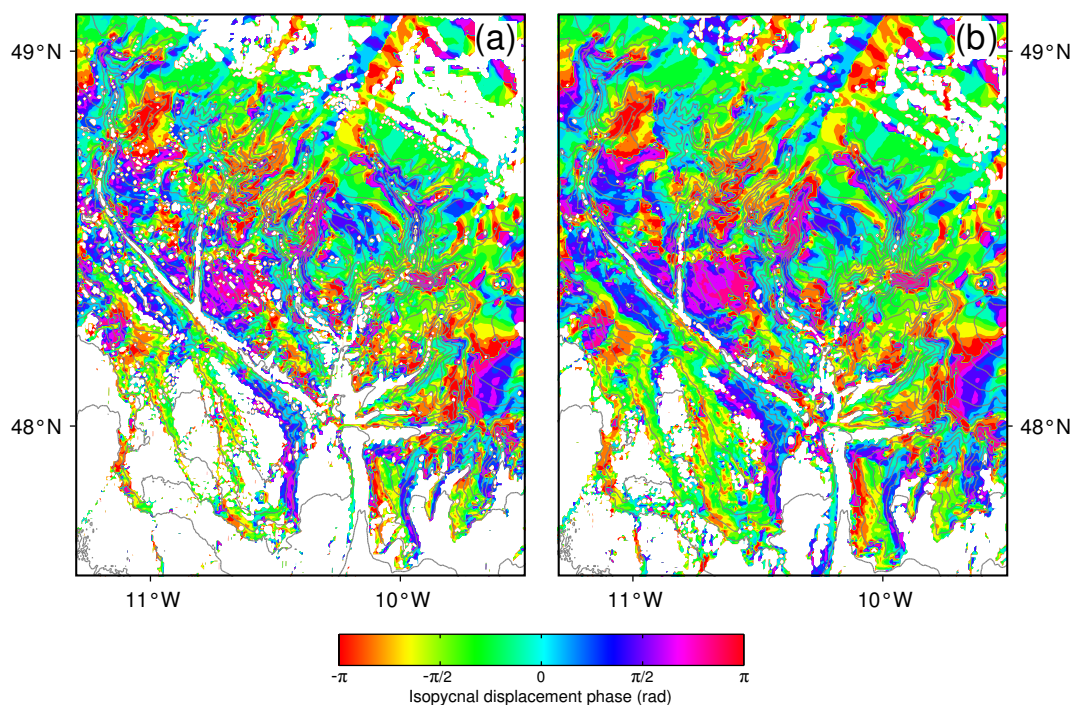


**Figure 6.4:** Baroclinic isopycnal displacement phase using (a) 1 km square average and (b) 2.5 km square average. Contours are plotted every 300 m.

### 6.4.3 TOTAL ISOPYCNAL DISPLACEMENT

Total isopycnal displacement due to both the barotropic and baroclinic tide can be calculated by summing the real and imaginary components of  $\zeta_{BT}$  and  $\zeta_{BC}$ . *Limb4* has been identified as being particularly energetic (Chapter 4) and hence the total isopycnal displacement amplitude is provided for this region for reference (Figure 6.5).

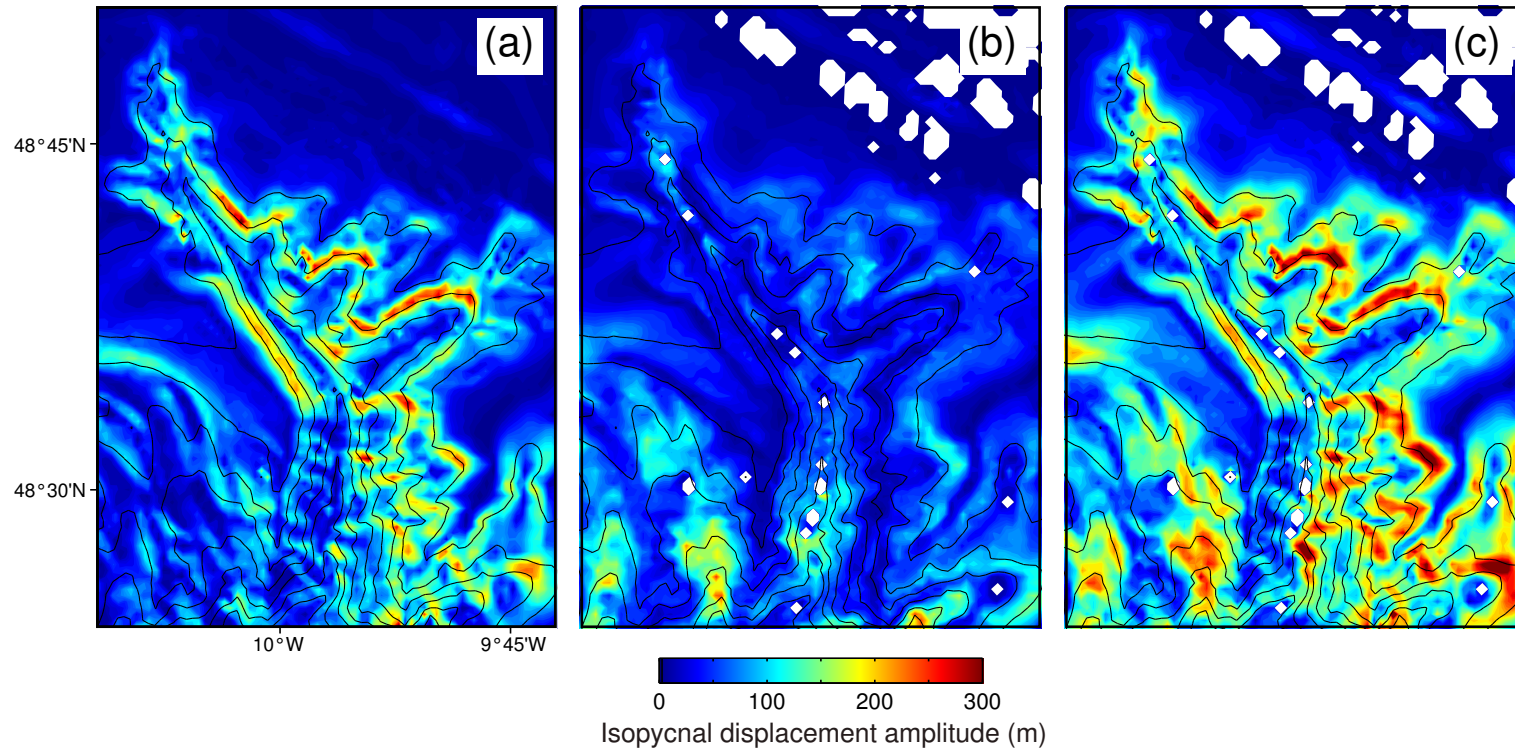


**Figure 6.5:** Isopycnal displacement amplitude in *Limb4* associated with: (a) the  $M_2$  surface tide ( $\zeta_{BT}$ ), (b) the  $M_2$  internal tide ( $\zeta_{BC}$ ) and (c) the two combined. Note that the total isopycnal displacement is a summation of the real and imaginary components of  $\zeta_{BT}$  and  $\zeta_{BC}$ .

Using this isopycnal displacement, and dissolved oxygen and temperature profiles collected using a Seaglider<sup>2</sup> (Figure 6.6 (c)), we calculate the variability in temperature and dissolved oxygen concentrations that benthic organisms on the canyon walls might encounter. The local gradients in temperature ( $\frac{dT}{dZ}$ ) and oxygen concentration ( $\frac{d(c(O_2))}{dZ}$ ) from the profiles are multiplied by the total isopycnal displacement,  $\zeta_{Total}$ , at each grid point to give the near-bottom temperature and oxygen concentration variability ( $T'$  and  $c(O_2)'$ , respectively):

$$T' = \zeta_{Total} \frac{dT}{dZ} \quad (6.4)$$

$$c(O_2)' = \zeta_{Total} \frac{d(c(O_2))}{dZ} \quad (6.5)$$

The maps of temperature and oxygen concentration variability (Figures 6.6 (a,b)) show that near-bottom temperature can vary by up to 3°C and near bottom oxygen concentration by up to 50  $\mu\text{mol/kg}$ . The temperature variability is highest around depths of 1000 m. This depth lies within the permanent thermocline i.e. the depth range where the vertical temperature (and density) gradients are largest. This strong vertical density gradient in combination with the steep continental slope at these depths leads to enhanced internal wave activity (White and Dorschel, 2010), resulting in large isopycnal displacements. The resulting isopycnal displacement then advects the high temperature gradients, leading to large variability. The peak in oxygen concentration variability occurs at shallower depths, corresponding to the where the gradient in oxygen concentration profile is largest.

<sup>2</sup>The Seaglider was equipped with a standard Sea-Bird Electronics conductivity-temperature-salinity sampling at 0.2 Hz and an Aanderaa 4330F dissolved oxygen optode (for further details of the deployment, see Chapter 3)

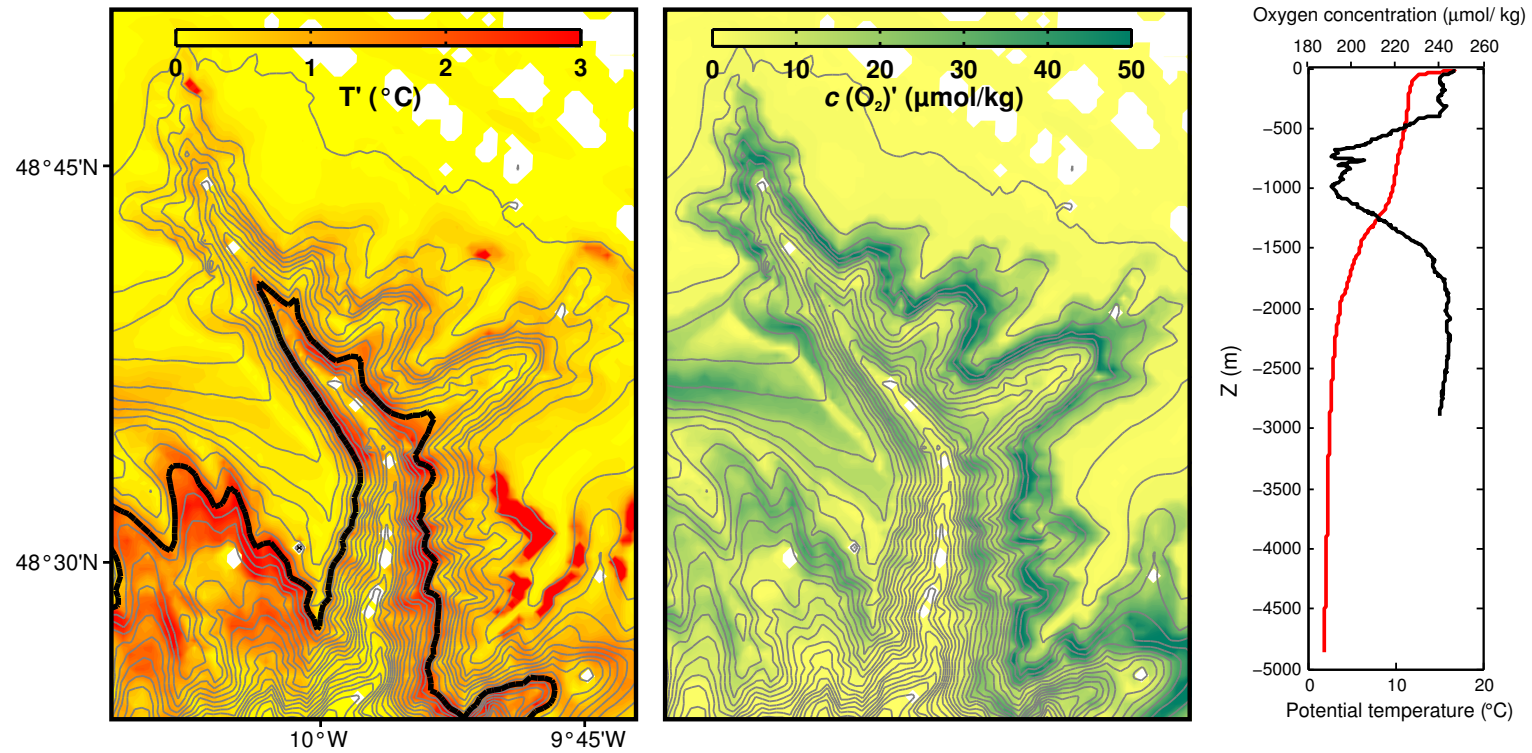


**Figure 6.6:** (a) Near-bottom temperature variability due to total (barotropic + baroclinic) modelled isopycnal displacement. The 1000 m isobath is indicated by the bold line. (b) Near-bottom oxygen variability due to total modelled isopycnal displacement. (c) Oxygen (black) and temperature (red) profiles used to calculate (a) and (b).

## 6.5 DISCUSSION AND CONCLUSIONS

The work presented here is a preliminary attempt looking at how information about the internal tide can be extracted from the current model and prepared for use in PHMs. As the internal tide is postulated to have a potentially large impact on biology, the need to incorporate hydrodynamic variables into predictive habitat models is prescient. The internal tide field within Whittard Canyon, as shown in Chapter 4, is highly spatially variable on a broad scale, with some limbs (limb 4), clearly more energetic than others. On a finer scale, there is also great variation within individual limbs (Section 4.3), however care must be taken as this local variation may in part be an artefact of flawed bathymetry and stratification that isn't representative of reality. As discussed by Wilson et al. (2015b), there is variability in stratification between limbs, however the model cannot capture this due to the use of a horizontally uniform stratification. In addition there were issues in the production of the bathymetric grid (Chapter 2) which may have led to artefacts. Despite the model using a fairly high bathymetric resolution for POM, it still is not sufficient to resolve many key features of the canyon such as vertical canyon walls. Also, as identified by the offset between the two data products used to create the bathymetric grid used here (Chapter 2), geolocation of the bathymetry datasets with real life may be an issue, and would have to be considered carefully. It is also important to note how coarse the resolution of the model's bathymetry is in relation to the resolution with which the occurrence of biological data can be collected using remotely operated vehicles (on the order of tens of centimetres).

The harmonic output of POM means that phase and amplitude of time-varying quantities are output, rendering time-averages across tidal cycles meaningless (they would average to 0), hence, the temporal variability of the internal tide cannot currently be captured in these layers. In addition, many of the layers produced are derived from parameters which in themselves can form layers. It is important therefore to test each layer individually to avoid double weighting the impact of any given parameter on habitats (e.g. Guisan and Zimmermann, 2000).

The maps of variability in temperature and oxygen concentration produced using isopycnal displacements extracted from the model show how the current model output can be used in combination with other data sources to provide potentially

useful layers. It is beyond the scope of this work to unpick what these specific values of variability would mean for biology within the canyon, however, the map of temperature variability is particularly interesting as it highlights the importance of the permanent thermocline within the region for both the concentration of internal tide energy and also potentially for biology (e.g. White and Dorschel, 2010). However, this method is limited by the use of a temperature and oxygen concentration profile from one limb extrapolated across the entire domain as a horizontally uniform field. In future, information on such parameters from across the canyon should be used to construct such maps of variability.

As discussed in Chapter 3, the absolute magnitudes of the different variables should be treated with caution. It should be made clear to interdisciplinary researchers using these layers that the results presented in this thesis are model output, and not reality. However on a canyon wide scale, the results presented in this work provide a first overview of the spatial variability of the internal tide within a complex canyon and the potential to improve the model skill of predictive habitat models and hence help to elucidate the bio-physical connections between the internal tide and biology.



# 7

## SUMMARY AND SYNTHESIS

This chapter provides a summary of all the key findings in this thesis and recommendations for future work.

### 7.1 SUMMARY

#### 7.1.1 MODEL SETUP

Accurately representing seafloor bathymetry is a vital part of any numerical modelling procedure to ensure that the internal tide field in the simulations are as close to reality as possible. A complete bathymetric dataset of the Whittard Canyon and surrounding area at the right resolution required for this work was not available, and therefore two data products were required to create one complete bathymetry input file. Combining GEBCO and INFOMAR data highlighted the difficulty of using products which may be geolocated differently, may have undergone different processing procedures and are of different resolutions.

The correct domain size is also important to identify. The right domain size must be selected so that all the key generation sites are present, however too large a domain size is computationally expensive. The results of domain size sensitivity testing indicate that a domain that only includes Whittard Canyon does not include all of the generation sites that contribute to the internal tide field in the canyon itself.

Shamrock Canyon is identified as a key generation site.

### **7.1.2 MODEL VALIDATION**

The errors calculated between the model and observations at first glance appear high, however previous work in Monterey Canyon by Carter (2010) using POM found similar RMS errors, ranging between 30% - 209%. The errors are reasonable when the shortcomings of the model and observations are considered. Bathymetric resolution is a key determinant of model skill, however increasing bathymetric resolution to sufficiently resolve the complex bathymetry encountered in Whittard Canyon is too computationally expensive and still would not be able to resolve features such as overhangs.

### **7.1.3 INTERNAL TIDES IN WHITTARD CANYON**

The internal tide within Whittard Canyon is spatially complex, however, through this work the key generation sites have been identified. Shamrock Canyon and the region to the west of Brenot Spur are key remote sources of baroclinic energy. Local generation also occurs within the canyon, but is modulated by a flux-conversion feedback that is dependant on the phase of the remotely generated internal waves. The results presented here highlight how important choosing the correct domain size is for barotropic-to-baroclinic conversion to be estimated accurately, as if key remote sources are omitted, even local generation is affected. The Bay of Biscay to the east of Whittard Canyon may be a source of farfield generation for Whittard Canyon, so it is advised that a much larger domain size be used to identify whether this is the case. Furthermore, internal tide barotropic-to-baroclinic conversion is also dependant upon bathymetry, therefore sufficiently high resolution topography is required to accurately estimate conversion.

The internal tide is enhanced throughout all limbs in the canyon, but variably so, relating to different remote sources of internal tides and differing reflection regimes. The propagation of the internal tide is dominantly up-slope and the corresponding baroclinic energy flux is bottom intensified along depths of 1000-2500 m which correlates with the position of the permanent thermocline within the region. The permanent thermocline associated with the MOW is likely to act as a waveguide for

freely propagating internal waves, focusing energy at the seabed (Puig and Palanques, 1998). This work provides confirmation that internal wave activity is enhanced over the region associated with the permanent thermocline, with implications for biology (Amaro et al., 2016) and the formation of nepheloid layers (Wilson et al. (2015b)).

#### **7.1.4 BATHYMETRIC RESOLUTION EFFECTS ON THE INTERNAL TIDE**

The barotropic-to-baroclinic energy conversion estimates calculated for model runs using differing resolutions of bathymetry highlight the importance of using the highest resolution bathymetry available. Using a 500-m gridded bathymetric dataset results in domain-averaged conversion rates that are 5.3%, 21.5% and 79.5% higher than model estimates using the 1.5-, 5- and 15 km smoothed bathymetries, respectively. Similar reductions in conversion with decreasing topographic resolution have been calculated when assessing tidal conversion at the Hawaiian islands (Carter et al., 2008) and at the Mid-Atlantic Ridge (Zilberman et al., 2009).

The bathymetric resolution used also affects the ratio of baroclinic energy that is radiated versus local dissipation. The ratio of converted energy that is dissipated within the domain is 78.8 %, 81.0 %, 75.9 % and 70.3 % in the 500-, 1.5-, 5- and 15-km model runs. bathymetries. We hypothesise that as the roughness of the topography is resolved, increased topographic scattering from low to high modes occurs (e.g. Müller and Xu, 1992) The small vertical wavelengths and high shear of high mode internal tides make them more susceptible to mixing than their low mode counterparts (St. Laurent and Garrett, 2002), resulting in increased dissipation within the domain. To confirm this hypothesis it would be pertinent to follow the method of Zilberman et al. (2009) and analyse the modal structure of conversion and dissipation within the region.

#### **7.1.5 INTERNAL TIDE LAYERS FOR PREDICTIVE HABITAT MODELS**

The harmonic output of POM means that phase and amplitude of time-varying quantities are output, rendering time-averages across tidal cycles meaningless (they would average to 0), hence, the temporal variability of the internal tide cannot currently be captured in these layers. In addition, many of the layers produced

are derived from parameters which in themselves can form layers. It is important therefore to test each layer individually to avoid double weighting the impact of any given parameter on habitats (e.g. Guisan and Zimmermann, 2000).

The maps of variability in temperature and oxygen concentration produced using isopycnal displacements extracted from the model show how the current model output can be used in combination with other data sources to provide potentially useful layers. It is beyond the scope of this work to unpick what these specific values of variability would mean for biology within the canyon, however, the map of temperature variability is particularly interesting as it highlights the importance of the permanent thermocline within the region for both the concentration of internal tide energy and also potentially for biology (e.g. White and Dorschel, 2010). However, this method is limited by the use of a temperature and oxygen concentration profile from one limb extrapolated across the entire domain as a horizontally uniform field. In future, information on such parameters from across the canyon should be used to construct such maps of variability.

## **7.2 SYNTHESIS**

### **7.2.1 IMPLICATIONS FOR NEPHELOID LAYER GENERATION**

As previously mentioned, many studies have linked the focusing of internal wave energy within submarine canyons to benthic resuspension and nepheloid layer formation (McPhee-Shaw and Kunze, 2002; MCPhee-Shaw et al., 2004; Thorpe and White, 1988). Within Whittard Canyon specifically, recent works (Wilson et al., 2015b; Huvenne et al., 2011; Johnson et al., 2013) have extensively mapped both bottom and intermediate nepheloid layers and postulated that the internal tide within the canyon is major control on their formation. The permanent thermocline associated with the MOW is likely to act as a waveguide for freely propagating internal waves, focusing energy at the seabed (Puig and Palanques, 1998). Once material has been resuspended, the thermocline then acts as a surface along which resuspended and advected material can be held in suspension.

As discussed in Chapter 4, cores of baroclinic energy flux within the canyon are bottom intensified over the depths 1000-2500 m. When the depth ranges of these

baroclinic energy fluxes are plotted alongside the depth ranges over which nepheloid layers in the Whittard Canyon are sourced from (taken from Wilson et al. (2015b)), a correlation is apparent (Figure 7.1). This suggests that bottom intensification of baroclinic energy and the source regions for nepheloid layers within the canyon are related and that the internal tide is perhaps driving the resuspension and transport of material from the seabed.

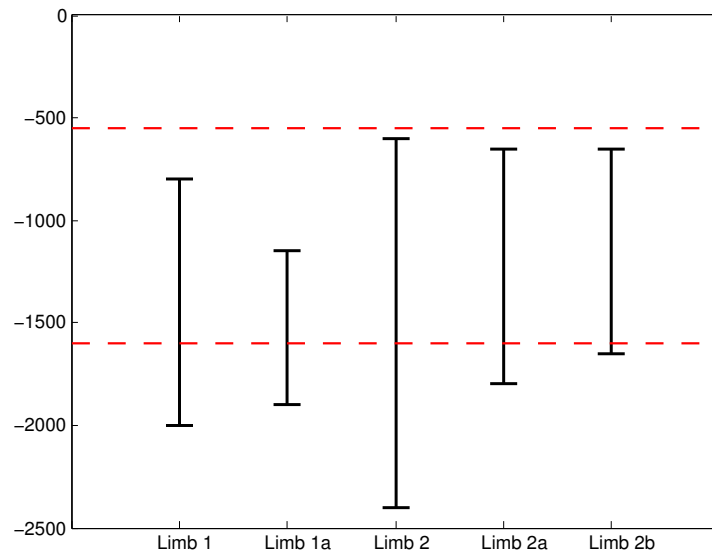


**Figure 7.1:** Depth ranges of baroclinic energy flux cores in the model (black) in comparison with the depth range from where nepheloid layers are sourced (dashed red) (Wilson et al., 2015b).

For the NE Atlantic margin, Thomsen and Gust (2000) suggest a value of  $0.15 \text{ m s}^{-1}$  as a typical threshold speed for the resuspension of fresh organic material. As shown in Figure 7.2, maximum current amplitudes in the model do exceed this value, however, rather than looking at an instantaneous speed at the peak of the internal tidal cycle, it is perhaps more instructive to look at a measure of speed over the tidal cycle such as the RMS speed. Resuspension of material, caused by the internal tide, can therefore occur over large parts of the canyon. The mechanism by which this resuspended material is advected and held in suspension and transported laterally to the mouth of the canyon is not clear, however, it is clear that the source regions for nepheloid layers are intimately connected with the dynamics of the internal tide within the region.

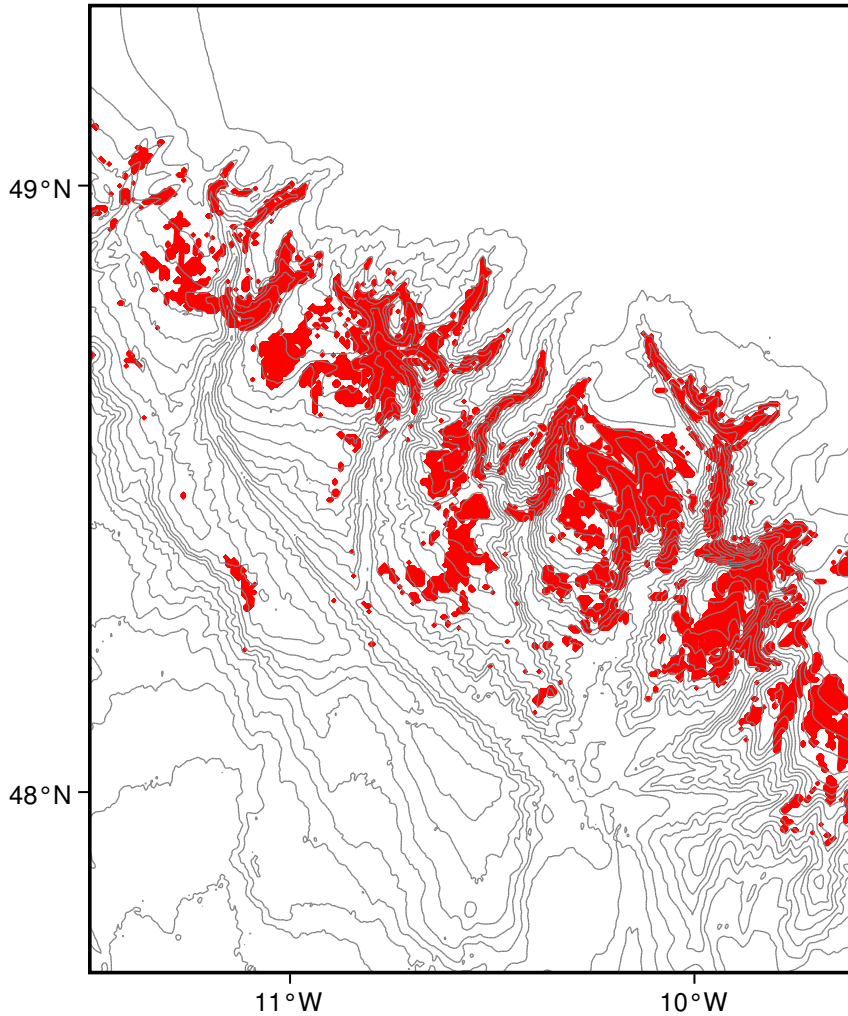


**Figure 7.2:** Locations where RMS current speed for the baroclinic  $M_2$  tidal current exceeds  $0.15 \text{ m s}^{-1}$  (red). Depth contours are plotted every 200 m.

The occurrence of nepheloid layers has also been postulated to be driven by anthropogenic causes (Wilson et al., 2015a) and therefore further work must be carried out to separate internal tide effects from other factors. However, the distinct conditions formed by the internal tide in the various canyon limbs are likely to have an effect on sedimentation, resuspension of organic material and the distribution of biological material. This has implications for habitats within the canyon, which it has been suggested, rely on nepheloid layers as nutrient pathways (Johnson et al., 2013). Further work, integrating internal tide hydrodynamics into predictive habitat models, should aim to shed more light on the complex interplay between the internal tide and the abundance and diversity of habitats within the region.

### 7.2.2 THE VARIABILITY OF ON SHELF ENERGY FLUXES

The on shelf energy fluxes around the Whittard Canyon region, as demonstrated in Section 4.5, are highly variable. This has implications for our current understanding of the dynamics at the Celtic Sea shelf break, as the energy flux past a given point provides an upper limit on the amount of energy available for dissipation and hence turbulent mixing across the shelf. Current estimates of on shelf energy fluxes at the Celtic Sea shelf edge are obtained from a few point measurements on shelf (Green et al., 2008; Hopkins et al., 2014), resulting in widely varying values, from 28-200  $W m^{-1}$ . Resulting estimates of dissipation from these few values therefore do not account for the the degree of variability that the model output demonstrates. Model output such as this should be used in future to inform the location of moorings and sections during observational programmes in order to capture as much of the variability as possible.

Also of note is that when the energy fluxes are integrated along the length of the 300-m isobath, the on shelf baroclinic energy flux is a net positive value (3.38 MW). However, when this value is split into on and off shelf components it becomes clear that a significant amount of energy is not only going on shelf, but is also entering the canyon from generation on the shelf. This complex interplay between baroclinic energy moving onto and from the shelf is likely to make interpretations of observations at particular sites difficult to make. Hence, models that provide greater spatial coverage should be used to aid in the interpretation of observational data.

Turbulent mixing at continental shelves is known to be more variable than in the open ocean and a number of model parameterisation schemes have been formulated to account for this (Carter et al., 2005). However, not all the sources of variability have been determined. As the first numerical study of a dendritic canyon, the results presented here may help to explain some of the variability at shelf edges which are highly corrugated and incised by canyons with multiple limbs. As demonstrated in this work, individual limbs within the canyon have markedly different dissipative regimes (Section 4.4). Further work, both using models and observations should focus on characterising the dissipative characteristics of dendritic canyons, as they have previously been understudied.

### **7.2.3 IMPORTANCE OF DOMAIN SIZE AND BATHYMETRIC RESOLUTION FOR WIDER INTERNAL WAVE MODELLING STUDIES**

The results of Chapters 2 and 5 highlight the importance of using the correct domain size and bathymetric resolution in order to accurately model the internal tide within the Whittard Canyon region. Varying the domain size in this study allowed for the diagnosis of the key generation sites for internal tides within this region, both local and remote. However, local generation within the canyon was found to be modulated by a flux-conversion feedback which was dependant on the phase of remotely generated internal waves. This further highlights the importance of choosing the correct domain size, as even if key remote sources are omitted, even local generation is affected. In this study, a coarse resolution large domain size (not presented here) was used to broadly identify remote generation sites so that the three domain sizes to be tested with higher resolution would not be missing key generation sites. This process was also instructive in identifying what areas weren't important generation sites. If computational power is an issue, then it is as important to identify what does not need to be included, as what should be included in a model domain.

Linear internal wave generation is strongly dependent on the horizontal and vertical scales of bottom topography (Bell, 1975), therefore, using bathymetry that accurately represents the region being studied is important in order to model internal tide dynamics that broadly replicate reality. It can be argued that horizontal wavelengths ranging from 60 m to 6 km forced by steady flows generate internal waves (Cushman-Roisin and Beckers, 2011), however, obtaining bathymetric dataset at this resolution is expensive and time consuming. However, if accurate estimates of barotropic-to-baroclinic conversion are required, then high resolution datasets are needed. We recommend that for the purposes of understanding the 3D structure in the canyon, the bathymetric resolution needs to be as high as possible. However, if a larger domain size was needed, for example, to diagnose far field generation, it would be reasonable to use a lower resolution bathymetric grid to reduce the computational expense of running the model. In conclusion, the choice of domain size and bathymetric resolution to be used in oceanographic simulations should be picked to suit the aim of the modelling study; it is not always necessary to use a large domain size, or the highest resolution bathymetric dataset.

## 7.3 FUTURE WORK

The results presented in this work provide ample opportunities for future work, through extension of the modelling work, and through application of a new understanding of the internal tide to other disciplines.

Although the non-linear behaviour of internal waves is discussed with regards to breakdown of the internal waves during critical reflection, a shortcoming of using POM, is that as a hydrostatic model it cannot capture such behaviour. It is recommended that a non-hydrostatic model, such as MITgcm, be used to fill in this missing information. With this additional suite of modelled results it may be possible to answer the following question: at which topographic scale do non-hydrostatic processes become important?

Additional simulations with different background stratifications would be useful to investigate how changes in stratification impact the internal tide field. Changing stratification is expected to have an impact, with a reduced near-surface stratification, one would expect less energy to be transmitted onto the shelf as the seasonal thermocline appears to act as a waveguide for internal tides. It would also be interesting to help investigate the temporal variations in the internal wave field over seasonal time scales.

Analysis of how bathymetric resolution results in differing conversion/dissipation at different modes i.e. modal analysis as per the work of Zilberman et al. (2009), would help to explain why the observed patterns of dissipation and conversion occur when the bathymetry is smoothed.

It is beyond the scope of this work to remove the canyon completely and model an idealised shelf profile, however idealised canyon studies that look at dendritic canyons would also be useful to unpick the dynamics within the canyon, which this work has only just touched upon.

The initial work on producing layers for predictive habitat models shows how output from models can be used by other disciplines. With more information on the geology of the canyon, one could estimate other parameters e.g. bottom stress values, which may provide useful information for geomorphologists.

## **7.4 CONCLUSION**

The modelling efforts here provide the first detailed look at the internal tide structure within Whittard Canyon and demonstrate the impact that the canyon has on the Celtic Sea shelf region. The high energy associated with the internal tide is likely to impact both biology within the canyon and sedimentation patterns, and for the first time, information on the internal tide is provided for the entire canyon. Although modelling results should be treated with caution, they provide unparalleled spatial coverage for minimal cost. The modelling efforts here should be used to target areas of interest in future observational programmes.

# **Appendices**



# A

## APPENDIX A - MODEL RUNS

**Table A.1:** List of model runs used in this thesis. The control run is marked in red.

Purpose	Bathymetric grid	Grid size	Bathymetric resolution	Stratification	Run length (tidal cycles)	Run time <sup>a</sup>
Diagnosing domain size sensitivity	<i>wc01</i>	301 × 461	500 m	summer	21	9 hours
	<i>wc02</i>	541 × 661	500 m	<i>summer</i>	21	38 hours
	<i>wc03</i>	781 × 861	500 m	<i>summer</i>	21	46 hours
Diagnosing run length sensitivity	<i>wc02</i>	541 × 661	500 m	<i>summer</i>	21	38 hours
	<i>wc02</i>	<b>541 × 661</b>	<b>500 m</b>	<b>summer</b>	<b>32</b>	<b>55 hours</b>
	<i>wc02</i>	541 × 661	500 m	<i>summer</i>	43	72 hours
Diagnosing bathymetric resolution sensitivity	500-m <sup>b</sup>	541 × 661	500 m	<i>summer</i>	32	55 hours
	1.5-km	541 × 661	1.5 km	<i>summer</i>	32	55 hours
	5.5-km	541 × 661	5.5 km	<i>summer</i>	32	55 hours
	15-km	541 × 661	15 km	<i>summer</i>	32	55 hours

<sup>a</sup> Run time on GRACE (High powered computing cluster) at the University of East Anglia.

<sup>b</sup> Identical to the *wc02* bathymetric grid.

# **B**

## **APPENDIX B - ALONG CANYON SECTIONS OF BAROCLINIC ENERGY FLUX FOR THE MINOR CANYON LIMBS**

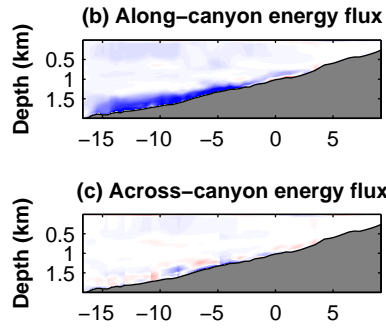


**Figure B.1:** Limb 1b along-canyon sections (b) Along-canyon and (c) across-canyon baroclinic  $M_2$  energy flux with distance along the thalweg. Positive along-canyon values are towards the head of the canyon. Positive across-canyon values are to the left when looking up canyon.

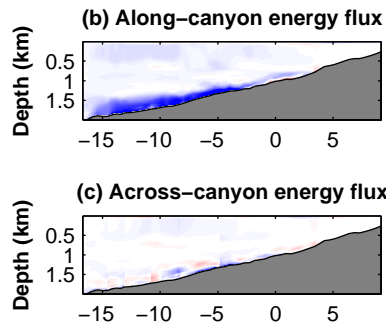


**Figure B.2:** Limb 1c along-canyon sections (See Figure B.1 for explanation)

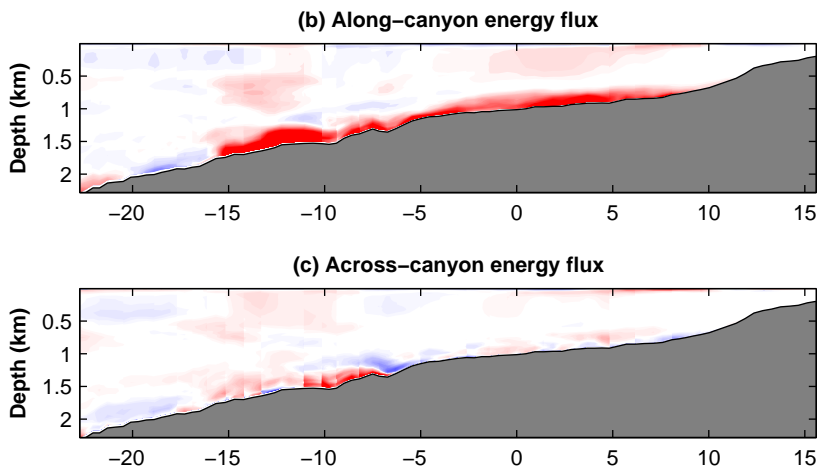


**Figure B.3:** Limb 2b along-canyon sections (See Figure B.1 for explanation)

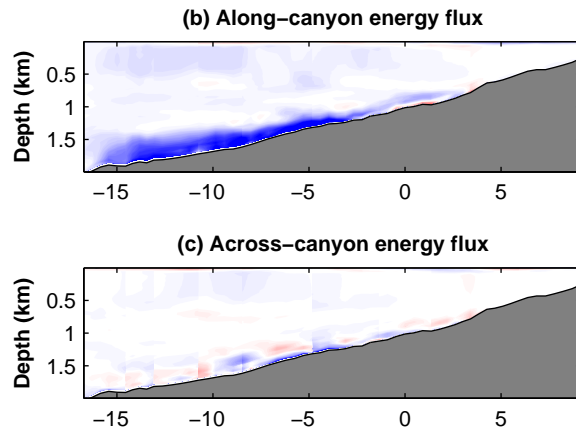


**Figure B.4:** Limb 2c along-canyon sections (See Figure B.1 for explanation)

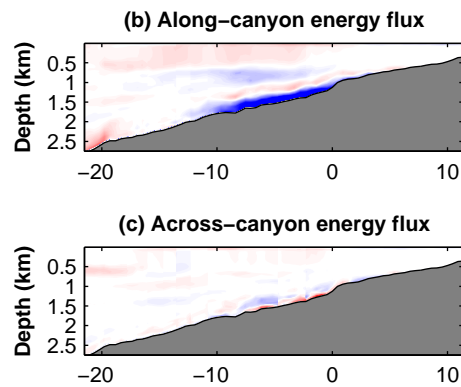


**Figure B.5:** Limb 3b along-canyon sections (See Figure B.1 for explanation)

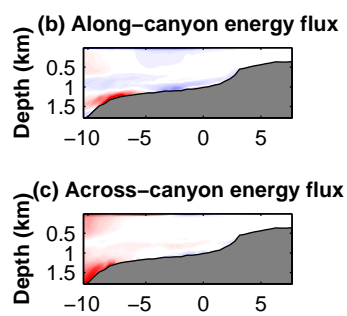


**Figure B.6:** Limb 4b along-canyon sections (See Figure B.1 for explanation)



## REFERENCES

- Amaro, T., H. de Stigter, M. Lavaleye, and G. Duineveld, 2015: Organic matter enrichment in the Whittard Channel; its origin and possible effects on benthic megafauna. *Deep Sea Research Part I: Oceanographic Research Papers*, **102**, 90–100.
- Amaro, T., et al., 2016: The Whittard Canyon—a case study of submarine canyon processes. *Progress in Oceanography*, **146**, 38–57.
- Baines, P. G., 1982: On internal tide generation models. *Deep Sea Research Part A. Oceanographic Research Papers*, **29 (3)**, 307–338.
- Becker, J., et al., 2009: Global bathymetry and elevation data at 30 arc seconds resolution: SRTM30\_PLUS. *Marine Geodesy*, **32 (4)**, 355–371.
- Bell, T., 1974: Internal wave-turbulence interpretation of ocean fine structure. *Geophysical Research Letters*, **1 (6)**, 253–255.
- Bell, T., 1975: Topographically generated internal waves in the open ocean. *Journal of Geophysical Research*, **80 (3)**, 320–327.
- Blumberg, A. F. and G. L. Mellor, 1987: A description of a three-dimensional coastal ocean circulation model. *Coastal and estuarine sciences*, **4**, 1–16.
- Bourillet, Z. S., J-F. and T. Mulder, 2006: The French Atlantic margin and deep-sea submarine systems. *Geo-Marine Letters*, **26 (6)**, 311–315.
- Bower, A., et al., 2002: Directly measured mid-depth circulation in the northeastern north atlantic ocean. *Nature*, **419 (6907)**, 603–607.
- Carter, G. S., 2010: Barotropic and baroclinic  $m_2$  tides in the Monterey Bay region. *Journal of Physical Oceanography*, **40 (8)**, 1766–1783, times Cited: 10.
- Carter, G. S., O. B. Fringer, and E. D. Zaron, 2012: Regional models of internal tides.
- Carter, G. S. and M. C. Gregg, 2002: Intense, variable mixing near the head of Monterey Submarine Canyon. *Journal of Physical Oceanography*, **32 (11)**, 3145–3165.
- Carter, G. S., M. C. Gregg, and R.-C. Lien, 2005: Internal waves, solitary-like waves, and mixing on the monterey bay shelf. *Continental Shelf Research*, **25 (12)**, 1499–1520.

- Carter, G. S. and M. A. Merrifield, 2007: Open boundary conditions for regional tidal simulations. *Ocean Modelling*, **18** (3), 194–209.
- Carter, G. S., et al., 2008: Energetics of  $m_2$  barotropic-to-baroclinic tidal conversion at the Hawaiian Islands. *Journal of Physical Oceanography*, **38** (10), 2205–2223.
- Carter, M. C. G., G. S. and M. A. Merrifield, 2006: Flow and mixing around a small seamount on Kaena Ridge, Hawaii. *Journal of physical oceanography*, **36** (6), 1036–1052.
- Cummins, P. F. and L.-Y. Oey, 1997: Simulation of barotropic and baroclinic tides off northern British Columbia. *Journal of Physical Oceanography*, **27** (5), 762–781.
- Cunningham, M. J., S. Hodgson, D. G. Masson, and L. M. Parson, 2005: An evaluation of along- and down-slope sediment transport processes between Goban spur and Brenot spur on the Celtic Margin of the Bay of Biscay. *Sedimentary Geology*, **179** (1 - 2), 99 – 116.
- Cushman-Roisin, B. and J.-M. Beckers, 2011: *Introduction to geophysical fluid dynamics: physical and numerical aspects*, Vol. 101. Academic Press.
- De Leo, F. C., C. R. Smith, A. A. Rowden, D. A. Bowden, and M. R. Clark, 2010: Submarine canyons: hotspots of benthic biomass and productivity in the deep sea. *Proceedings of the Royal Society of London B: Biological Sciences*, rspb20100462.
- Duros, P., et al., 2011: Live (stained) benthic foraminifera in the Whittard Canyon, Celtic margin (NE Atlantic). *Deep Sea Research Part I: Oceanographic Research Papers*, **58** (2), 128–146.
- Egbert, G. D. and S. Y. Erofeeva, 2002: Efficient inverse modeling of barotropic ocean tides. *Journal of Atmospheric and Oceanic Technology*, **19** (2), 183–204.
- Flather, R., 1976: A tidal model of the northwest European continental shelf. *Mem. Soc. R. Sci. Liege*, **10** (6), 141–164.
- Frederiksen, R., A. Jensen, and H. Westerberg, 1992: The distribution of the scleractinian coral *Lophelia pertusa* around the Faroe Islands and the relation to internal tidal mixing. *Sarsia*, **77** (2), 157–171.
- Garrett, C. and E. Kunze, 2007: Internal tide generation in the deep ocean. *Annu. Rev. Fluid Mech.*, **39**, 57–87.

- Gerkema, T., 2002: Application of an internal tide generation model to baroclinic spring-neap cycles. *Journal of Geophysical Research: Oceans*, **107** (C9).
- Gill, A. E., 1982: *Atmosphere-ocean dynamics*, Vol. 30. Academic press.
- Gordon, R. L. and N. F. Marshall, 1976: Submarine canyons - internal wave traps. *Geophysical Research Letters*, **3** (10), 622–624.
- Green, J. A. M., J. H. Simpson, S. Legg, and M. R. Palmer, 2008: Internal waves, baroclinic energy fluxes and mixing at the European shelf edge. *Continental Shelf Research*, **28** (7), 937–950.
- Gregg, M., R. Hall, G. Carter, M. Alford, R.-C. Lien, D. Winkel, and D. Wain, 2011: Flow and mixing in Ascension, a steep, narrow canyon. *Journal of Geophysical Research: Oceans*, **116** (C7).
- Guisan, A. and N. E. Zimmermann, 2000: Predictive habitat distribution models in ecology. *Ecological modelling*, **135** (2), 147–186.
- Hall, R. A. and G. S. Carter, 2011: Internal tides in Monterey Submarine Canyon. *Journal of Physical Oceanography*, **41** (1), 186–204.
- Hall, R. A., J. M. Huthnance, and R. G. Williams, 2013: Internal wave reflection on shelf slopes with depth-varying stratification. *Journal of Physical Oceanography*, **43** (2), 248–258.
- Harris, P. T. and T. Whiteway, 2011: Global distribution of large submarine canyons: Geomorphic differences between active and passive continental margins. *Marine Geology*, **285** (1-4), 69–86.
- Hickey, B., 1995: Coastal submarine canyons. *Topographic effects in the ocean*, 95–110.
- Hickman, A. E., C. M. Moore, J. Sharples, M. I. Lucas, G. H. Tilstone, V. Krivtsov, and P. M. Holligan, 2012: Primary production and nitrate uptake within the seasonal thermocline of a stratified shelf sea. *Marine Ecology Progress Series*, **463**, 39–57.
- Holt, J. and S. Thorpe, 1997: The propagation of high frequency internal waves in the Celtic Sea. *Deep Sea Research Part I: Oceanographic Research Papers*, **44** (12), 2087–2116.
- Hopkins, J. E., G. R. Stephenson, J. Green, M. E. Inall, and M. R. Palmer, 2014: Storms modify baroclinic energy fluxes in a seasonally stratified shelf sea: Inertial-tidal interaction. *Journal of Geophysical Research: Oceans*, **119** (10), 6863–6883.

- Hotchkiss, F. S. and C. Wunsch, 1982: Internal waves in Hudson Canyon with possible geological implications. *Deep-Sea Research Part a-Oceanographic Research Papers*, **29 (4)**, 415–442.
- Huvenne, V. A., P. A. Tyler, D. G. Masson, E. H. Fisher, C. Hauton, V. Hühnerbach, T. P. Le Bas, and G. A. Wolff, 2011: A picture on the wall: innovative mapping reveals cold-water coral refuge in submarine canyon. *PloS one*, **6 (12)**, e28755.
- Inall, M., D. Aleynik, T. Boyd, M. Palmer, and J. Sharples, 2011: Internal tide coherence and decay over a wide shelf sea. *Geophysical Research Letters*, **38 (23)**.
- Johnson, M. P., M. White, A. Wilson, L. Würzberg, E. Schwabe, H. Folch, and A. L. Allcock, 2013: A vertical wall dominated by *Acesta excavata* and *Neopycnodonte zibrowii*, part of an undersampled group of deep-sea habitats. *PloS one*, **8 (11)**, e79917.
- Kang, D. and O. Fringer, 2012: Energetics of barotropic and baroclinic tides in the Monterey Bay area. *Journal of Physical Oceanography*, **42 (2)**, 272 – 290.
- Kelly, S. and J. Nash, 2010: Internal-tide generation and destruction by shoaling internal tides. *Geophysical Research Letters*, **37 (23)**.
- Kunze, E., L. K. Rosenfeld, G. S. Carter, and M. C. Gregg, 2002: Internal waves in Monterey Submarine Canyon. *Journal of Physical Oceanography*, **32 (6)**, 1890–1913.
- Lee, I. H., R.-C. Lien, J. T. Liu, and W.-s. Chuang, 2009: Turbulent mixing and internal tides in Gaoping (Kaoping) Submarine Canyon, Taiwan. *Journal of Marine Systems*, **76 (4)**, 383–396.
- Legg, S. and A. Adcroft, 2003: Internal wave breaking at concave and convex continental slopes\*. *Journal of Physical Oceanography*, **33 (11)**, 2224–2246.
- Martini, K., M. Alford, J. Nash, E. Kunze, and M. Merrifield, 2007: Diagnosing a partly standing internal wave in Mamala Bay, Oahu. *Geophysical Research Letters*, **34 (17)**.
- McDougall, T. J. and P. M. Barker, 2011: Getting started with TEOS-10 and the Gibbs Seawater (GSW) oceanographic toolbox. *SCOR/IAPSO WG*, **127**, 1–28.
- McPhee-Shaw, E., R. Sternberg, B. Mullenbach, and A. Ogston, 2004: Observations of intermediate nepheloid layers on the northern California continental margin. *Continental Shelf Research*, **24 (6)**, 693–720.
- McPhee-Shaw, E. E. and E. Kunze, 2002: Boundary layer intrusions from a sloping

- bottom: A mechanism for generating intermediate nepheloid layers. *Journal of Geophysical Research: Oceans (1978–2012)*, **107 (C6)**, 3–1.
- Mellor, G., T. Ezer, and L. Oey, 1994: The pressure gradient conundrum of sigma coordinate ocean models. *Journal of Atmospheric and Oceanic Technology*, **11 (4)**, 1126–1134.
- Mohn, C., A. Rengstorf, M. White, G. Duineveld, F. Mienis, K. Soetaert, and A. Grehan, 2014: Linking benthic hydrodynamics and cold-water coral occurrences: A high-resolution model study at three cold-water coral provinces in the NE Atlantic. *Progress in Oceanography*, **122**, 92–104.
- Müller, P. and N. Xu, 1992: Scattering of oceanic internal gravity waves off random bottom topography. *Journal of physical oceanography*, **22 (5)**, 474–488.
- Nash, J. D., M. H. Alford, and E. Kunze, 2005: Estimating internal wave energy fluxes in the ocean. *Journal of Atmospheric and Oceanic Technology*, **22 (10)**, 1551–1570.
- Nash, J. D., E. Kunze, J. M. Toole, and R. W. Schmitt, 2004: Internal tide reflection and turbulent mixing on the continental slope. *Journal of Physical Oceanography*, **34 (5)**, 1117–1134.
- Niwa, Y. and T. Hibiya, 2001: Numerical study of the spatial distribution of the m2 internal tide in the pacific ocean. *Journal of Geophysical Research: Oceans (1978–2012)*, **106 (C10)**, 22 441–22 449.
- Pérez, F. F., A. F. Ríos, B. A. King, and R. T. Pollard, 1995: Decadal changes of the  $\theta$ -s relationship of the Eastern North Atlantic Central Water. *Deep Sea Research Part I: Oceanographic Research Papers*, **42 (11)**, 1849–1864.
- Petruncio, E. T., J. D. Paduan, and L. K. Rosenfeld, 2002: Numerical simulations of the internal tide in a submarine canyon. *Ocean Modelling*, **4 (3-4)**, 221–248.
- Petruncio, E. T., L. K. Rosenfeld, and J. D. Paduan, 1998: Observations of the internal tide in Monterey canyon. *Journal of Physical Oceanography*, **28 (10)**, 1873–1903.
- Pingree, R. and B. Le Cann, 1989: Celtic and Armorican slope and shelf residual currents. *Progress in Oceanography*, **23 (4)**, 303–338.
- Pingree, R. and B. Le Cann, 1990: Structure, strength and seasonality of the slope currents in the Bay of biscay region. *Journal of the Marine Biological Association of the United Kingdom*, **70 (04)**, 857–885.

- Pingree, R., G. Mardell, and D. Cartwright, 1981: Slope turbulence, internal waves and phytoplankton growth at the Celtic sea shelf-break [and discussion]. *Philosophical Transactions of the Royal Society of London A: Mathematical, Physical and Engineering Sciences*, **302 (1472)**, 663–682.
- Pingree, R. D., G. T. Mardell, and A. L. New, 1986: Propagation of internal tides from the upper slopes of the Bay of Biscay.
- Pollard, R., M. Griffiths, S. Cunningham, J. Read, F. F. Pérez, and A. F. Ríos, 1996: Vivaldi 1991 - A study of the formation, circulation and ventilation of Eastern North Atlantic Central Water. *Progress in Oceanography*, **37 (2)**, 167–192.
- Puig, P. and A. Palanques, 1998: Nepheloid structure and hydrographic control on the Barcelona continental margin, northwestern Mediterranean. *Marine Geology*, **149 (1)**, 39–54.
- Puig, P., A. Palanques, J. Guillén, and M. El Khatab, 2004: Role of internal waves in the generation of nepheloid layers on the northwestern Alboran slope: implications for continental margin shaping. *Journal of Geophysical Research: Oceans*, **109 (C9)**.
- Rainville, L., T. S. Johnston, G. S. Carter, M. A. Merrifield, R. Pinkel, P. F. Worcester, and B. D. Dushaw, 2010: Interference pattern and propagation of the m<sup>2</sup> internal tide south of the Hawaiian ridge. *Journal of Physical Oceanography*, **40 (2)**, 311–325.
- Reid, G. and D. Hamilton, 1990: A reconnaissance survey of the Whittard sea fan, southwestern approaches, British Isles. *Marine Geology*, **92 (1)**, 69–86.
- Robert, K., D. O. Jones, P. A. Tyler, D. Van Rooij, and V. A. Huvenne, 2015: Finding the hotspots within a biodiversity hotspot: fine-scale biological predictions within a submarine canyon using high-resolution acoustic mapping techniques. *Marine Ecology*, **36 (4)**, 1256–1276.
- Sharples, J., C. M. Moore, A. E. Hickman, P. M. Holligan, J. F. Tweddle, M. R. Palmer, and J. H. Simpson, 2009: Internal tidal mixing as a control on continental margin ecosystems. *Geophysical Research Letters*, **36**.
- Simpson, J. H., 1998b: The Celtic seas coastal segment. *The Sea, vol. 11.*, R. A. Brink, K.H., Ed., 659–698.
- St. Laurent, L. and C. Garrett, 2002: The role of internal tides in mixing the deep ocean. *Journal of Physical Oceanography*, **32 (10)**, 2882–2899.

- Stewart, H. A., J. S. Davies, J. Guinan, and K. L. Howell, 2014: The Dangeard and Explorer canyons, South Western Approaches UK: geology, sedimentology and newly discovered cold-water coral mini-mounds. *Deep Sea Research Part II: Topical Studies in Oceanography*, **104**, 230–244.
- Thomsen, L. and G. Gust, 2000: Sediment erosion thresholds and characteristics of resuspended aggregates on the western European continental margin. *Deep Sea Research Part I: Oceanographic Research Papers*, **47 (10)**, 1881–1897.
- Thomson, R. E. and W. J. Emery, 2014: *Data analysis methods in physical oceanography*. Newnes.
- Thorpe, S. and M. White, 1988: A deep intermediate nepheloid layer. *Deep Sea Research Part A. Oceanographic Research Papers*, **35 (9)**, 1665–1671.
- van Aken, H. M., 2000: The hydrography of the mid-latitude Northeast Atlantic Ocean: II: The intermediate water masses. *Deep Sea Research Part I: Oceanographic Research Papers*, **47 (5)**, 789–824.
- Van Rooij, D., et al., 2010: The le danois contourite depositional system: interactions between the mediterranean outflow water and the upper cantabrian slope (north iberian margin). *Marine Geology*, **274 (1)**, 1–20.
- Van Weering, T., L. Thomsen, J. Heerwaarden, B. Koster, and T. Viergutz, 2000: A seabed lander and new techniques for long term in situ study of deep-sea near bed dynamics. *Sea Techn*, **41**, 17–27.
- Vlasenko, V., N. Stashchuk, M. E. Inall, and J. E. Hopkins, 2014: Tidal energy conversion in a global hot spot: On the 3-D dynamics of baroclinic tides at the Celtic Sea shelf break. *Journal of Geophysical Research: Oceans*, **119 (6)**, 3249–3265.
- Vlasenko, V., N. Stashchuk, M. E. Inall, M. Porter, and D. Aleynik, 2016: Focusing of baroclinic tidal energy in a canyon. *Journal of Geophysical Research: Oceans*, **121 (4)**, 2824–2840.
- White, M. and B. Dorschel, 2010: The importance of the permanent thermocline to the cold water coral carbonate mound distribution in the NE Atlantic. *Earth and Planetary Science Letters*, **296 (3)**, 395–402.
- Wilson, A. M., K. Kiriakoulakis, R. Raine, H. D. Gerritsen, S. Blackbird, A. L. Allcock, and M. White, 2015a: Anthropogenic influence on sediment transport in the Whittard Canyon, NE Atlantic. *Marine Pollution Bulletin*, **101 (1)**, 320–329.

- Wilson, A. M., R. Raine, C. Mohn, and M. White, 2015b: Nepheloid layer distribution in the Whittard Canyon, NE Atlantic Margin. *Marine Geology*, **367**, 130–142.
- Zhang, W. G., T. F. Duda, and I. A. Udovydchenkov, 2014: Modeling and analysis of internal- tide generation and beamlike onshore propagation in the vicinity of shelfbreak canyons. *Journal of Physical Oceanography*, **44** (3), 834–849.
- Zilberman, N., J. Becker, M. Merrifield, and G. Carter, 2009: Model estimates of  $M_2$  internal tide generation over Mid-Atlantic Ridge topography. *Journal of Physical Oceanography*, **39** (10), 2635–2651.